



Detailed Velocity, Temperature, and Heat Flux Measurements on a Large Scale Film Cooling Model

Philip Poinsette, Douglas Thurman, and Barbara Lucci
Glenn Research Center, Cleveland, Ohio

NASA STI Program . . . in Profile

Since its founding, NASA has been dedicated to the advancement of aeronautics and space science. The NASA Scientific and Technical Information (STI) Program plays a key part in helping NASA maintain this important role.

The NASA STI Program operates under the auspices of the Agency Chief Information Officer. It collects, organizes, provides for archiving, and disseminates NASA's STI. The NASA STI Program provides access to the NASA Technical Report Server—Registered (NTRS Reg) and NASA Technical Report Server—Public (NTRS) thus providing one of the largest collections of aeronautical and space science STI in the world. Results are published in both non-NASA channels and by NASA in the NASA STI Report Series, which includes the following report types:

- **TECHNICAL PUBLICATION.** Reports of completed research or a major significant phase of research that present the results of NASA programs and include extensive data or theoretical analysis. Includes compilations of significant scientific and technical data and information deemed to be of continuing reference value. NASA counter-part of peer-reviewed formal professional papers, but has less stringent limitations on manuscript length and extent of graphic presentations.
- **TECHNICAL MEMORANDUM.** Scientific and technical findings that are preliminary or of specialized interest, e.g., “quick-release” reports, working papers, and bibliographies that contain minimal annotation. Does not contain extensive analysis.
- **CONTRACTOR REPORT.** Scientific and technical findings by NASA-sponsored contractors and grantees.
- **CONFERENCE PUBLICATION.** Collected papers from scientific and technical conferences, symposia, seminars, or other meetings sponsored or co-sponsored by NASA.
- **SPECIAL PUBLICATION.** Scientific, technical, or historical information from NASA programs, projects, and missions, often concerned with subjects having substantial public interest.
- **TECHNICAL TRANSLATION.** English-language translations of foreign scientific and technical material pertinent to NASA's mission.

For more information about the NASA STI program, see the following:

- Access the NASA STI program home page at <http://www.sti.nasa.gov>
- E-mail your question to help@sti.nasa.gov
- Fax your question to the NASA STI Information Desk at 757-864-6500
- Telephone the NASA STI Information Desk at 757-864-9658
- Write to:
NASA STI Program
Mail Stop 148
NASA Langley Research Center
Hampton, VA 23681-2199



Detailed Velocity, Temperature, and Heat Flux Measurements on a Large Scale Film Cooling Model

Philip Poinsette, Douglas Thurman, and Barbara Lucci
Glenn Research Center, Cleveland, Ohio

National Aeronautics and
Space Administration

Glenn Research Center
Cleveland, Ohio 44135

Acknowledgments

Data discussed in this report is publically available at <https://data.nasa.gov/Aerospace/Film-Cooling-Data/tjbu-3afk>.

This work was sponsored by the
Transformative Aeronautics Concepts Program.

Trade names and trademarks are used in this report for identification only. Their usage does not constitute an official endorsement, either expressed or implied, by the National Aeronautics and Space Administration.

Level of Review: This material has been technically reviewed by technical management.

Detailed Velocity, Temperature, and Heat Flux Measurements on a Large Scale Film Cooling Model

Philip Poinsatte, Douglas Thurman, and Barbara Lucci
National Aeronautics and Space Administration
Glenn Research Center
Cleveland, Ohio 44135

Abstract

To investigate the flow physics of turbine film cooling, detailed mean and fluctuating velocity and temperature surveys were made in the turbulent jet flow field behind a row of large scale film cooling holes. Additionally, surface heat transfer, film effectiveness, and turbulent heat flux values were determined. Measurements were made in the NASA Engine Research Building (ERB) SW-6 test facility, which consists of an 8.15-in² open-inlet wind tunnel with a temperature-controlled secondary flow system. The film-cooling test plate fit into the wind tunnel such that the heat transfer surface formed the wind tunnel floor. This plate consisted of a three-hole array of film cooling holes that were fed from a plenum of different temperature. The model geometry was scaled up roughly 30 times of typical turbine film cooling size to enable high spatial resolution measurements near the film coolant hole. The cooling holes had a diameter of 0.75 in. (19 mm), pitch spacing of 3, and were angled 30° from the streamwise direction. High-resolution survey data was taken along a centerline streamwise plane behind the hole as well as at various cross-sectional planes behind the hole at two blowing ratios. Mean and fluctuating flow field velocity and temperature measurements were made using various thin wire anemometry probes and small thermocouple sensors; surface temperature and heat transfer measurements were made employing liquid crystal and infrared imaging techniques. Reported variables include temperatures, velocity components, turbulence intensities and length scales, and Reynolds stresses. Additionally, high quality turbulent heat flux measurements were acquired through simultaneous measurement of flow field temperature and velocity using constant temperature and constant current anemometry probes with a jet-to-freestream temperature difference of approximately 75°. Relevant data is available on the NASA Open Data Portal at <https://data.nasa.gov/Aerospace/Film-Cooling-Data/tjbu-3afk>.

Nomenclature

BR	blowing ratio, $BR = \frac{(\rho U)_{injection}}{(\rho U)_{\infty}}$
CCA	constant current anemometry
CTA	constant temperature anemometry
D	diameter of film cooling hole
DLS	dissipative length scale
E	energy
ERB	Engine Research Building
f	frequency of the anemometry signal
ILS	integral length scale
IR	infrared

L	length of film cooling hole
LES	large eddy simulation
L_w	square duct side length, $L_w = 8.15$ in. (207 mm)
N	number of points taken in the sample
P	pitch (distance) between film cooling holes
PIV	particle image velocimetry
RANS	Reynolds-averaged Navier–Stokes
T	temperature
u	streamwise velocity component
U_{inf}	freestream streamwise velocity
v	spanwise velocity component
w	vertical velocity component
η	film cooling effectiveness, $\eta = \frac{(T - T_{IRsurface})}{(T_{\infty} - T_{plenum})}$
θ	nondimensional temperature, $\theta = \frac{(T - T_{\infty})}{(T_{plenum} - T_{\infty})}$
ρ	density of fluid
∞	freestream condition

Introduction

Hot turbine engines require some form of cooling due to material limits. Several methods exist to actively cool the hot engine components. Film cooling of combustor liners and high pressure turbine blades and vanes is conventionally used to provide a thin layer of cooler air that is bled from the compressor of the engine to help protect the metal surface from the extreme freestream temperatures. Optimization of the location of film cooling holes is typically done using analytical codes. These codes however often overestimate or underestimate the amount of cooling required due to the turbulence model's inability to accurately predict the complicated interaction of the coolant and freestream flows.

Numerous experimental studies have investigated coolant-in-jet flow interactions, providing important validation data for computational code evaluation, but these studies usually include measurements of individual independent parameters such as temperature and velocity components and their fluctuating values. Wernet et al. (Refs. 1 and 2) provided both temperature and velocity measurements on film cooled plates in separate tests using tomographic and dual plane particle image velocimetry (PIV) and Raman thermal experiments. Velocity and fluctuation measurements in a film cooling array using constant temperature anemometry (CTA) were presented in El-Gabry et al. (Ref. 3). Thole et al. (Ref. 4) measured fluid temperatures along the centerline of a jet using constant current anemometry (CCA), and temperature measurements using CCA and thermocouples were determined in Womack et al. (Ref. 5). While these types of studies help with understanding of temperature and flow field interaction, the prediction of these flow and thermal fields are often deficient due to the complicated flow structures not being accurately captured in Reynolds-averaged Navier–Stokes (RANS) turbulence models, specifically the turbulent heat flux parameters and the lack of simultaneous measurement of velocity and temperature experimental data,

The turbulent heat fluxes $u'T'$, $v'T'$, and $w'T'$ used in RANS models are important in affecting the turbulent transport of heat that needs to be predicted accurately in order to replicate the flow interactions

between the cooler film cooling jets and the hot freestream. There is a limited amount of experimental heat flux data in open literature as it is difficult to obtain simultaneous temperature and velocity in a flow field. Schreivogel et al. (Ref. 6) used thermographic PIV to obtain time-resolved simultaneous temperature and velocity measurements to calculate turbulent diffusion terms in representative film cooling applications. Kohli and Bogard (Ref. 7) investigated turbulent heat fluxes using a combination of CCA temperature measurements and laser Doppler velocimetry. Lau et al. (Ref. 8) acquired velocity and temperature measurements in channel flow using a quadruple hot-wire probe. Those authors found that despite the large probe volume, velocity and shear measurements were well captured, however for unknown reasons, their thermal measurements were less reliable. Smits et al. (Refs. 9 and 10) attempted to better explain the response to temperature fluctuations of a CTA and CCA.

The present paper expands on previously published experimental and computational turbulent heat flux results using simultaneous CTA and CCA measurements. In Borghi et al. (Ref. 11), simultaneous experimental temperature and velocity measurements were acquired and compared to computational results for a large scale film cooled plate at one blowing ratio. The current work compiles an extensive set of experimental data, including heat flux, velocity, temperature, and length scale measurements, for the configuration using the same plate for two blowing ratios.

Experimental Setup

The SW-6 Fundamental Film Cooling Facility, shown in Figure 1, consists of an aluminum bellmouth, flow conditioning screens, and a square acrylic section 8.15 by 8.15 in. (207 by 207 mm) wide with 0.75 in. (19 mm) thick walls. The tunnel was connected to a central exhaust system downstream that pulled room air through the flow path. The test section, shown in Figure 2, consisted of a floor piece fabricated from ABS*plus* thermoplastic in a 3D printer, with three injection holes for periodic flow and boundary conditions. The hole diameter was 0.75 in. (19 mm) and was inclined at 30° from the horizontal surface, with hole spacing $P/D = 3$.

A PC-based data acquisition system was used to acquire data from pressure transducers and thermocouples. The tunnel flow rate was measured from a total pressure probe placed upstream of the test section and static pressure taps located on the sidewalls. Freestream temperature was measured with a thermocouple located upstream of the holes near the total pressure probe. Tunnel flow was nominally 30 ft/s (9.1 m/s) at ambient conditions, providing a Reynolds number based on hole diameter and freestream velocity of 11,000. Freestream turbulence was measured to be less than 1 percent at the inlet to the test section, and boundary layer thickness measured approximately 0.8 in. (20 mm) thick.

The injection flow was provided by blowing pressurized air through a flow meter and into a plenum attached to the underside of the test section floor plate. The tubes connecting the plenum to the test section holes had a length of approximately $L/D = 20$. The injection flow conditions were measured with static pressure taps and thermocouples both inside the plenum and in each injection tube. The injection air was heated using three 750 W parallel in-line electric pipe heaters providing a temperature difference of approximately 75 °F (24 °C) from the room temperature (nominally 70 °F (21 °C)) main flow. Other film cooling data (Ref. 12) with this geometry was previously acquired using cooled secondary air with a smaller temperature difference and is discussed in Appendix A. The preferred setup for the current experiments was to use the heated secondary flow which allowed a larger temperature difference from the freestream room temperature.

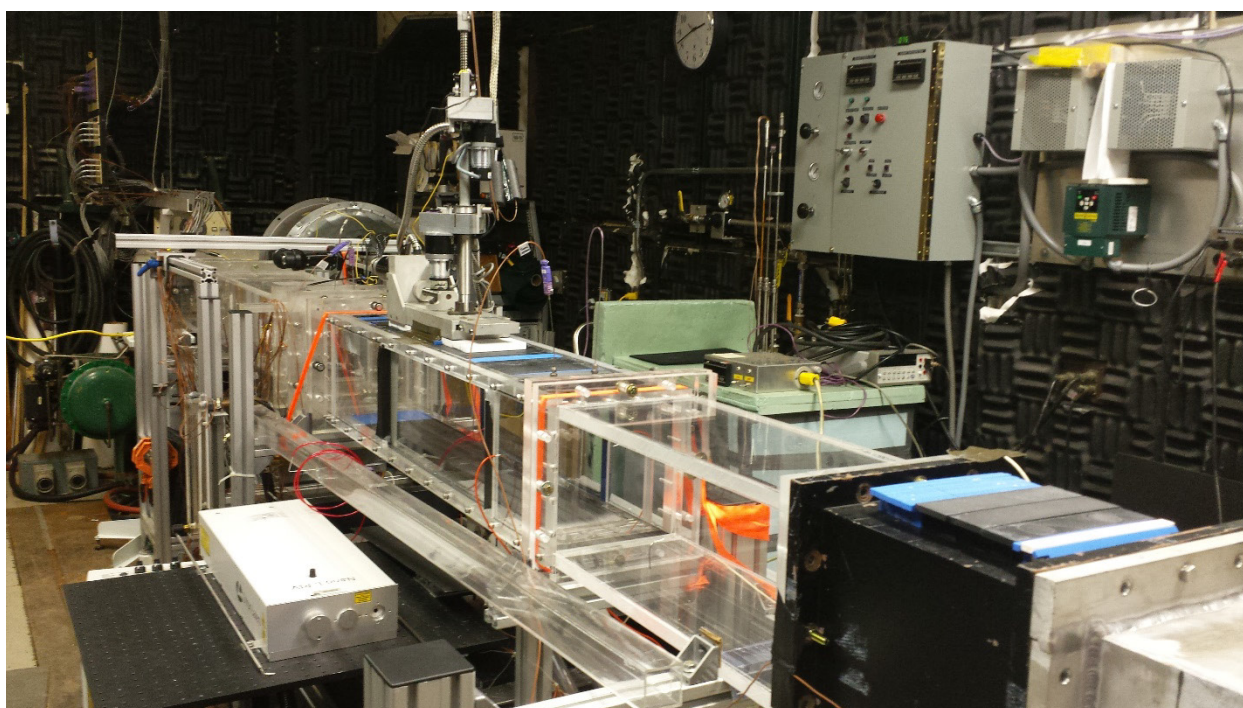
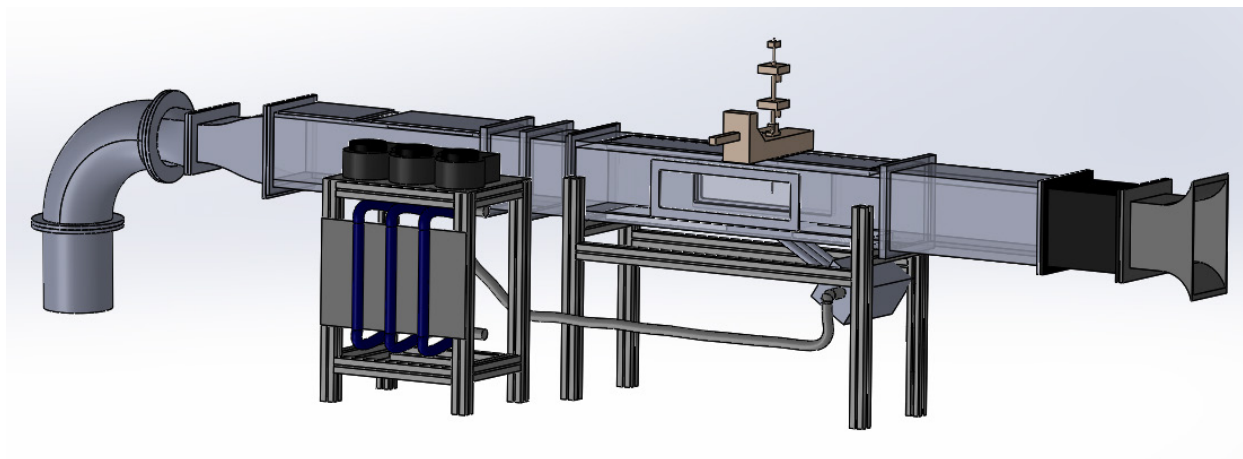


Figure 1.—Film cooling tunnel.

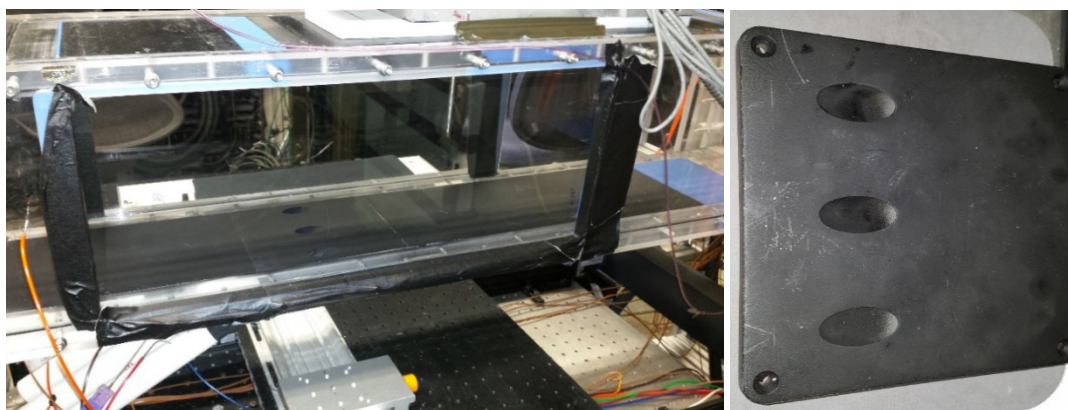


Figure 2.—Plate installed in tunnel (left); Film cooled test plate (right).

Pressure, thermocouple, and hot-wire and cold-wire anemometry surveys were taken along the centerline in the streamwise direction and at cross sectional planes $x/D = 2, 3, 4, 6,$ and 10 , where x is the distance from the leading edge of the hole. An actuator system was used to position the probe in the tunnel. Figure 3 shows the measurement points where data was acquired; the dots indicate measurement points and thus represent the survey interrogation density. Data at blowing ratios, BR , of roughly 1.2 and 2.4 were acquired, where

$$BR = \frac{(\rho U)_{injection}}{(\rho U)_{\infty}} \quad (1)$$

Simultaneous velocity and temperature survey measurements were obtained using two different 3-wire “cross-wire” velocity-temperature (xT) probes, as shown in Figure 4, with one probe measuring ρU , ρV , and T (defined as Probe 1) and the other measuring ρU , ρW , and T (defined as Probe 2). Surveys from these probes were taken separately on different days. Upstream survey planes took approximately 1.5 hr to complete, while downstream survey planes were more expansive and took approximately 3 hr to complete. The two cross-wires of the xT probes used for velocity component measurements were Tungsten-coated, positioned perpendicular to one another with a diameter of $25 \mu\text{m}$, and were connected to a constant temperature “hot-wire” anemometer (CTA) system, with a low frequency cut-off of 10 kHz. The law of cosines was then used to reconstruct the two velocity components from the two perpendicular wires. The wire used for temperature measurements was $1.2 \mu\text{m}$ diameter, 0.4 mm in length, and connected to a constant current “cold-wire” anemometer (CCA) module, which had a low frequency cut-off of 3 kHz. Both measurements were averaged for 3 sec at a frequency of 50 kHz. The temperature wire in Probe 1 was vertically offset (z direction), resulting in a probe volume of roughly $0.15D$ width by $0.2D$ height by $0.15D$ depth. The temperature wire in Probe 2 was slightly offset spanwise (y direction), resulting in a probe volume of roughly $0.2D$ width by $0.15D$ height by $0.15D$ depth. Where possible these wire offsets were accounted for when evaluating the data. To ensure the integrity of this sensitive signal, data noise reduction techniques were employed including special precautions to shield the instrumentation leads and sensors from extraneous electromagnetic interference. A temperature compensation technique was considered to correct for the low-pass filtering inherent to CCA measurements, but due to the limited spatial resolution of the experimental data, it was decided to report only the uncompensated data. See Appendix H for further details about this technique.

The probes were calibrated in a separate test section by varying the velocity and temperature of the flow and recording the voltages for each wire, giving a *density*velocity* versus voltage calibration curve. Since the CTA hot-wire is sensitive to the temperature of the flow, a series of calibration curves at various velocities and temperatures were used to interpolate the *density*velocity* parameter from the wire voltage, as shown in Figure 5. In order to determine the local density in the flow, pressure measurements were acquired at each survey plane using a total-static pressure probe. It was assumed that the local flow pressures would not change for a given flow condition. To accommodate for barometric pressure changes, total and static pressures were normalized by P_{bar} . Once the local density was determined at each point in the survey plane, the local velocity components were then calculated. An uncertainty analysis performed on the temperature measurements were shown to be within 1 percent, and flow measurements showed the data to be nominally within 6 percent.

Film cooling effectiveness is another technique that can aid in determining temperature variations on a film cooled surface. Effectiveness values were calculated from infrared thermography images acquired on the surface of the test plate at various blowing ratios. The plate was painted black to provide an emissivity near 0.95 , and a FLIR SC655 infrared camera with 640 by 480 pixel resolution and a spectral

range of 7.5 to 13 μm was used to acquire the images. Image temperatures were calibrated to surface thermocouples upstream of the holes. Additionally, surface heat transfer measurements were obtained using a similar test plate with a thin Inconel foil sheet attached with a thin adhesive layer to the surface starting at the trailing edge of the film cooling holes. The side edges of the foil were attached to copper bus bars, which were connected to an electric power supply. The foil sheet was heated and allowed to come to steady state. Using the power applied to the Inconel heater along with the air temperature and surface temperature map from IR imaging, local heat transfer coefficients were determined. Note for these measurements the coolant and freestream were maintained as the same temperatures.

Previous PIV data taken using the same tunnel and test section was used to compare time-averaged velocities and fluctuations with the CTA/CCA results. Both dual-plane and tomographic methods were used. A description of the technique used and some of the results are reported in Reference 1.

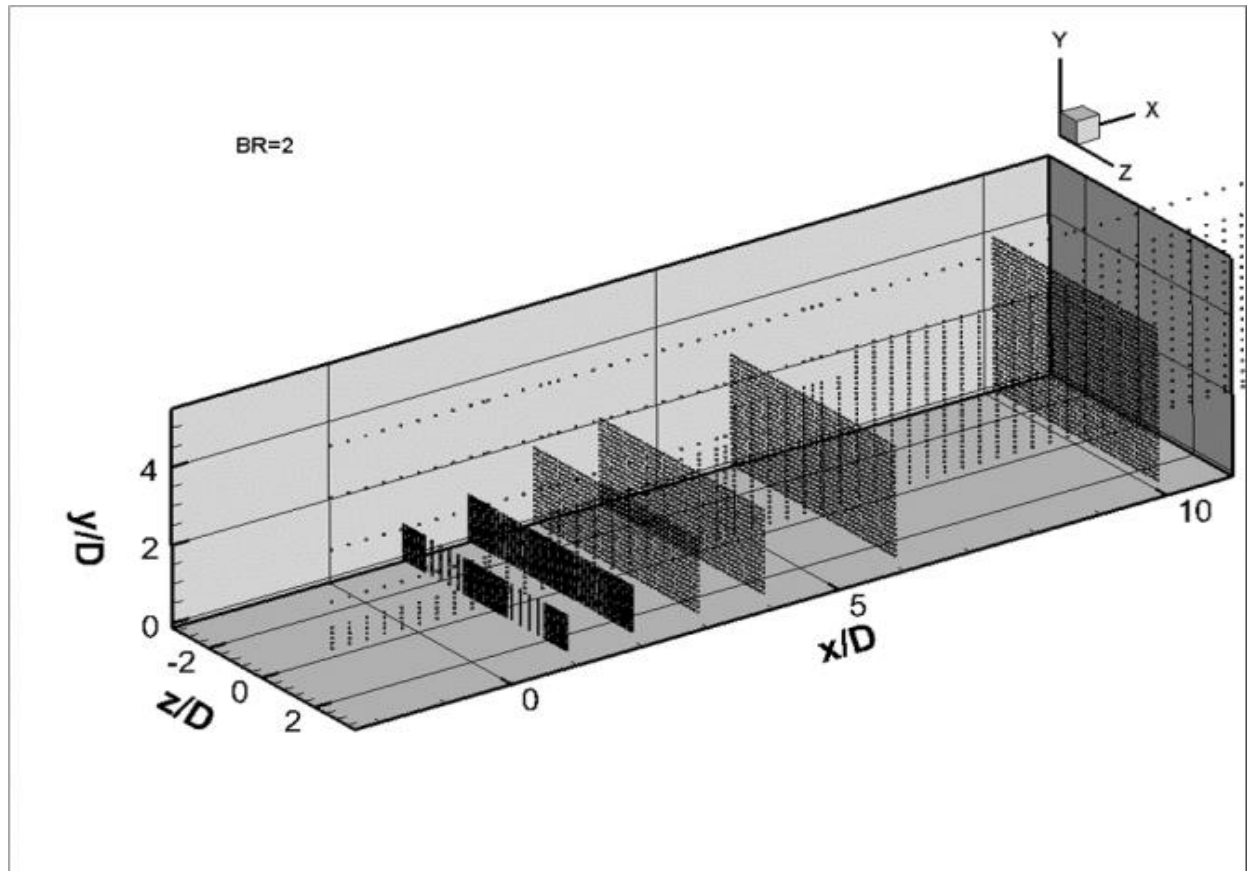


Figure 3.—Typical measurement locations for the $BR = 2.4$ case.

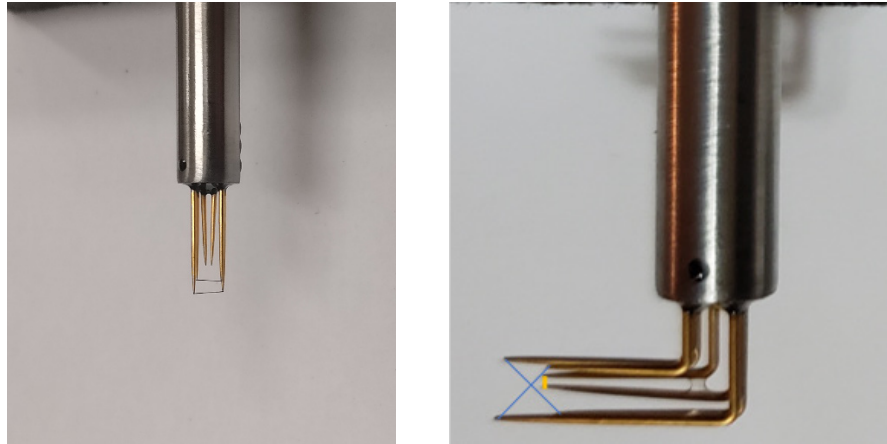


Figure 4.—Close-up of the 3-wire “xT” probes showing cross-wire velocity wires and temperature wire; Probe 1 (left) and Probe 2 (right).

7

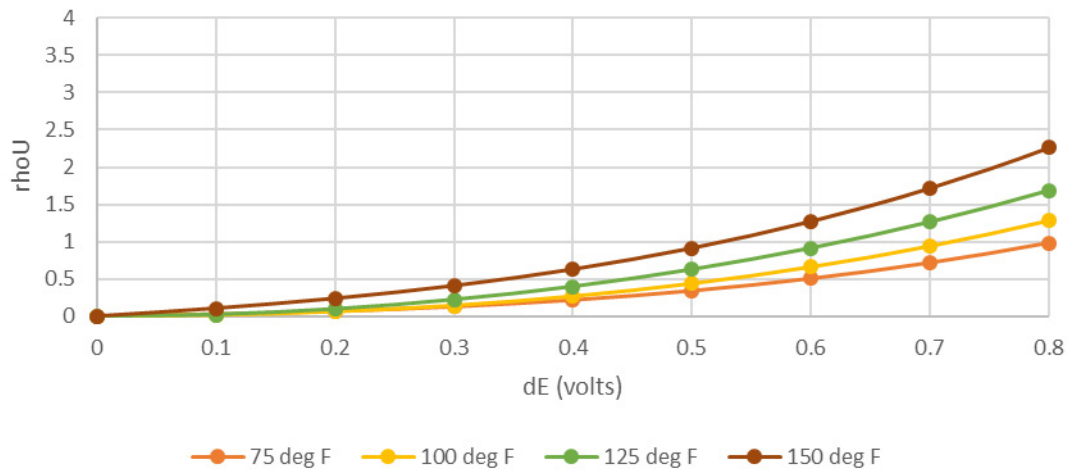


Figure 5.—Typical calibration curves for 3-wire “xT” probe.

Results

The results in this section show mean and fluctuating temperature and flow data including Reynolds stresses and heat fluxes for two blowing ratios along the centerline and at several cross-planes. Additionally, surface temperature and heat transfer data are presented. The data measured in this study can be represented in many ways. Most of the variables presented are normalized by some factor, with many of these factors being straightforward and some not so obvious. A summary of the normalizing parameters chosen for each measurement can be found in Appendix B at the end of this paper. Other information in the Appendices include comparisons of heated and cooled injection air, of the two different probes, of hot wire data with PIV data, and of experimental data with previous computational solutions.

Temperature Measurements

Averaged flow temperatures were normalized by the thermal driving temperature difference between the approach tunnel freestream and the plenum. Figure 6 shows nondimensional local mean temperature contours, defined as

$$\theta = \frac{(T - T_{\infty})}{(T_{plenum} - T_{\infty})} \quad (2)$$

for the centerline and spanwise planes of $x/D = 2, 3, 4, 6, 10$ for BR of 1.2 and 2.4 respectively. Results from both xT probes are shown side-by-side for comparison; recall that Probe 1 measures temperature and the streamwise and spanwise velocity components, and that Probe 2 measures temperature and the streamwise and vertical velocity components. Also, the temperature wire of Probe 1 was located 0.1 in. above the velocity wires, thus the data for probe 1 does not extend as low as Probe 2. See Appendix C for details of probe orientation and wire alignment effects. The data is seen to be consistent between the two probes. The core of the jet is readily visible; it exits the round hole as a flattened circle and progresses to the characteristic kidney-shape pattern moving downstream (typically observed with an inclined jet in cross flow), with maximum temperatures in the jet core sections. The core section of the jet is somewhat larger for the $BR = 2.4$ case relative to the $BR = 1.2$ case. The jet at $BR = 1.2$ appears to stay mostly attached to the model surface, while at $BR = 2.4$ indications of jet liftoff are evident.

Figure 7 shows normalized temperature fluctuations for both probes at the same planes, with the fluctuation defined as follows:

$$T' = T - T_{avg} \quad (3)$$

where T' is the instantaneous temperature fluctuation from the mean temperature, and

$$\frac{\overline{T'}}{\Delta T} = \frac{\sqrt{\frac{\sum (T')^2}{N}}}{(T_{plenum} - T_{\infty})} \quad (4)$$

where $\overline{T'}$ is the root sum square of temperature fluctuations and is normalized by $(T_{plenum} - T_{\infty})$. The agreement between the two probes is again very good. As expected, the regions of high fluctuation are in the shear layers of the jet and crossflow, while low fluctuations are seen in the freestream approach and jet core.

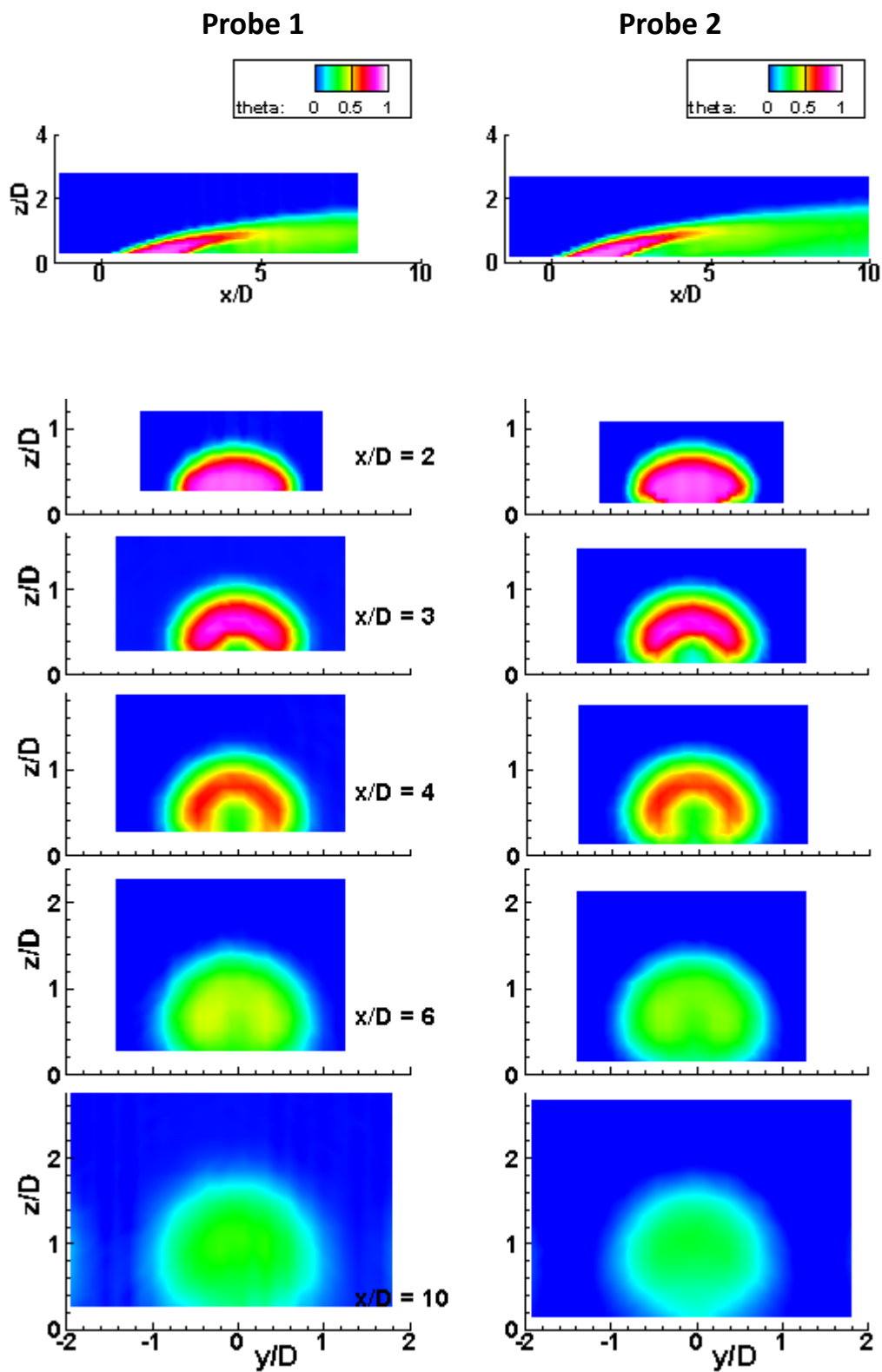


Figure 6.—(a) Normalized temperature θ for Probe 1 and Probe 2 at streamwise and spanwise survey planes, $BR = 1.2$.

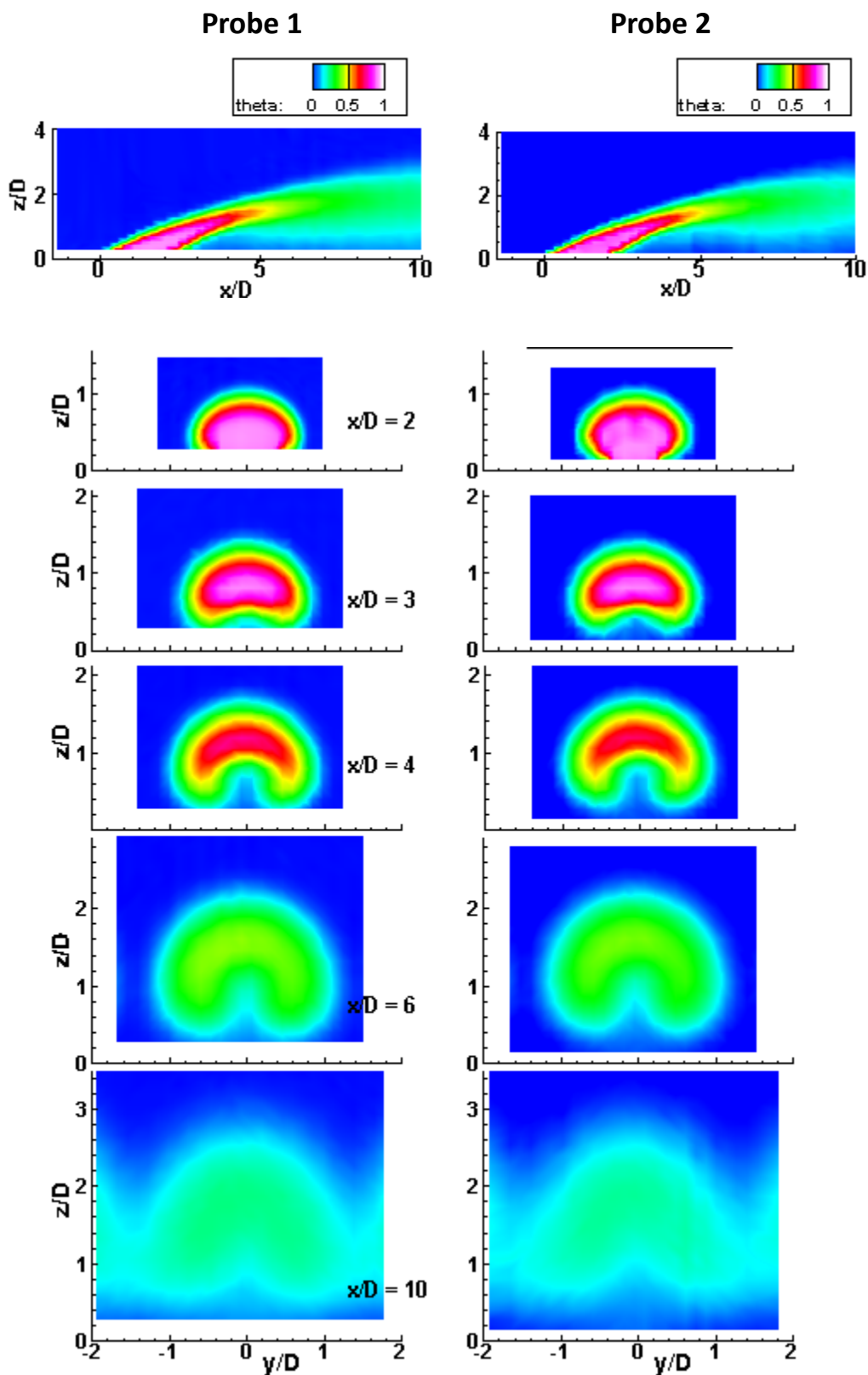


Figure 6.—(b) Normalized temperature θ for Probe 1 and Probe 2 at streamwise and spanwise survey planes, $BR = 2.4$.

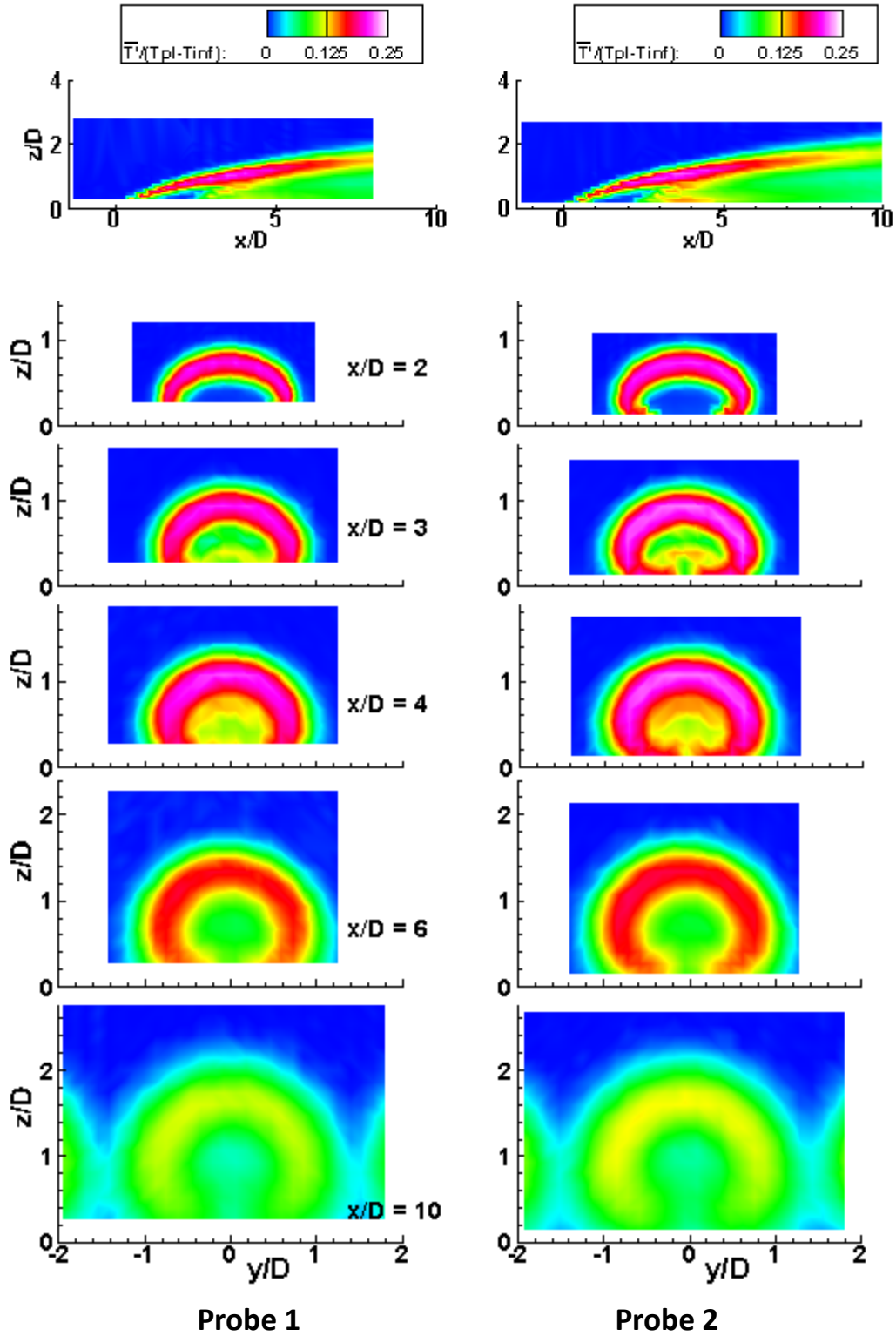


Figure 7.—(a) Normalized temperature fluctuations $\bar{T}/\Delta T$ for Probe 1 and Probe 2 at streamwise and spanwise survey planes, $BR = 1.2$.

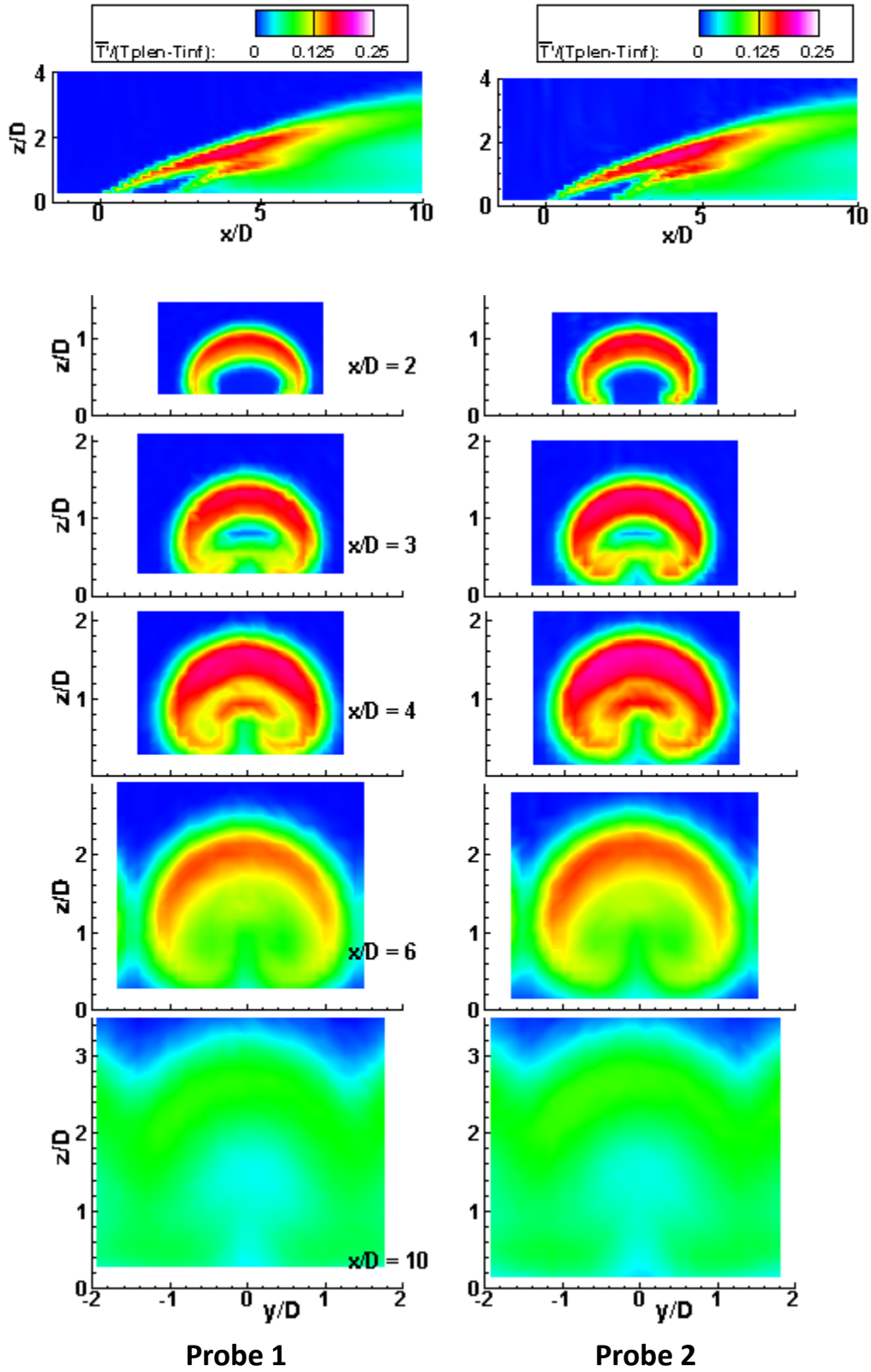


Figure 7.—(b) Normalized temperature fluctuations $\bar{T}'/\Delta T$ for Probe 1 and Probe 2 at streamwise and spanwise survey planes, $BR = 2.4$.

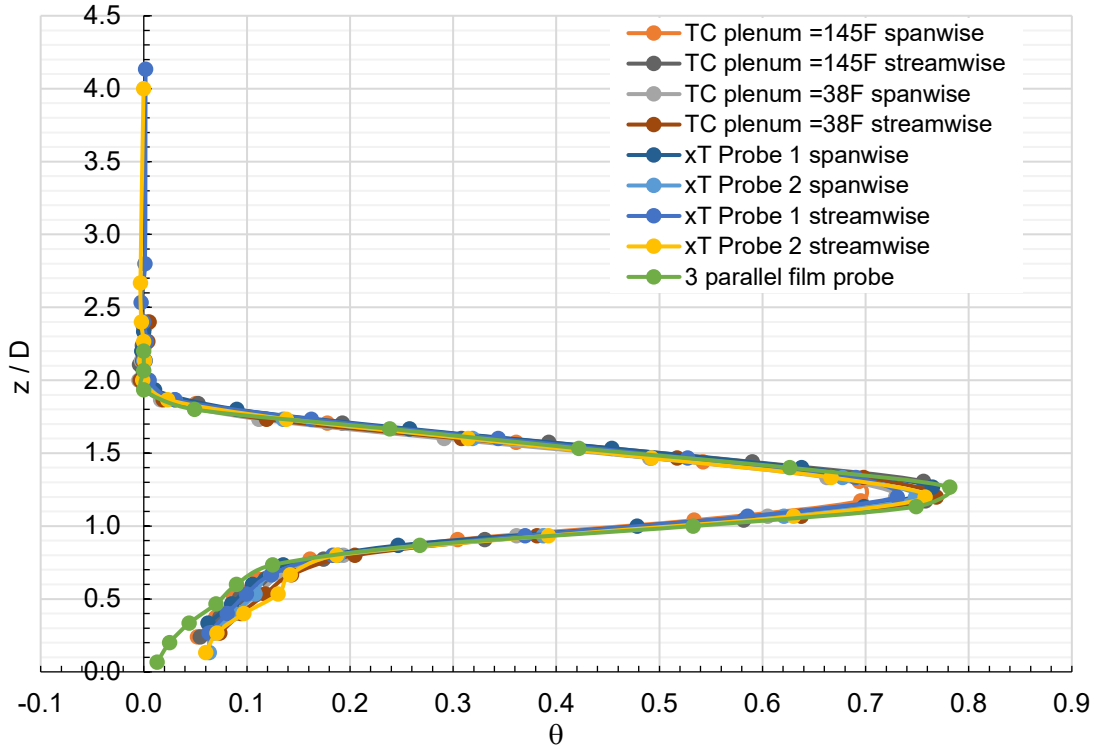


Figure 8.—Comparison of midspan mean temperature profiles at $x/D = 4.0$ for nominal $BR = 1$.

As further indication of the mean temperature measurement consistency, Figure 8 shows midspan mean temperature profiles measured from Probes 1 and 2 along with some previously measured hot film and thermocouple data in the same facility for both a heated and cooled jet. These profiles are taken from various nominally $BR = 1$ survey data sets and are at a midspan location 4 diameters downstream of the film cooling holes. The data is consistent across the various wires and thermocouples. Additionally, little difference is seen between heated jet and the cold jet data. The only major areas of discrepancy are very near the wall and around the peak temperature at $z/D = 1.2$. The various probe sizes and orientations affect the temperature resolution in these areas. All the temperature survey data generally shows this consistency at all measurement planes.

Surface Heat Transfer Measurements

Surface heat transfer measurements were acquired on a test plate with an Inconel foil attached to the plate with a thin thermochromic liquid crystal coating. The heat transfer coefficient was calculated by the equation

$$h = \frac{q}{T_{LCsurface} - T_{\infty}} \quad (5)$$

The heat flux q was determined from the power applied to the Inconel sheet and the airstream and plenum temperature were kept the same for the heat transfer tests. Nusselt number was calculated as

$$Nu = \frac{hL_w}{k} \quad (6)$$

where L_w is the 8.15in. (207 mm) side wall, k is thermal conductivity of air. Note that these surface measurements were taken on a similar configuration and conditions as the survey measurements. Figure 9 shows contour plots of Nusselt number on the surface of the test plate downstream of the cooling holes for nominal blowing ratios of 1 and 2. Recall that the foil heater sheet begins at the trailing edge of the holes for the heat transfer model; the unheated starting length results in very high heat transfer coefficients at the foil edge. Generally, we see that the film jet increases the heat transfer behind the holes, but the effect tapers off moving downstream. Jet lift-off directly behind the hole and reattachment is evident at the higher blowing ratio.

Surface temperature measurements were also acquired employing an infrared camera. Film cooling effectiveness was defined as:

$$\eta = \frac{(T_\infty - T_{IRsurface})}{(T_\infty - T_{plenum})} \quad (7)$$

where T_∞ is the temperature of the freestream tunnel air. Figure 10 shows film cooling effectiveness maps along with centerline values of film cooling effectiveness averaged over a span of one pitch (± 0.5 pitch). The film effectiveness is higher for $BR = 1$ compared with $BR = 2$. This agrees with the temperature survey data seen in Figure 6 with $BR \sim 1$ showing the jet staying attached better than for $BR \sim 2$, and thus providing much better film protection of the surface from the free stream gas temperature. Note that heat transfer maps are different from the effectiveness plots; higher heat transfer can be caused by higher mixing which would be detrimental to good film effectiveness. More details of the film cooling jet flow are discussed below in flow field measurements.

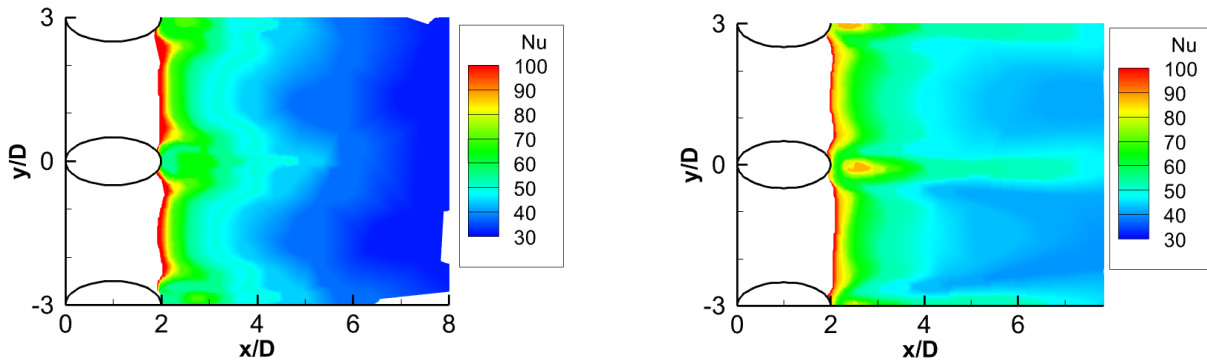


Figure 9.—Surface Nusselt number from liquid crystal for $BR = 1$ (left) and $BR = 2$ (right).

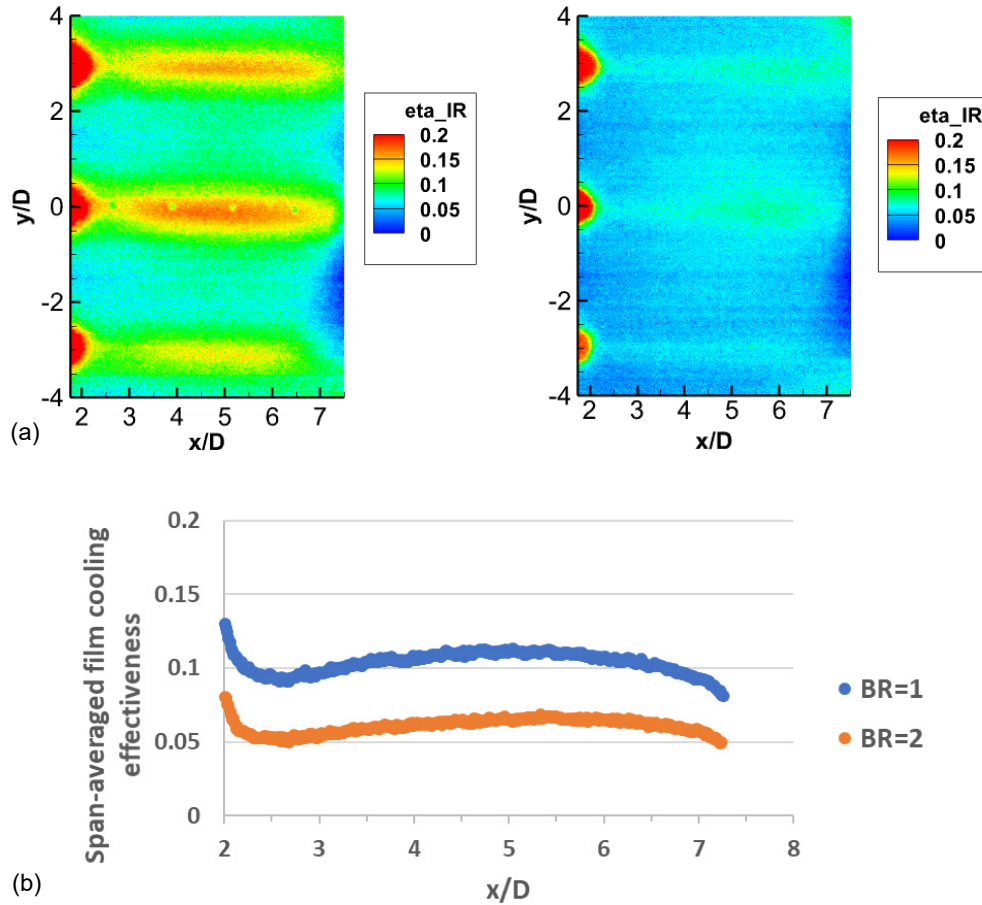


Figure 10.—(a) Surface film cooling effectiveness from infrared thermography for $BR = 1$ (left) and $BR = 2$ (right). (b) Centerline span-averaged film cooling effectiveness from infrared thermography for $BR = 1$ and $BR = 2$.

Velocity Measurements

Individual velocity components were determined from the xT probe surveys. Figure 11 shows a contour plot of the Probe 2 streamwise velocity component normalized by the averaged tunnel velocity, u/U_∞ , at the spanwise plane $x/D = -8.3$ upstream of the holes. The edge of the boundary layer is seen to be about $z/D = 0.65$.

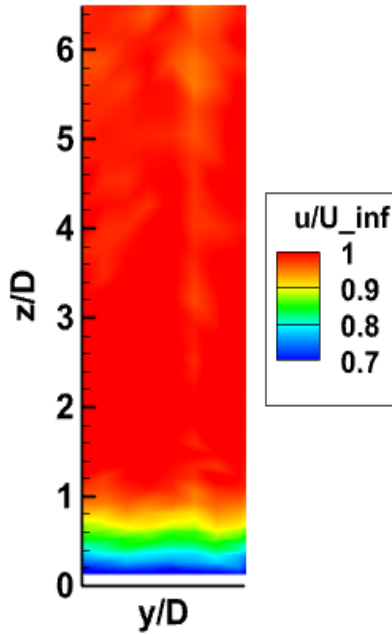


Figure 11.—Velocity profile at $x/D = -8.3$ using xT Probe 2.

Contour plots of the streamwise velocity component along the centerline and spanwise planes downstream of the jet at $x/D = 2, 3, 4, 6, 10$ for both xT probes are shown in Figure 12 for $BR = 1.2$ and 2.4 . The data for both blowing ratio cases from the two probes agree fairly well, although localized differences are evident, especially for $BR = 1.2$. Both probes show the same general jet-in-crossflow behavior. From the streamwise plots, we see the jet lifting the approaching boundary layer and the jet penetrating into the freestream. The spanwise surveys downstream of the hole show the typical kidney vortex pattern developing and then dissipating moving downstream. Near the hole, the jet flows are highly three-dimensional, and the results vary somewhat depending on which probe is being used.

For $BR = 1.2$ data, Probe 2, which picks up the vertical velocity component as well as streamwise velocity, shows the jet protruding further downstream near $x/D > 5$ in the centerline plots. In the spanwise plots, Probe 1 shows slightly higher magnitudes relative to Probe 2 in the core of the jet, but these are generally within the measurement uncertainty. The slight discrepancy in the shape of the contours, with the spanwise profile of Probe 1 more flattened than that shown by Probe 2, can be attributed to the probe wire orientation and probe volume. Recall that Probe 1 has horizontal wires for measuring velocity and is primarily useful for streamwise and spanwise flow components, so any jet flows with strong vertical components will actually create a resultant streamwise-vertical velocity with a magnitude slightly higher than one would see from solely a streamwise component. This can be seen in the $x/D = 2$ and $x/D = 3$ planes, with the higher magnitude in the core of the jet where there is a predominant streamwise-vertical velocity. Probe 2 has vertical wires and measures streamwise and vertical components. These probe effects are diminished further downstream as the mixing between the jet and the surrounding flow increases and the discrepancy becomes imperceptible. These discrepancies are also diminished in the $BR = 2$ data due to the larger jet velocity in the streamwise direction.

The asymmetry seen in Probe 2 is likely due to survey data point resolution as well as the bias in the vertical flow seen by each of the velocity wires of the probe, i.e., one wire sees a slightly different velocity than its adjacent wire (0.1 in. spacing) as the probe traverses through the jet. The lack of asymmetry in the temperature contours in Figure 6 and Figure 7 supports the idea that no physical flow

bias exists, and this is a result of the limitations of the measurement probes. Again, for $BR = 2$ where the streamwise velocity component is larger, the asymmetry of Probe 2 is diminished. It is felt that the more vertical flow areas near the outer edges of the jet are better described by Probe 2, while the more spanwise flow areas near the top of the jet are better described by Probe 1. Further details of the effects of probe wire orientation can be found in Appendix C.

Figure 13 shows the fluctuating streamwise velocity component, \bar{u}' , for both Probe 1 and Probe 2, normalized by U_∞ . \bar{u}' is defined as

$$\bar{u}' = \sqrt{\frac{\sum (u_i - u_{avg})^2}{N}} \quad (8)$$

where u_i is the instantaneous sample velocity, u_{avg} is the averaged velocity of all the points in the sample, and N is the number of points taken in the sample. Similar to the fluctuating temperature data, the velocity fluctuation contours are again generally consistent between data obtained with the different probes, especially downstream where the flow is more uniform in the x direction and less three-dimensional. The general shapes are consistent, showing high fluctuation values in the shear layers, but the maximum magnitudes from each probe are different. For example, for the $BR = 1.2$ data, Probe 2 shows maximum fluctuations higher than Probe 1. In the centerline plot at $BR = 1.2$ near the floor around $x/D = 4$ is a noticeable difference, in which Probe 2 shows slightly higher magnitudes just downstream of the hole exit. The orientation of the wires and probe supports may contribute to these discrepancies of the fluctuations. See Appendix C for probe comparison details.

Secondary flow components contribute to the development of the kidney vortex produced from the injected flow of an inclined round hole. The normalized mean values are defined as v/U_∞ and w/U_∞ , and normalized fluctuation values as

$$\frac{\bar{v}'}{U_\infty} = \frac{\sqrt{\frac{\sum (v_i - v_{avg})^2}{N}}}{U_\infty} \quad (9)$$

$$\frac{\bar{w}'}{U_\infty} = \frac{\sqrt{\frac{\sum (w_i - w_{avg})^2}{N}}}{U_\infty} \quad (10)$$

Figure 14 and Figure 15 show the development of these velocities and their fluctuations of the jet as it progresses downstream. The jet moves upward and outward as it exits the hole. The main flow is forced up and then wraps around the outside of the jet. It is entrained down around the jet and then up through the middle of the jet wake. The strength of the secondary flow components gradually die out as the jet moves downstream. The high values of the fluctuations, u' , v' and w' , are found in the high shear areas of the jet mixing with the free stream main flow. The centerline v -component is expected to have an average value near 0, which is generally true as the values are quite low.

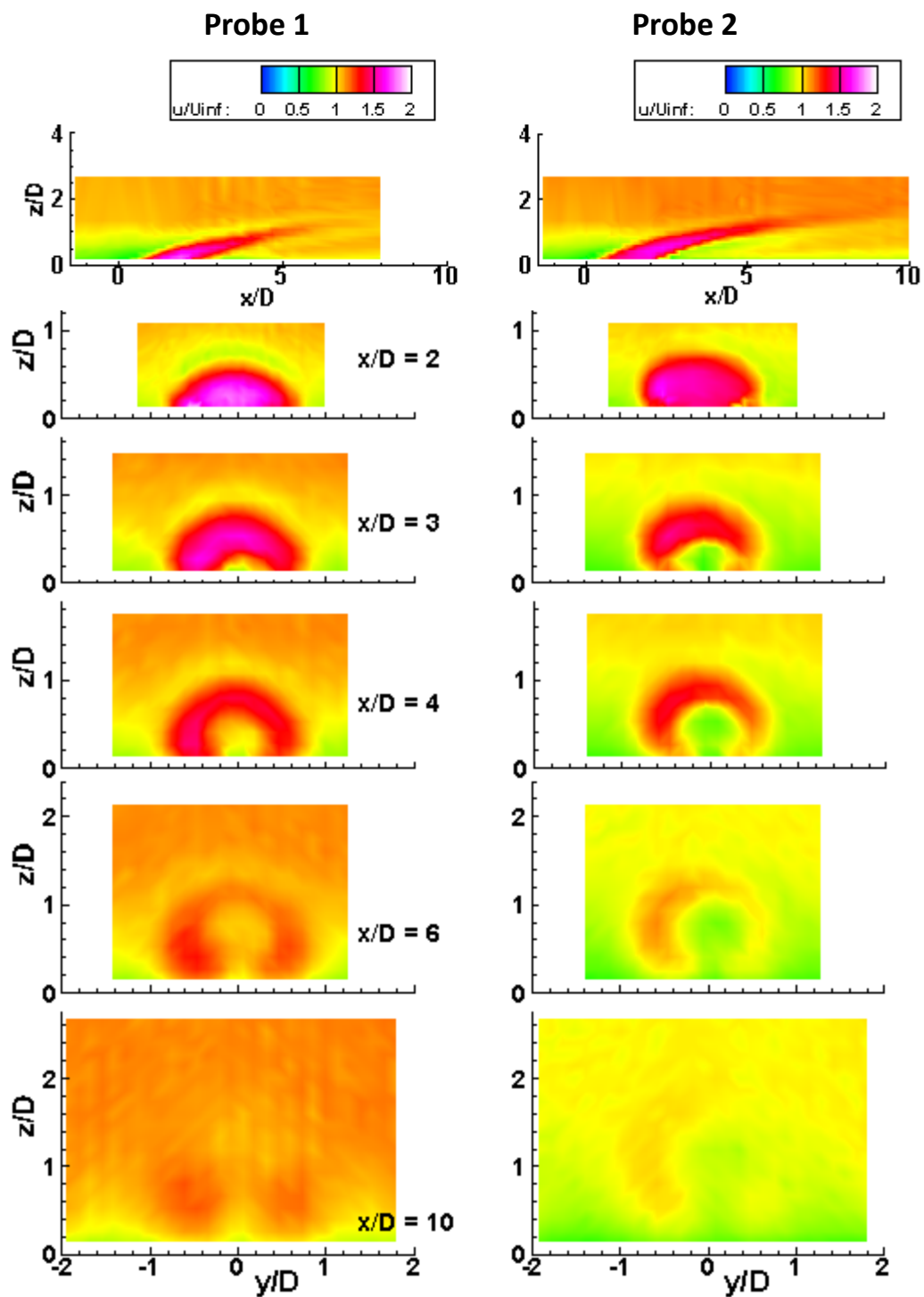


Figure 12.—(a) Normalized u -component velocity for Probe 1 and Probe 2 at streamwise and spanwise survey planes, $BR = 1.2$.

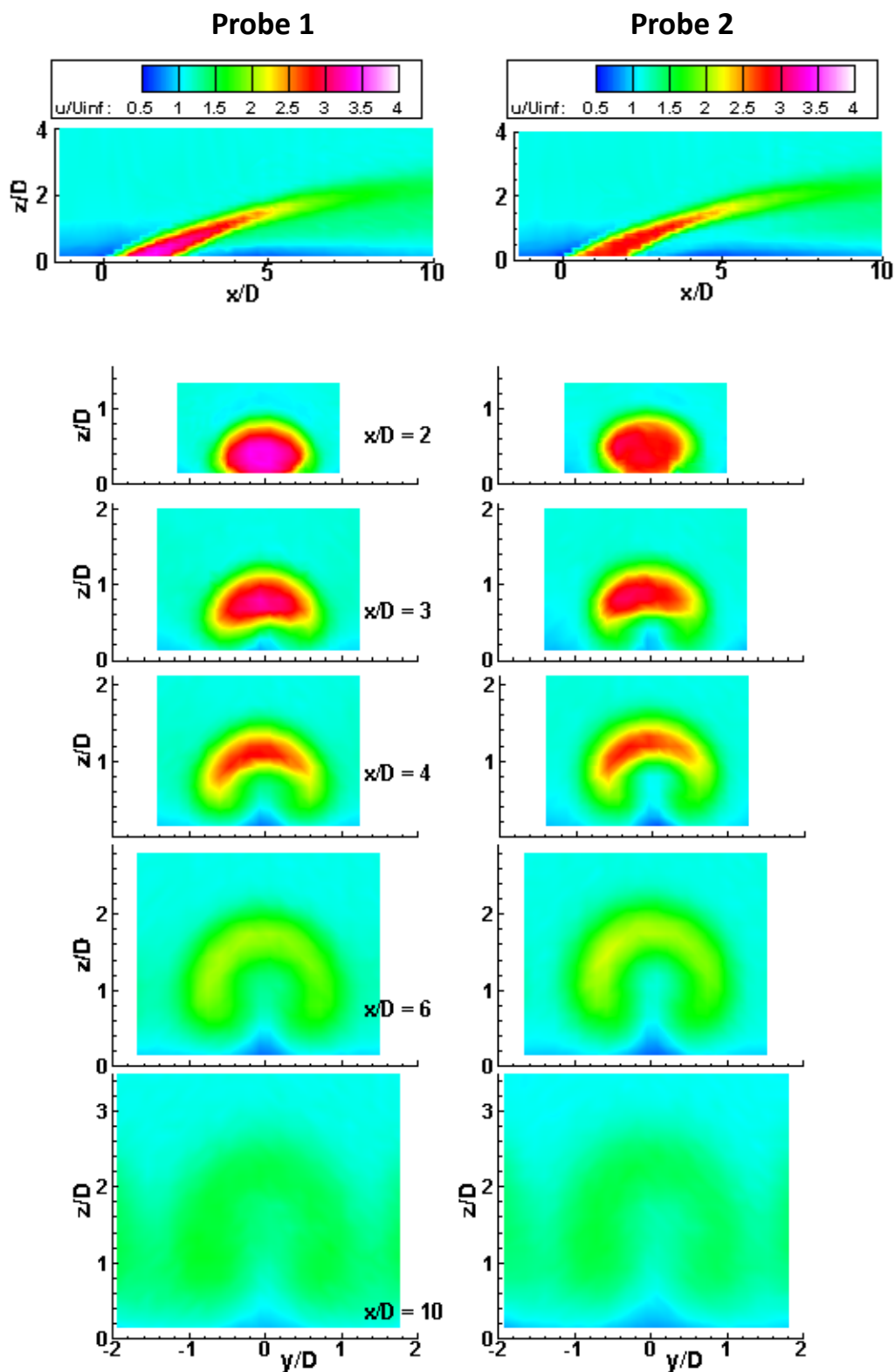


Figure 12.—(b) Normalized u -component velocity for Probe 1 and Probe 2 at streamwise and spanwise survey planes, $BR = 2.4$.

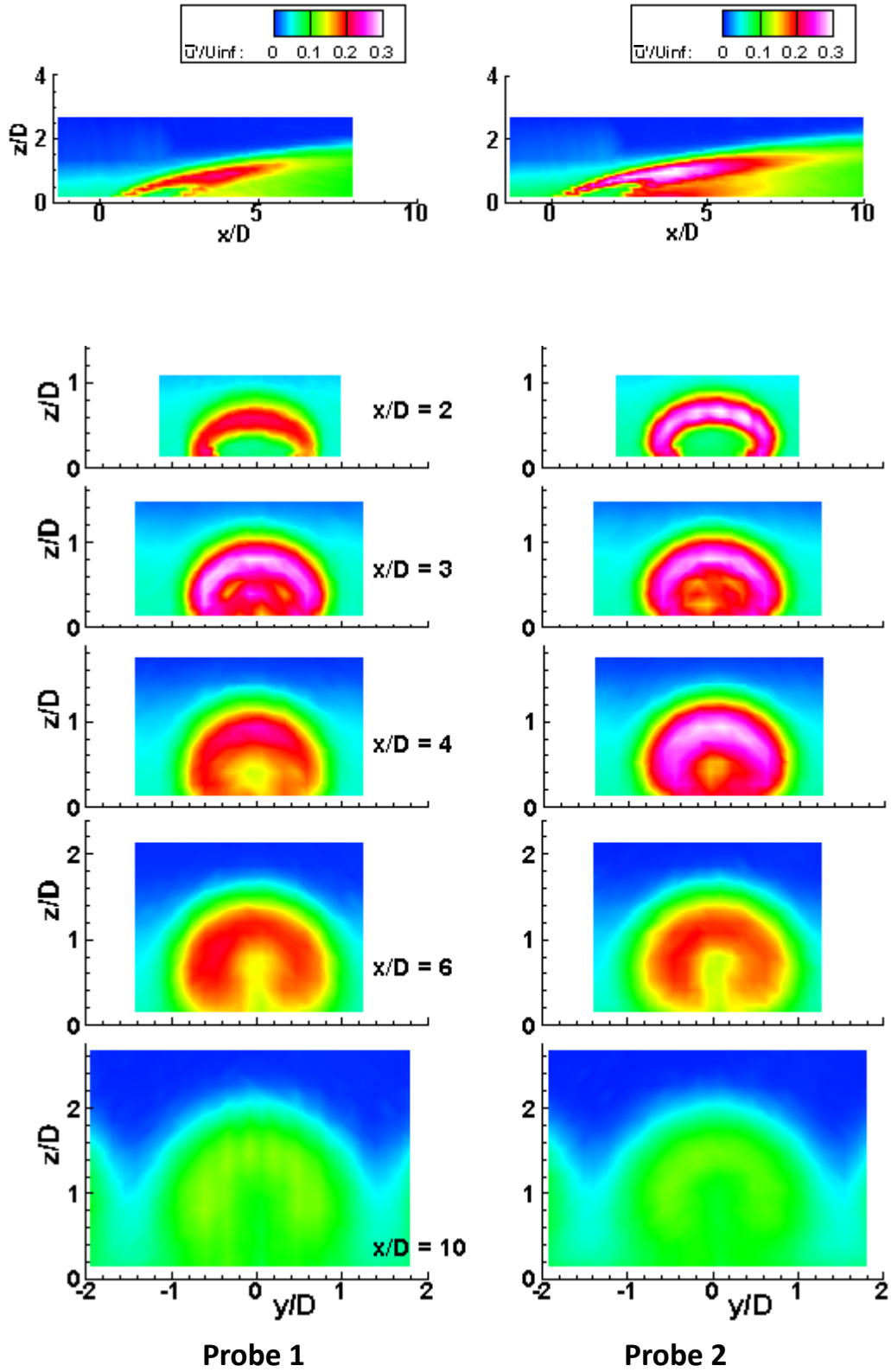


Figure 13.—(a) Normalized streamwise velocity component fluctuations \bar{u}'/U_{∞} for Probe 1 and Probe 2 at streamwise and spanwise survey planes, $BR = 1.2$.

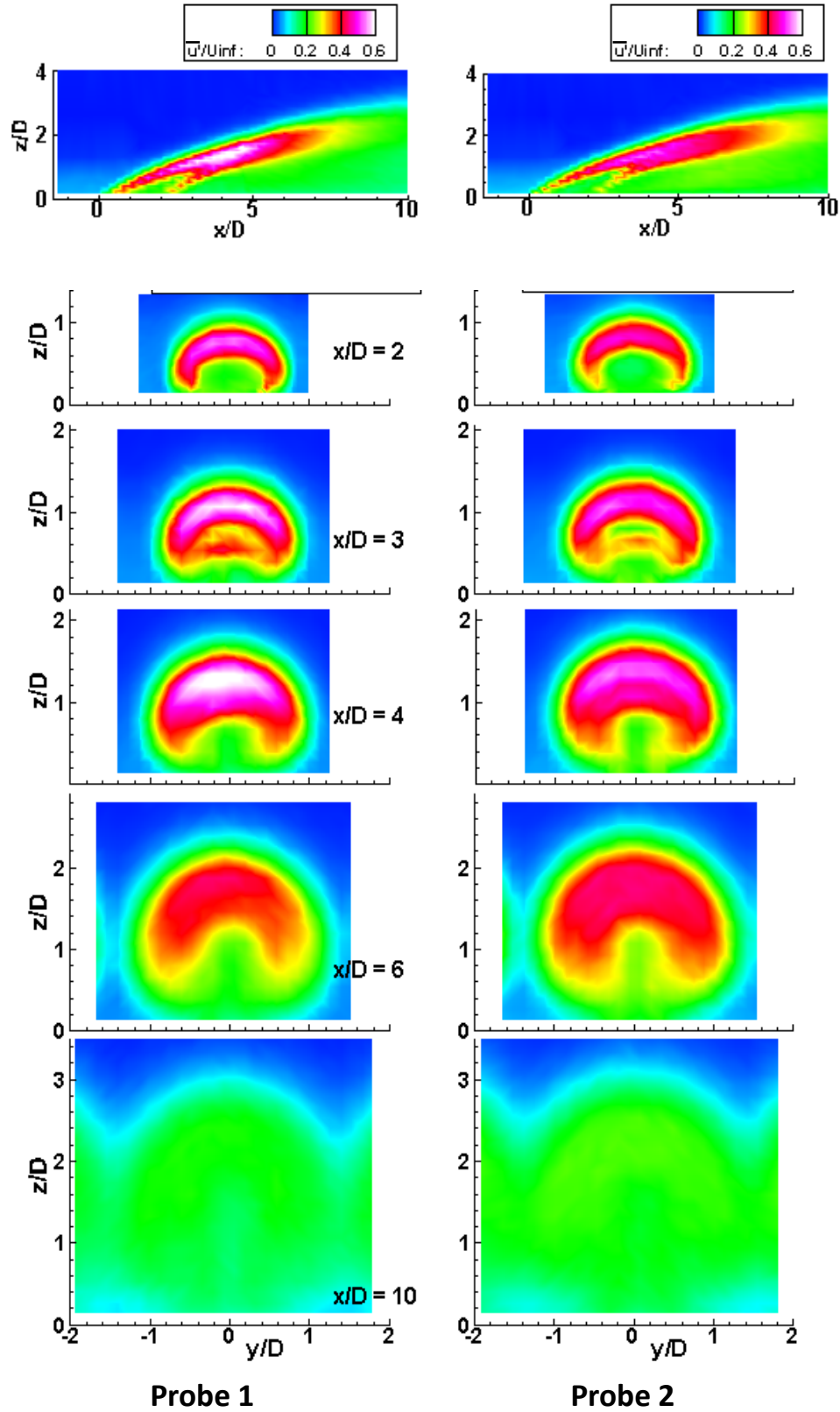


Figure 13.—(b) Normalized streamwise velocity component fluctuations \bar{u}'/U_∞ for Probe 1 and Probe 2 at streamwise and spanwise survey planes, $BR = 2.4$.

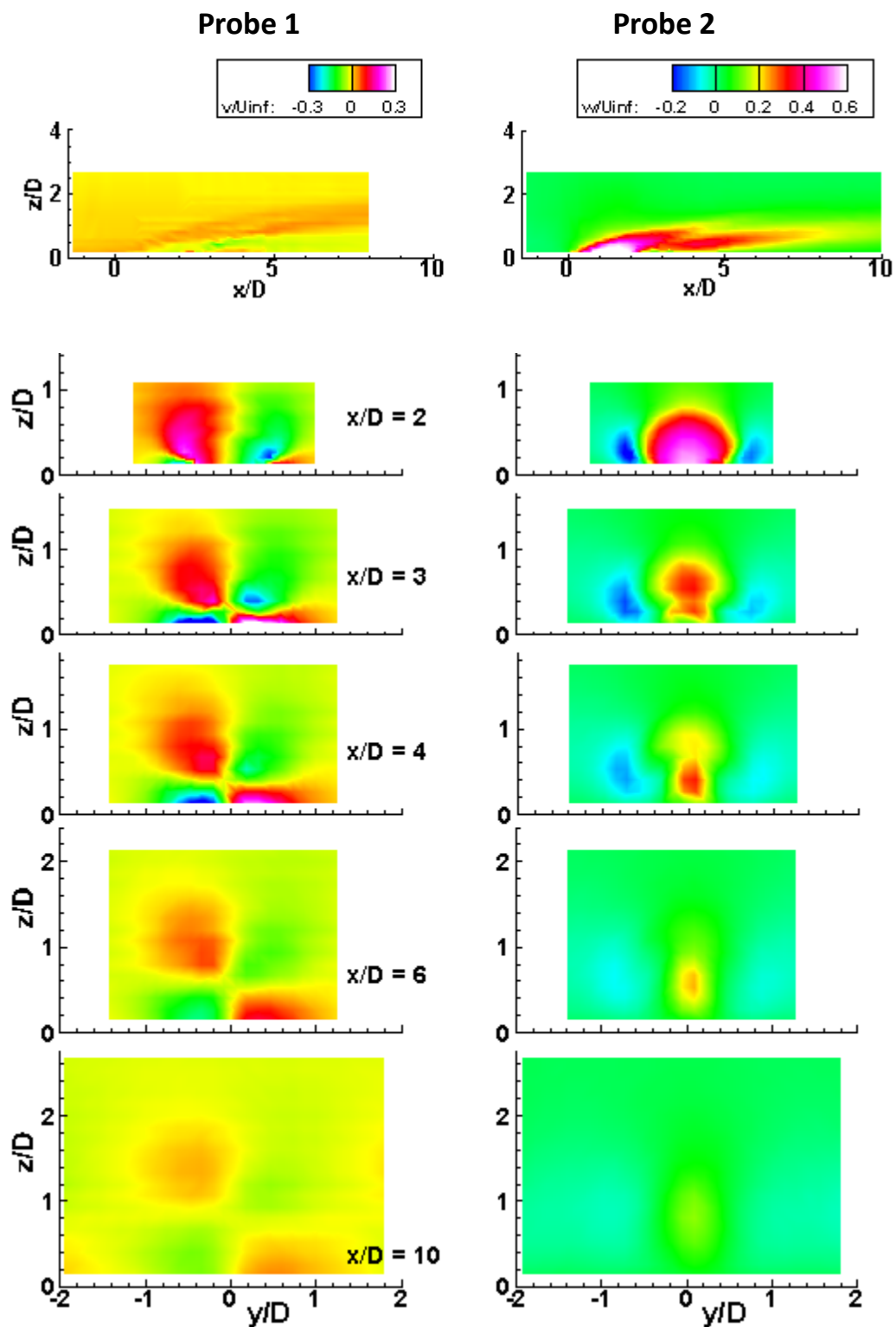


Figure 14.—(a) Normalized v - and w -component velocity for Probe 1 and Probe 2 at streamwise and spanwise survey planes, $BR = 1.2$.

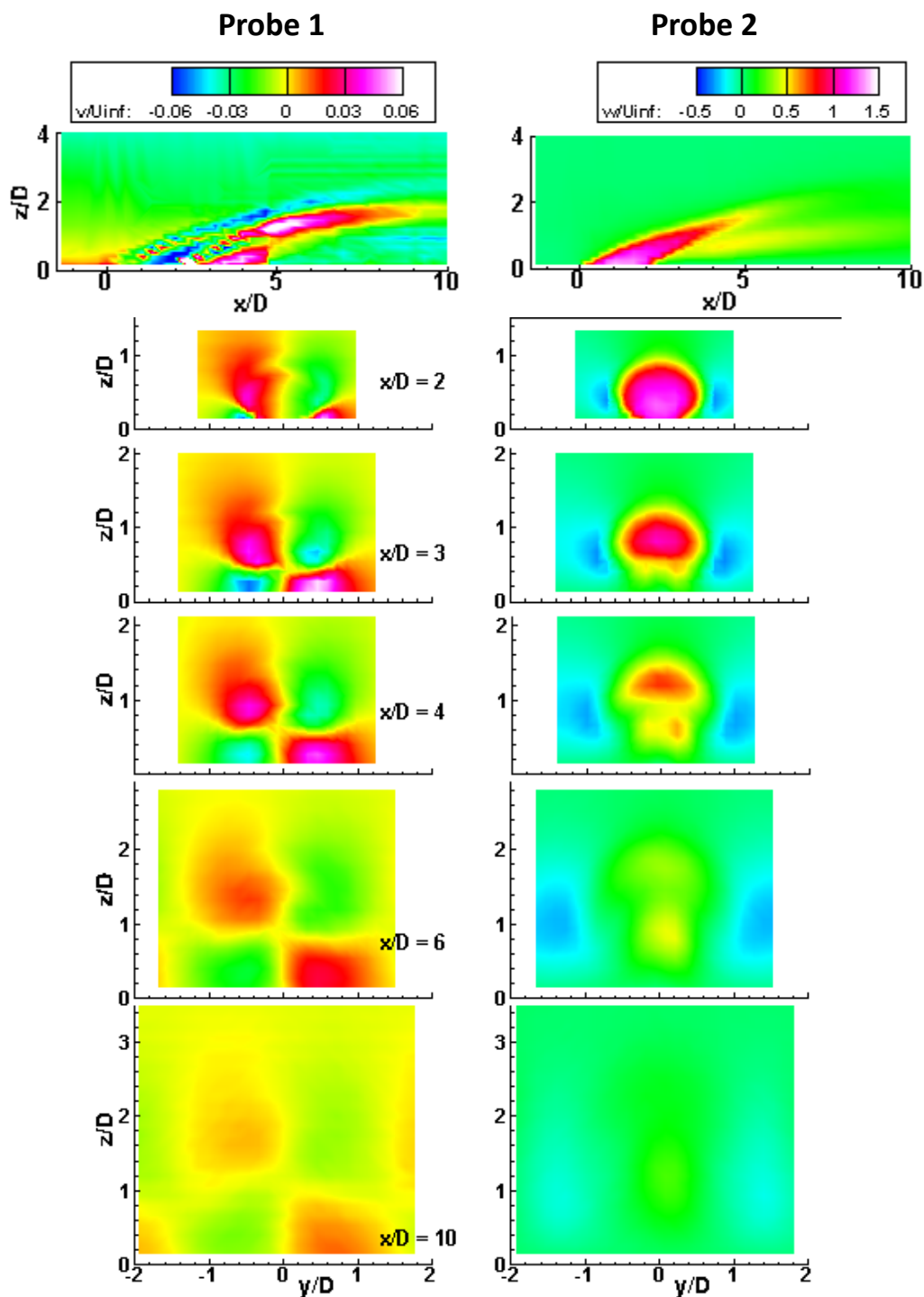


Figure 14.—(b) Normalized v - and w -component velocity for Probe 1 and Probe 2 at streamwise and spanwise survey planes, $BR = 2.4$

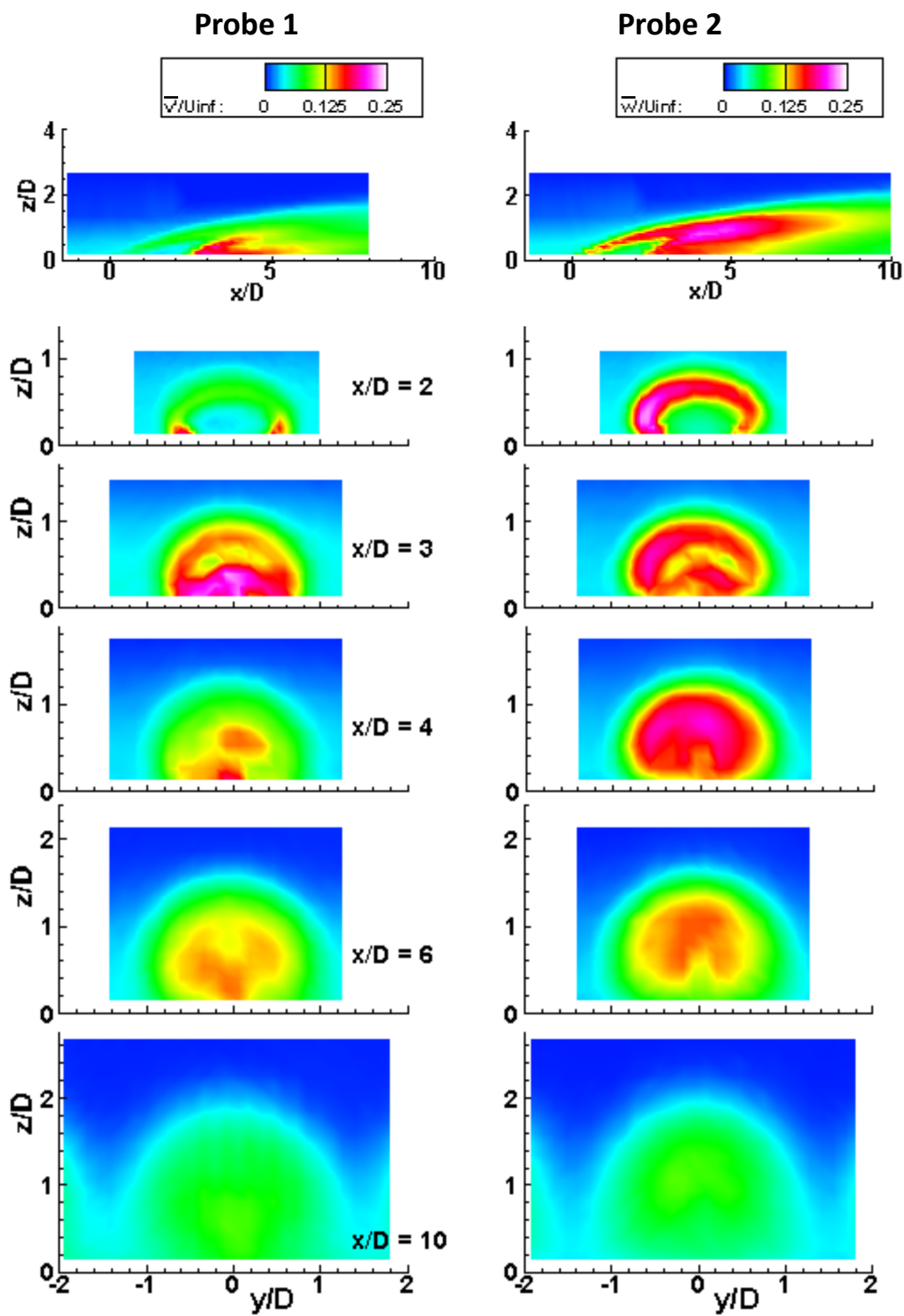


Figure 15.—(a) Normalized velocity component fluctuations \bar{v}'/U_{∞} and \bar{w}'/U_{∞} for Probe 1 and Probe 2 at streamwise and spanwise survey planes, $BR = 1.2$.

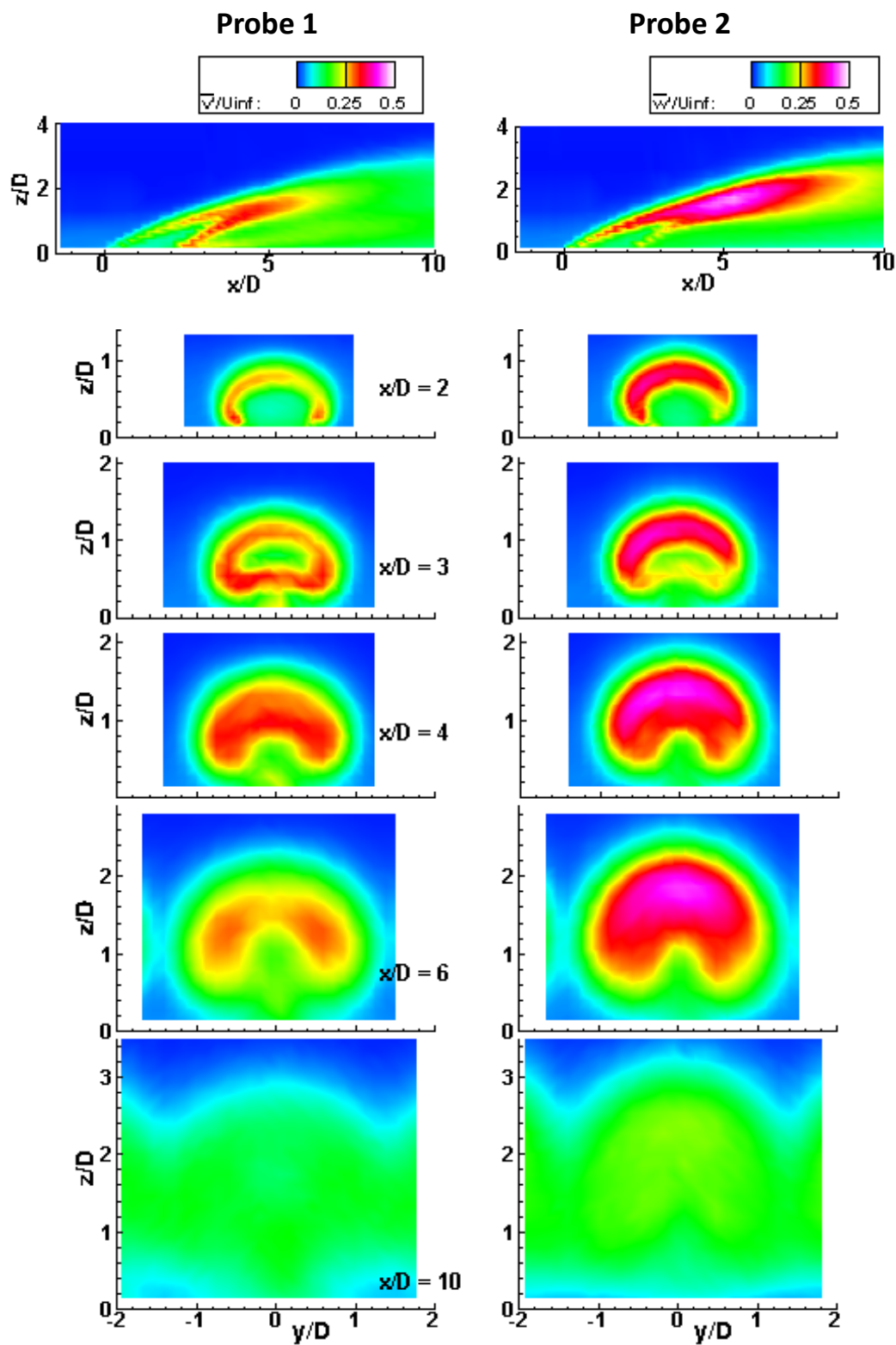


Figure 15.—(b) Normalized velocity component fluctuations \bar{v}'/U_{∞} and \bar{w}'/U_{∞} for Probe 1 and Probe 2 at streamwise and spanwise survey planes, $BR = 2.4$.

Turbulence Quantities

Figure 16 shows percent velocity turbulence intensity measured separately with each probe at the various survey planes and both blowing ratios. Turbulence intensity is defined with local mean velocity as:

$$Tu = \frac{u'}{u} \times 100\% \quad (11)$$

Note that each probe only measures two velocity components, thus the values are not expected to agree where the vertical and spanwise components are relatively strong but agree very well downstream where the u -component dominates. As expected, high turbulence is seen in the shear layers of the flow. Just downstream of the jet, turbulence levels are above 20 percent near the floor where the vortices wrap around and converge. The higher turbulence shown from Probe 2 for $BR = 1.2$ follows from the higher velocity fluctuations, showing a strong vertical velocity in the shear layer. For $BR = 2.4$, the differences between the probes are less pronounced.

Length Scale Measurements

The integral length scale is related to the size of the largest eddies in the flow. Nondimensional integral length scale (macroscale) values are shown in Figure 17, with the integral length scale (noted as ILS in the figure legend) defined as

$$\Lambda_x = ILS = \left[\frac{E(f)U_{mean}}{4u'^2} \right]_{f \rightarrow 0} \quad (12)$$

where E is energy, f is frequency, and u' is the standard deviation of the u -component of velocity. The ILS/D values upstream of the holes is around 0.35, which is on the order of the dimensions of the upstream flow conditioning. Near the hole exit, the macroscale values are near 1, the same as the diameter of the cooling hole. Downstream of the jet, the macroscale is on the order of 0.1. The integral length scale is diminished due to mixing in the shear layers with the freestream, with the larger eddies breaking down into smaller eddies. The biggest difference between the two probes is in the jet coming out of the hole, with Probe 1 indicating more spanwise influence in the jet. Note that the high streaks in the upper freestream are related to the survey density and are not considered.

Nondimensional dissipative length scale (microscale) values are shown in Figure 18, with the dissipative length scale (noted as DLS in the figure legend) defined as

$$\frac{1}{\lambda_x^2} = \frac{1}{DLS^2} = \frac{2\pi^2}{U^2 u'^2} \int_0^\infty f^2 E(f) df \quad (13)$$

The dissipation length scale is smaller than the integral length scale and is independent of the geometry. Differences between the probes are most notable for $BR = 1.2$ in the jet and downstream of the hole. Freestream values of DLS/D are on the order of 0.02 and are consistent with previous measurements reported in Reference 13. Mixing of the shear layers in the jet results in slightly higher values around 0.05 downstream of the hole. The highest values are upstream of the jet near the floor and in the jet, with values near 0.1.

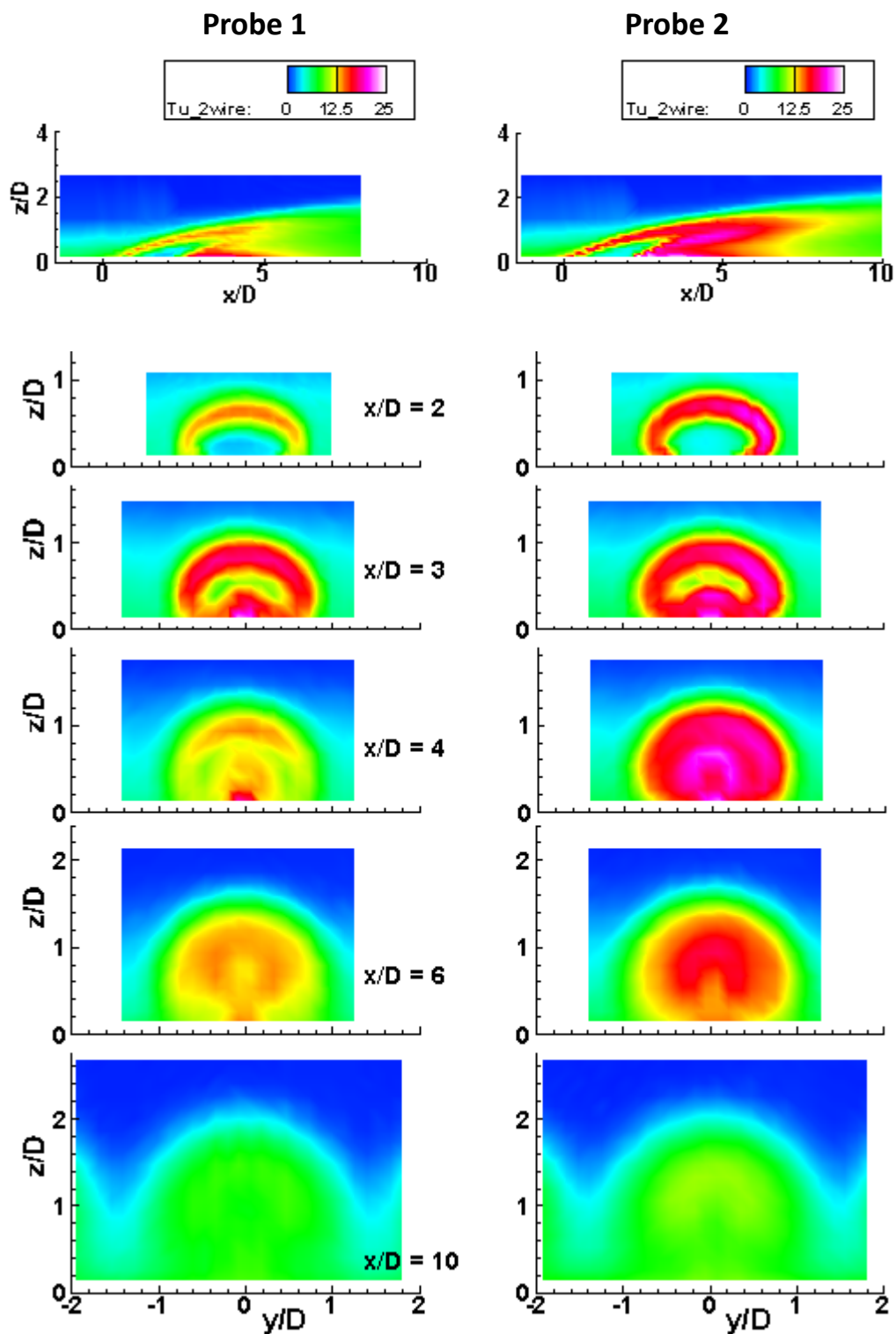


Figure 16.—(a) Percent turbulence intensity (2-wire measurements) for Probe 1 and Probe 2 at streamwise and spanwise survey planes, $BR = 1.2$.

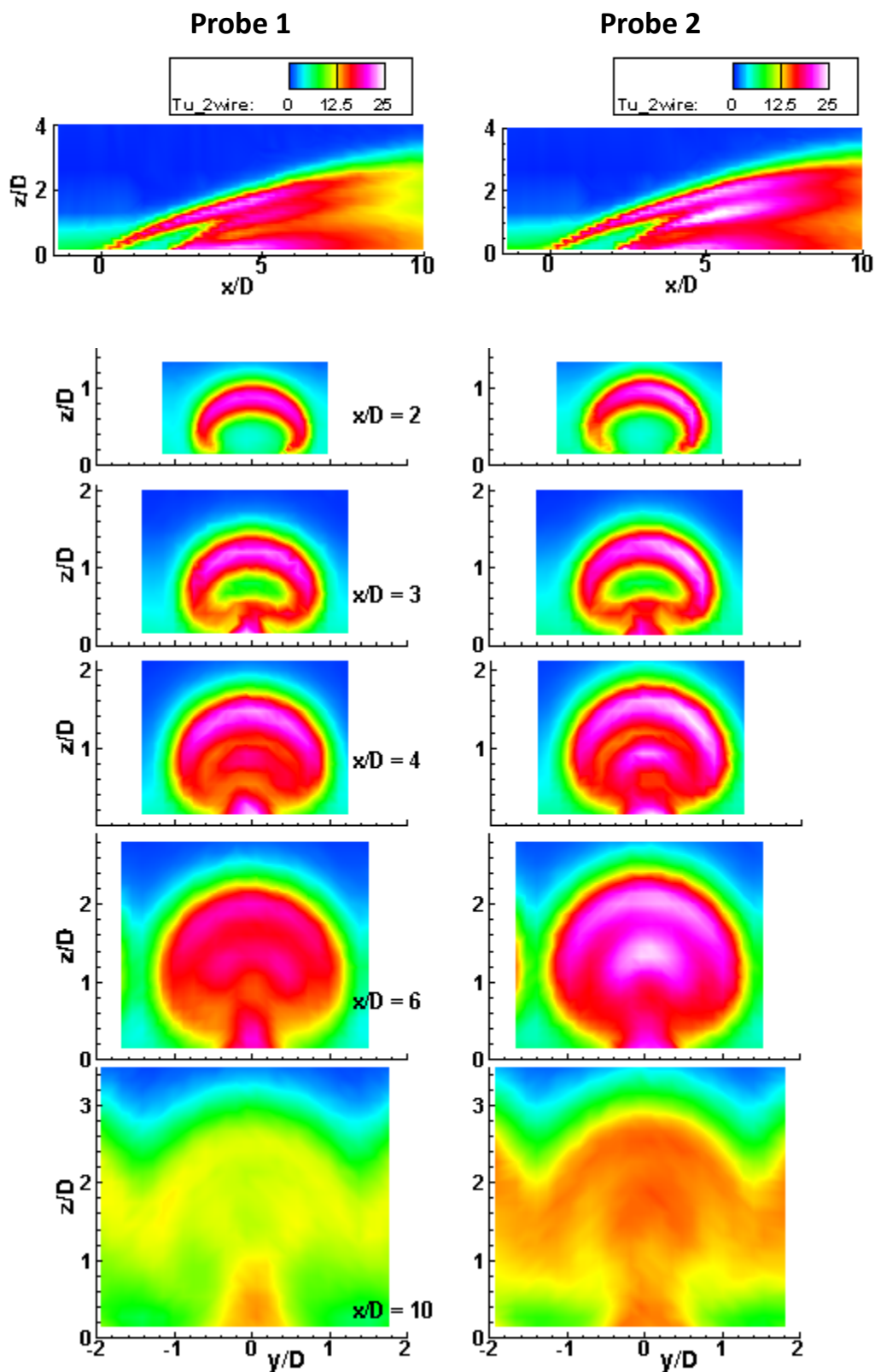


Figure 16.—(b) Percent turbulence intensity (2-wire measurements) for Probe 1 and Probe 2 at streamwise and spanwise survey planes, $BR = 2.4$.

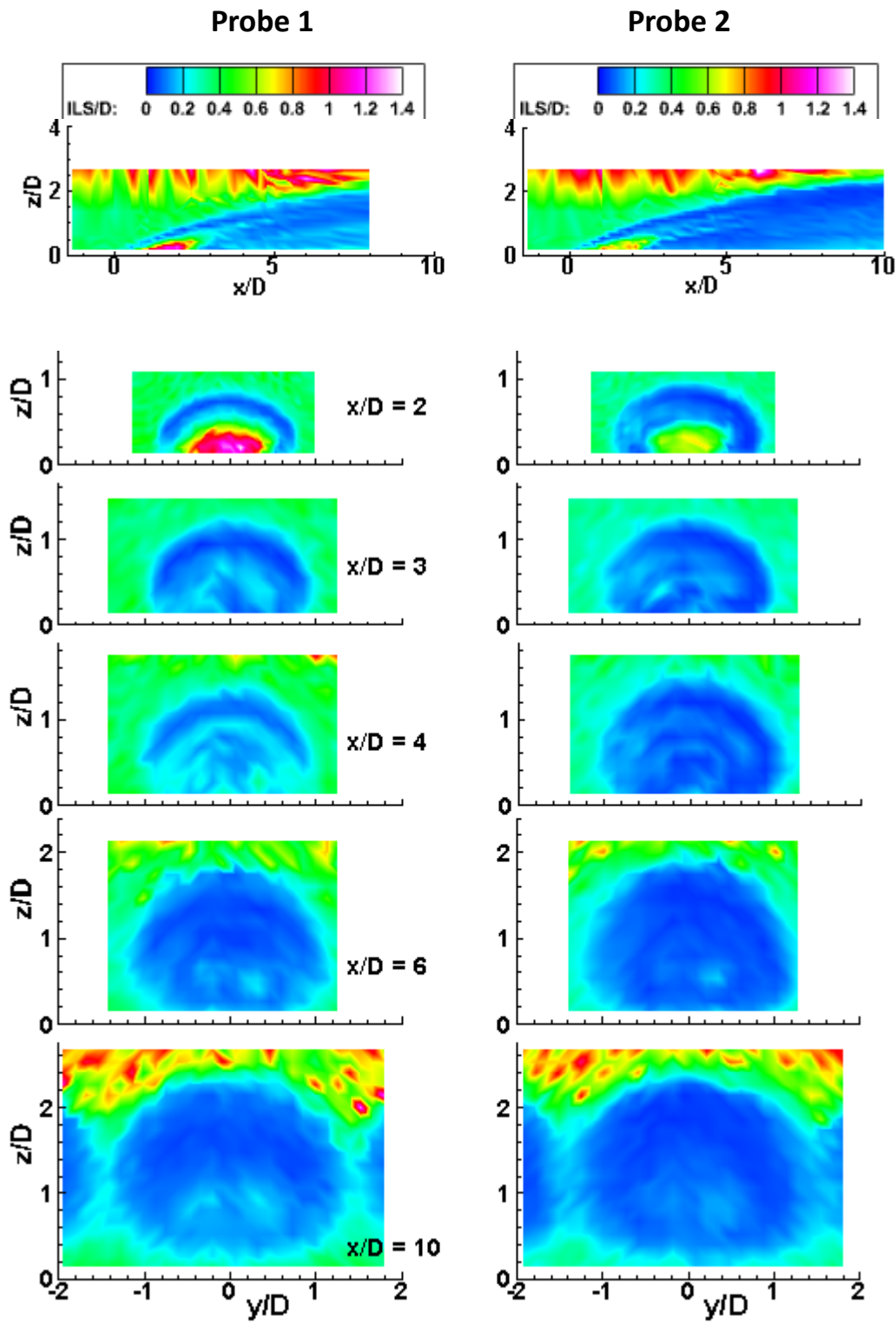


Figure 17.—(a) Normalized integral length scale Λ_x for Probe 1 and Probe 2 at streamwise and spanwise survey planes, $BR = 1.2$.

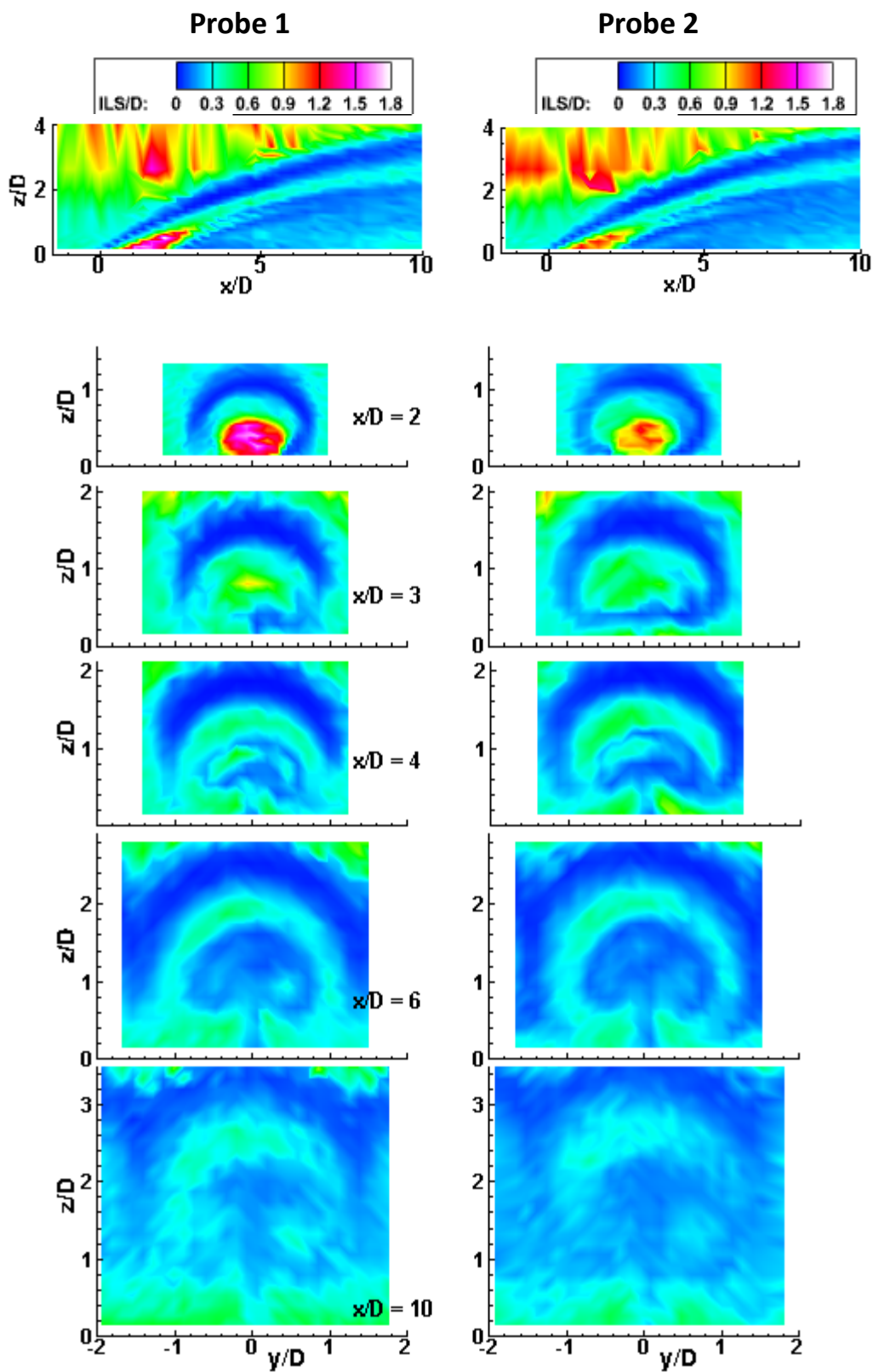


Figure 17.—(b) Normalized integral length scale Λ_x for Probe 1 and Probe 2 at streamwise and spanwise survey planes, $BR = 2.4$.

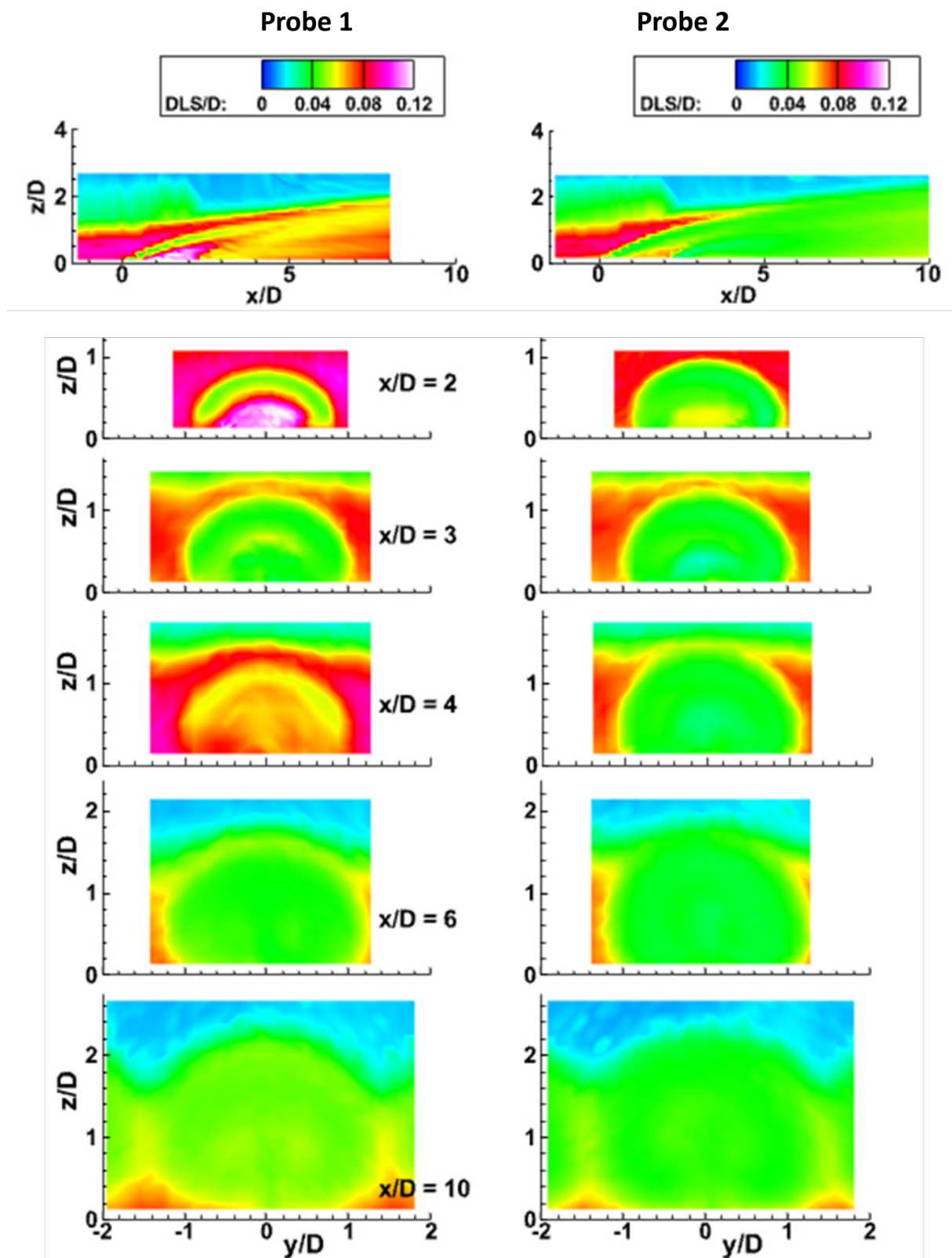


Figure 18.—(a) Normalized dissipative length scale λ_x for Probe 1 and Probe 2 at streamwise and spanwise survey planes, $BR = 1.2$.

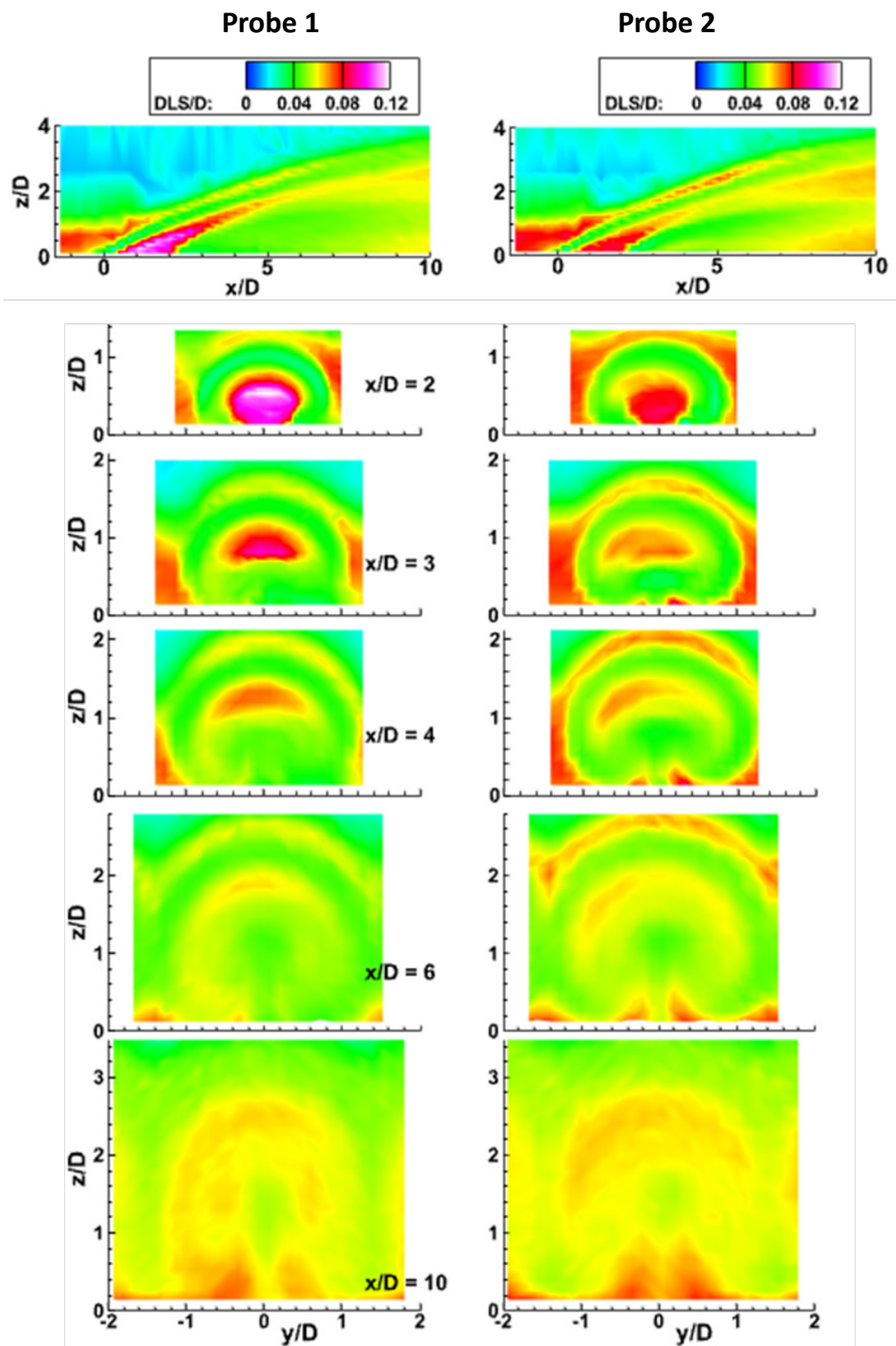


Figure 18.—(b) Normalized dissipative length scale λ_x for Probe 1 and Probe 2 at streamwise and spanwise survey planes, $BR = 2.4$

Reynolds Stress

The mean Reynolds stress parameters $u'v'$ and $u'w'$ are shown in Figure 19 for both blowing ratios. These figures show various layers and regions of positive and negative correlation throughout the flow field, and it should be noted that the probe volumes employed in this study limit the spatial resolution of these various layers. Still these Reynolds stress measurements give some insight into the flow interactions between the inclined jet and freestream main flow. As the jet exits the floor at a 30° incline, it pushes up and out against the freestream flow and entrains some of the freestream down and under the jet core, especially at higher blowing ratios. Recall that the largest velocity fluctuations appear near the jet especially at the jet-freestream interfaces, indicating high turbulent shear stress.

Examining the Probe 2 data (which measures correlation of the streamwise and vertical velocity components), strong positive $u'w'$ correlations are seen near the jet top as it flows up into freestream, and negative $u'w'$ correlations are evident as the flow wraps around the core on the outside.

Similarly, in the Probe 1 data (which measures correlation of the streamwise and spanwise velocity components), strong positive and negative $u'v'$ correlations of the fluctuations are seen as the jet flows downstream and outward in both directions at the top of the jet. In the flow region near the wall, especially close the ejection hole, the v -component has changed directions as the flow entrains below the jet core and thus the correlations change sign.

The correlations dissipate moving further downstream as the flow become better mixed and more uniform and random. The correlations for $BR = 2.4$ are higher in magnitude relative to $BR = 1.2$.

Turbulent Heat Flux

The normalized turbulent heat flux $u'T'$ is shown in Figure 20. Both probes show similar results, a positive correlation of u -velocity and temperature fluctuations with the highest values near the top of the jet. The regions with the largest temperature fluctuations correlate with the high velocity fluctuations. The highest areas of temperature and velocity correlated mixing are, as expected, near the jet freestream interfaces and the flow entrainment areas.

The agreement between the two probes was fairly good, especially considering the probe volumes and measurement filtering can affect the temporal and spatial resolution. The more vertical flow areas near the outer edges of the jet are better described by Probe 2, while the more spanwise flow areas near the top of the jet are better described by Probe 1. As the flow continues downstream, these differences diminish as the jet becomes more diffuse. The asymmetry seen in Probe 2 is likely due to survey data point resolution as well as the bias in the vertical flow seen by each of the velocity wires of the probe. The asymmetry from Probe 2 for $BR = 1.2$ was investigated in Borghi (Ref. 11), in which a two-point heat flux study was conducted comparing experimental results with Large Eddy Simulation results. It was found that by offsetting the temperature and velocity measurements in the spanwise direction to accommodate the wire spacing of the probe and down sampling the LES to match the spatial resolution of the experiment, the LES results matched the experiment. See Appendix D for further discussion on this comparison. For $BR = 2.4$, the differences in the probes are much less pronounced.

The turbulent heat flux parameters $v'T'$ and $w'T'$ are shown in Figure 21. The magnitudes of the $v'T'$ and $w'T'$ correlations are smaller than those for $u'T'$. The direction of the $v'T'$ heat flux follows the velocity and thermal paths, flowing in the negative direction for positive y/D and flowing in the positive direction for negative y/D and then swirling back around and under. Similarly, $w'T'$ shows high positive correlation where the vertical flow is upward and mixes with the lower temperature main flow. Regions of negative $w'T'$ correlation are in the outer and lower regions where the vertical flow is downward and entraining the lower temperature main flow.

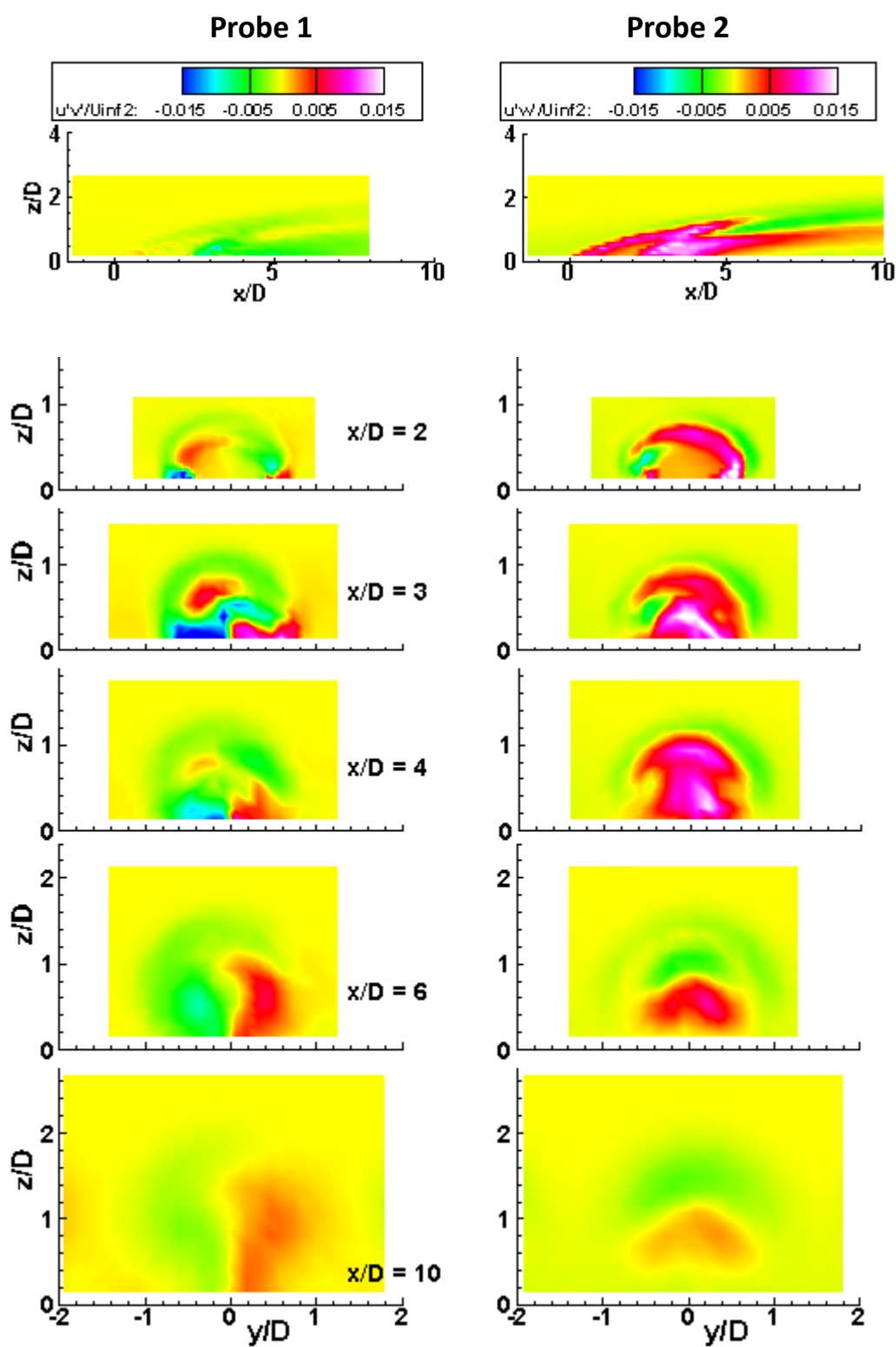


Figure 19.—(a) Reynolds stress parameters $u'v$ and $u'w$ for Probe 1 and Probe 2 at streamwise and spanwise survey planes, $BR = 1.2$.

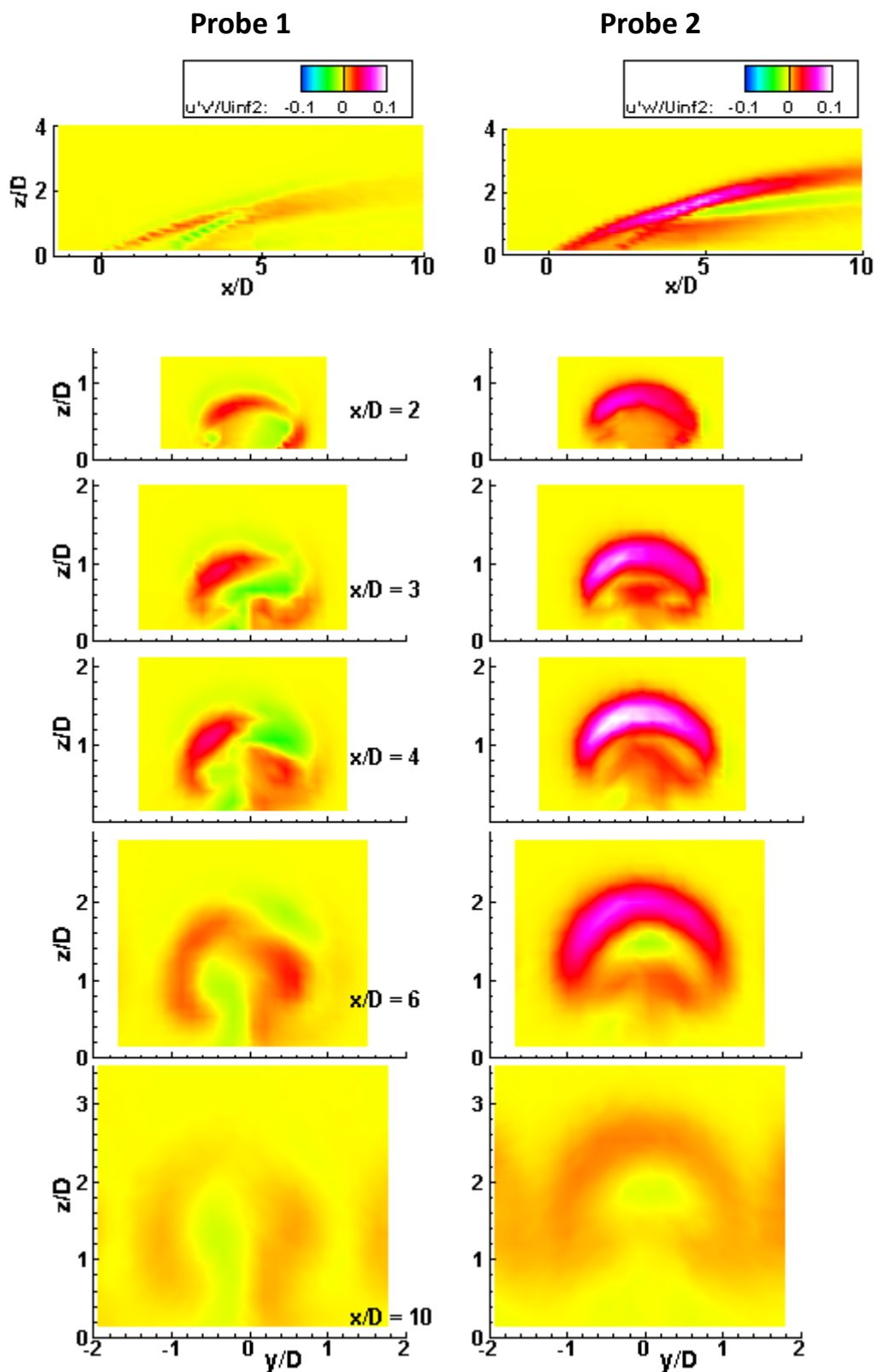


Figure 19.—(b) Reynolds stress parameters $u'v$ and $u'w$ for Probe 1 and Probe 2 at streamwise and spanwise survey planes, $BR = 2.4$.

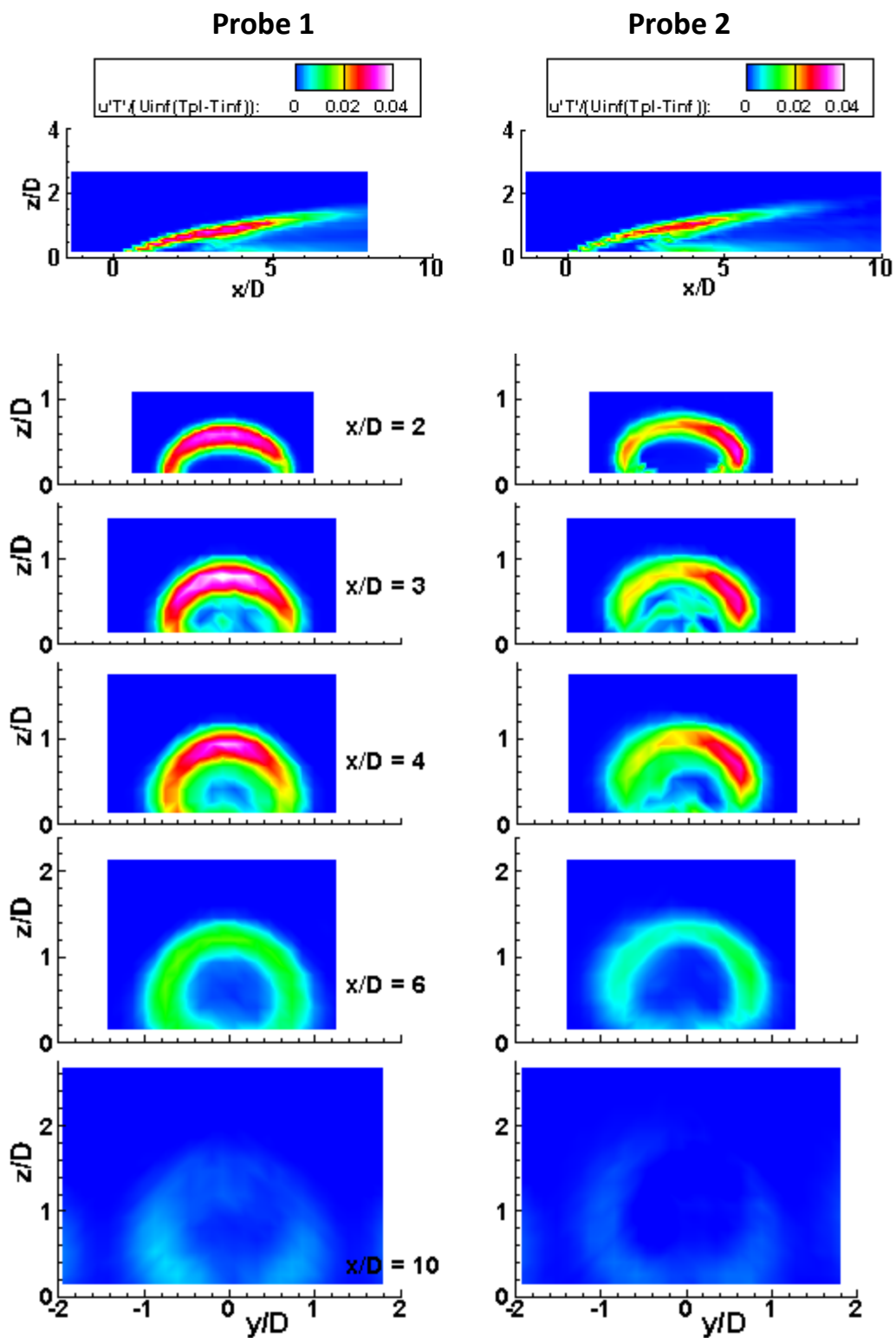


Figure 20.—(a) Normalized heat flux component $u'T'$ for Probe 1 and Probe 2 at streamwise and spanwise survey planes, $BR = 1.2$.

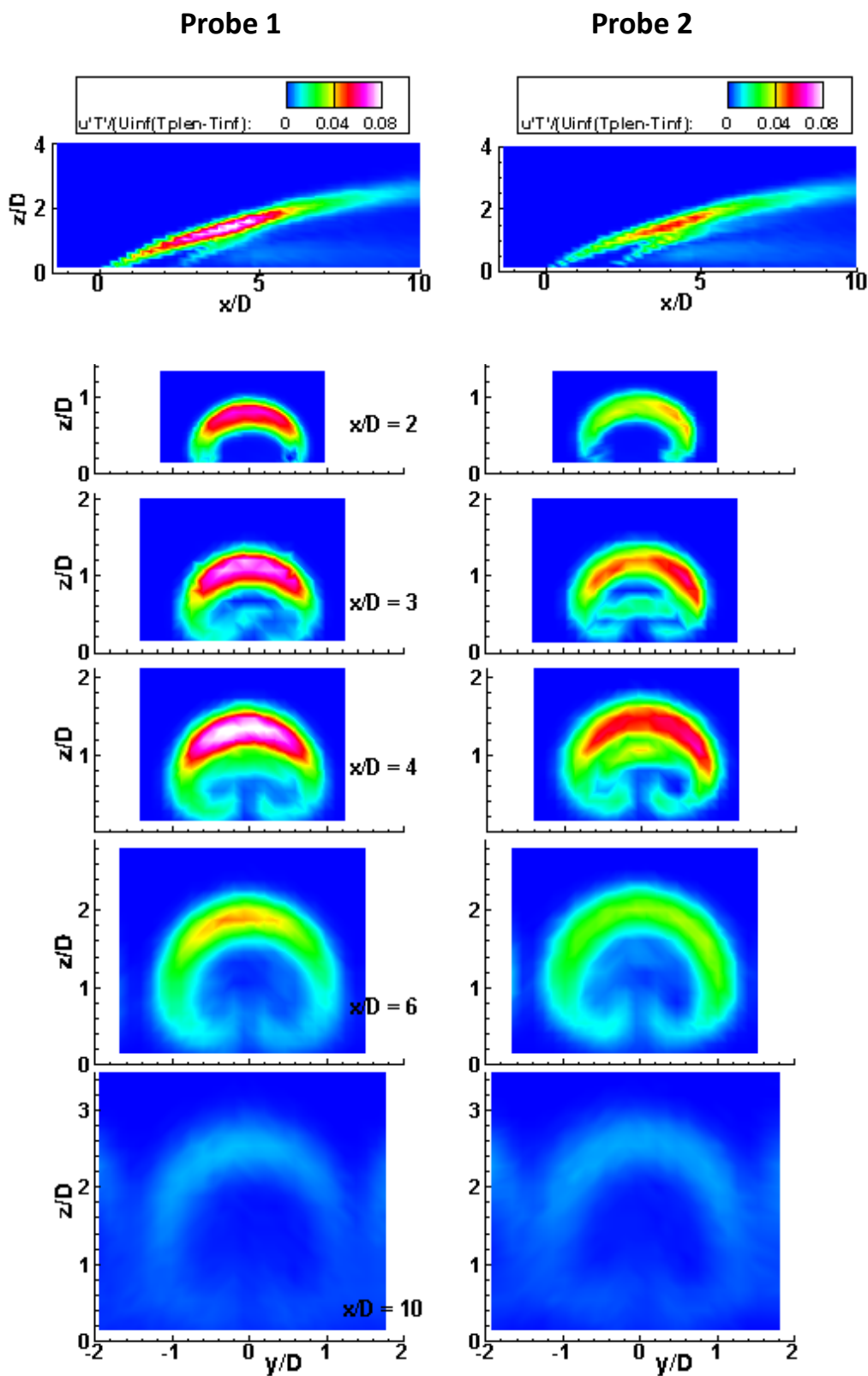


Figure 20.—(b) Normalized heat flux component $u'T'$ for Probe 1 and Probe 2 at streamwise and spanwise survey planes, $BR = 2.4$.

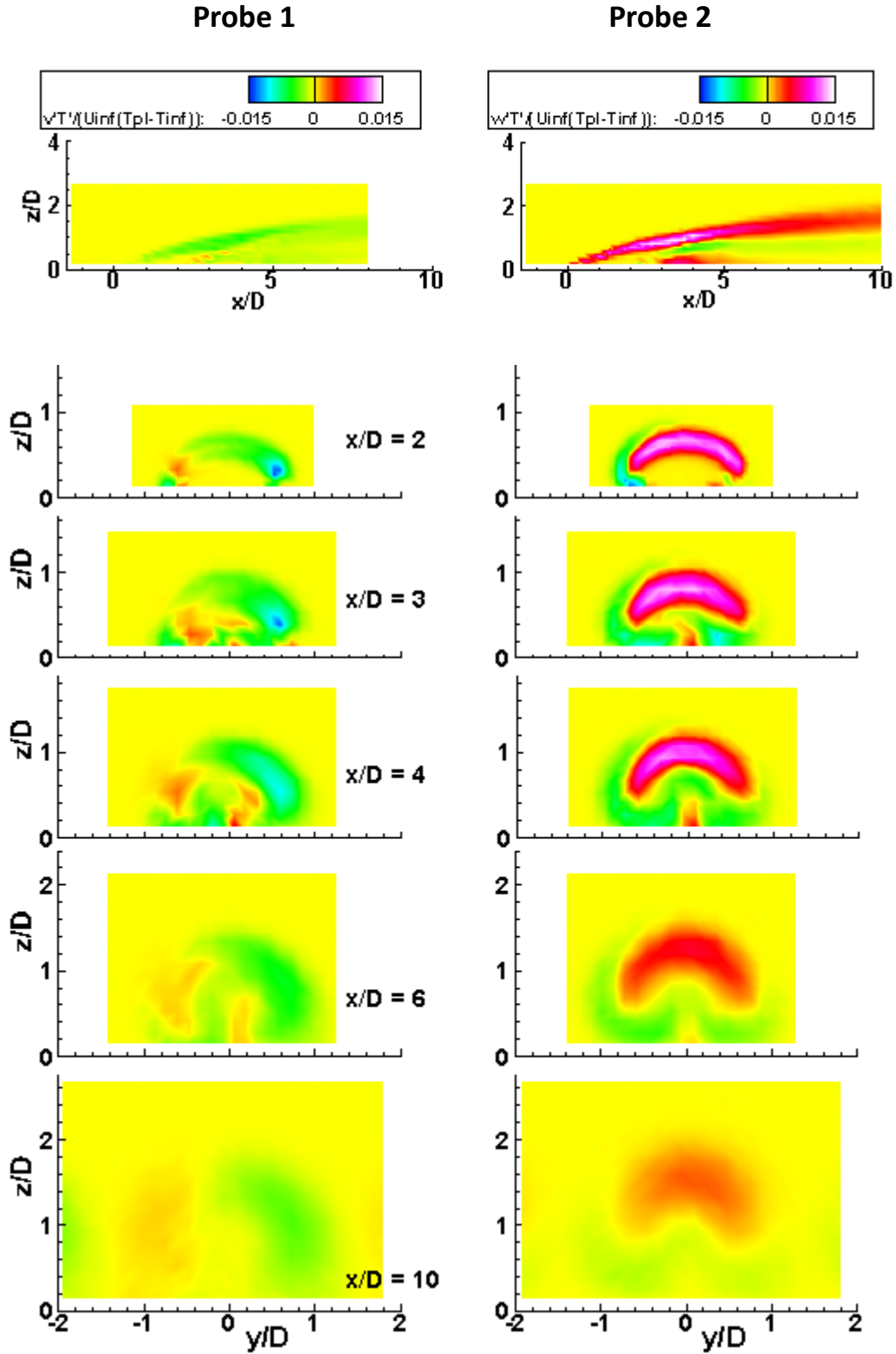


Figure 21.—(a) Normalized heat flux components $v'T'$ and $w'T'$ for Probe 1 and Probe 2 at streamwise and spanwise survey planes, $BR = 1.2$.

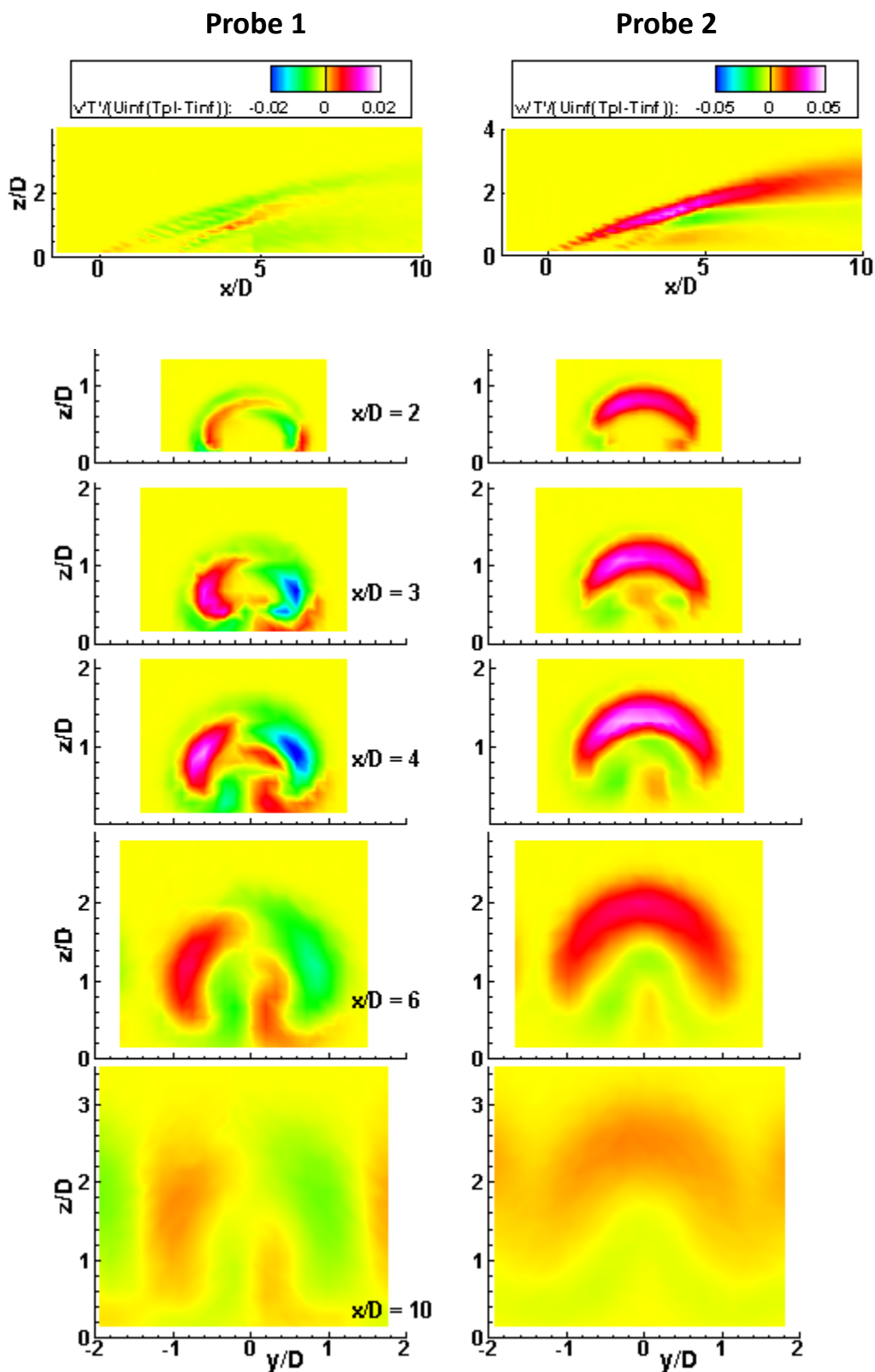


Figure 21.—(b) Normalized heat flux components $v'T'$ and $w'T'$ for Probe 1 and Probe 2 at streamwise and spanwise survey planes, $BR = 2.4$

Conclusion

An extensive data set of experimental measurements have been provided on a large-scale film cooling jet model for two blowing ratios. Surface heat transfer and film cooling effectiveness measurements were acquired using infrared thermography. Mean and fluctuating velocity and temperature measurements as well as statistical quantities such as Reynolds stress, turbulence, length scale, and turbulent heat flux were acquired from simultaneous temperature/velocity measurements using two different “xT” probes with constant temperature and constant current anemometry. Turbulent heat flux measurements are typically difficult to acquire, so the data provided in this paper will prove useful for validating computational models. While the temperature values were similar between the two probes used, there were differences in velocity values due to the orientation of the wires and the resulting probe volume. Spanwise flows were better represented by spanwise-streamwise wires of Probe 1, and vertical flows were better represented by the vertical-streamwise wires of Probe 2. Comparisons of data with computational analysis and other measurements are noted in the Appendixes. Data from this study is available on the NASA Open Data Portal at <https://data.nasa.gov/Aerospace/Film-Cooling-Data/tjbu-3afk>.

Appendix A.—Cooled Versus Heated Secondary Flow Comparison

Data was taken in the SW-6 facility using either a cooled secondary flow or a heated secondary flow. The cooled flow was obtained by routing the secondary flow through copper tubing that was coiled inside an ice water tank shown in Figure A.1 (Ref. 12), resulting in a temperature ranging from 35 to 45 °F. The heated flow option was achieved by routing the secondary flow through three parallel in-line electric pipe heaters as shown in Figure A.2, resulting in temperatures of 140 to 150 °F. The lift off of the injection flow depends on density which is a function of the temperature of the injected air for a given blowing ratio. Since heated air has lower density, a hot injection flow may have more lift off from the surface and higher velocity than if cooled injected air was used. A comparison of results between cooled and heated injection air showed no significant differences for the present study; buoyancy effects were thus considered small with relatively small temperature differences near room temperature. Figure A.3 shows a typical comparison of the cooled and heated secondary flow temperature data; the nondimensional temperature data match fairly well. This work is a case study for validation of computational codes and since the heated flow allowed a larger temperature difference from the freestream room temperature of nominally 70 °F, it was the preferred setup for the current experiments.

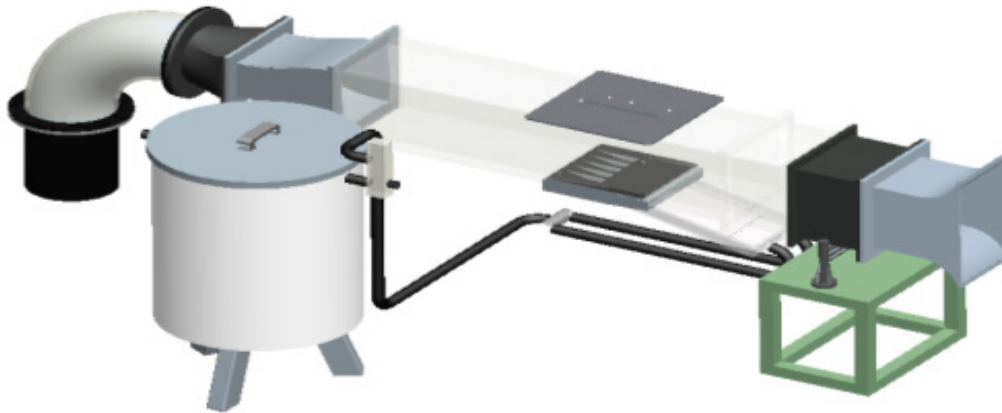


Figure A.1.—Typical tunnel layout with secondary flow ice bath.

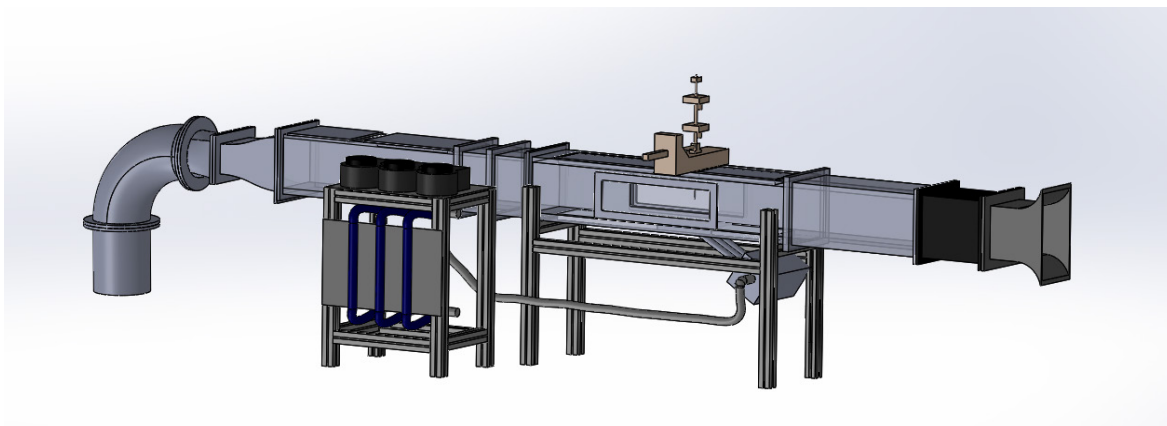


Figure A.2.—Typical tunnel layout with secondary flow electric heaters.

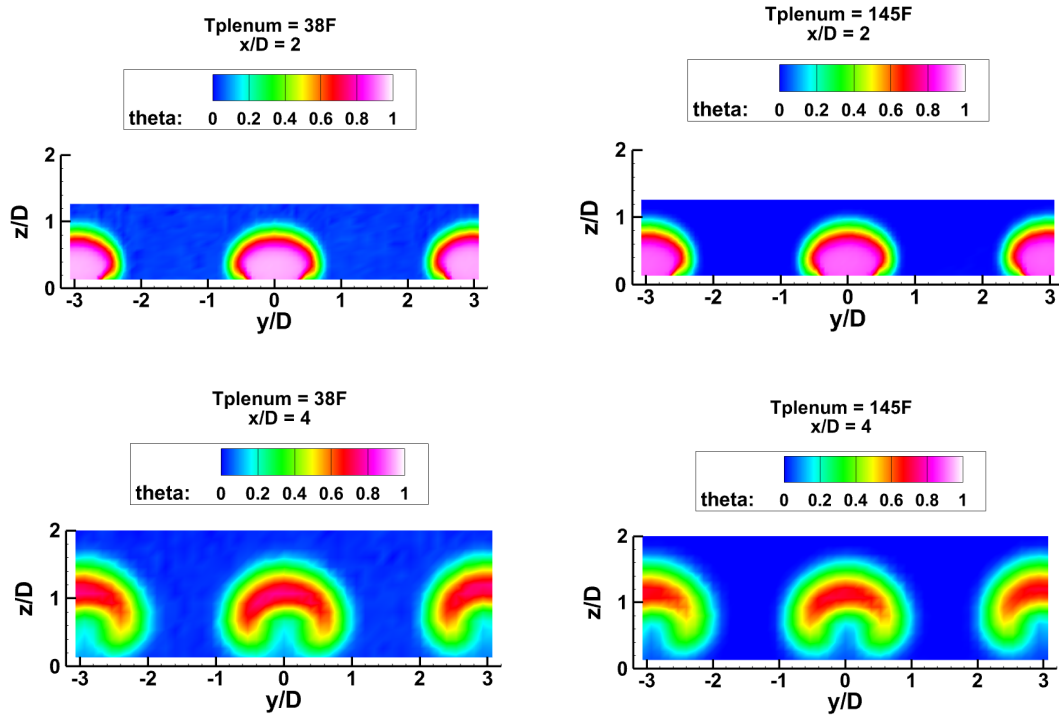


Figure A.3.—Comparison of single-wire temperature survey data with cooled ($T_{\text{plenum}} = 38^\circ\text{F}$) versus heated ($T_{\text{plenum}} = 145^\circ\text{F}$) secondary flow, $BR = 2.4$.

Appendix B.—Choice of Variables and Variable Definitions

The data measured in this study can be represented in many ways. Most of the variables presented are normalized by some factor. Many of the normalizing factors were straightforward but some were not obvious. The choice of the denominator could be used to highlight certain aspects of the results, especially with respect to the fluctuating data.

Local velocity components were normalized by the freestream approach velocity, U_∞ (nominally 30 ft/sec): u/U_∞ , v/U_∞ , w/U_∞ . The local fluctuating velocities were also normalized by freestream velocity: u'/U_∞ , v'/U_∞ , w'/U_∞ . Since the free stream velocity is a low-fluctuating mostly one-dimensional variable in the streamwise direction, it is relatively insensitive to probe orientation effects and thus is a very accurate measurement. Note that these fluctuation quantities are not normalized by the local velocity, thus they are not strictly speaking local turbulence intensities, which are defined as the root sum square of component fluctuations divided by the *local* mean resultant velocity. Figure B.1 shows component comparisons of “local velocity fluctuations” and “local turbulence intensity” (in decimal form rather than percentage as in Figure 16) along the centerline. Note that along the streamwise centerline, the flow is symmetrical in the spanwise direction (v -velocity component), thus Probe 2 (which measures u - and w -velocity components) provides a more accurate measurement of the total turbulence intensity for the centerline. At most other locations the flow is highly three-dimensional and thus neither probe can accurately nor simultaneously capture all three resultant velocity components. Normalizing by the tunnel approach freestream velocity provides a more consistent reference and highlights the fluctuations better, but caution should be used to not confuse it with turbulence intensities for modeling purposes, especially at higher blowing ratios. For example, the u'/U_∞ plot for $BR = 2.4$ shows fairly high fluctuations in the jet region, but the Tu plot illustrates that the high turbulence is mostly in the mixing region of the shear layers between the jet and mainstream flow, with the freestream and the jet core directly out of the hole having relatively low turbulence.

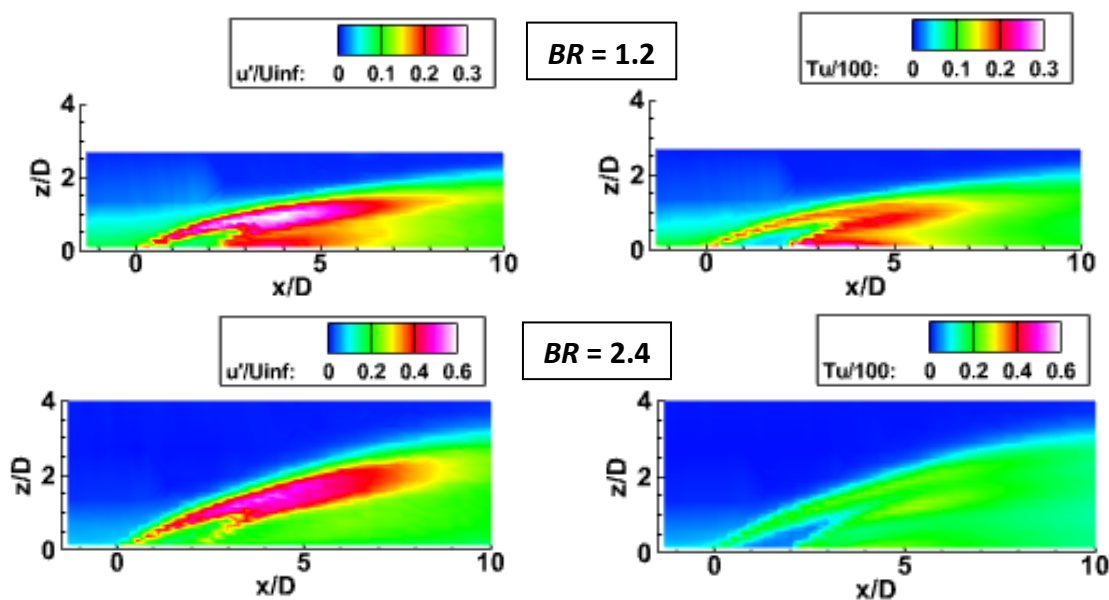


Figure B.1.—Comparison of normalized local streamwise velocity fluctuation values to local turbulence intensity values ($Tu/100$), $BR = 1.2$ and $BR = 2.4$.

The mean temperature measurements were presented as the dimensionless variable θ defined as:

$$\theta = \frac{(T - T_{\infty})}{(T_{plenum} - T_{\infty})} \quad (B.1)$$

The fluctuating temperatures were normalized by the thermal driving temperature difference between the approach tunnel freestream and the plenum.

$$\frac{T'}{(T_{plenum} - T_{\infty})} \quad (B.2)$$

This was chosen because the temperature fluctuations are generally caused by the mixing of the jet from the plenum as it protrudes into the mainstream flow airstream. Using this overall temperature driving force also agrees well with using the approach tunnel velocity to normalize velocity fluctuations.

The heat flux variables were normalized by the parameter $U_{\infty}(T_{plenum} - T_{\infty})$. Thus, the plotted variables are:

$$\frac{u'T'}{U_{\infty}(T_{plenum} - T_{\infty})} \quad (B.3)$$

$$\frac{v'T'}{U_{\infty}(T_{plenum} - T_{\infty})} \quad (B.4)$$

$$\frac{w'T'}{U_{\infty}(T_{plenum} - T_{\infty})} \quad (B.5)$$

The definition for the integral length scale, Λ_x (macroscale), was defined as

$$\Lambda_x = \left[\frac{E(f)U_{mean}}{4u'^2} \right]_{f \rightarrow 0} \quad (B.6)$$

E	energy
f	frequency
u'	standard deviation of the u -component of velocity

The dissipative length scale, λ_x (microscale), was defined as

$$\frac{1}{\lambda_x^2} = \frac{2\pi^2}{U^2 u'^2} \int_0^{\infty} f^2 E(f) df \quad (B.7)$$

The blowing ratio was defined by:

$$BR = \frac{(\rho U)_{injection}}{(\rho U)_{\infty}} \quad (B.8)$$

where ρ is the density of fluid.

The film effectiveness was defined as:

$$\eta = \frac{(T_{\infty} - T_{IRsurface})}{(T_{\infty} - T_{plenum})} \quad (B.9)$$

Appendix C.—Probe 1 and Probe 2 Comparison

Figure C.1 shows the two xT wire probes used in this study. Probe 1 measures temperature and the streamwise and spanwise velocity components, while Probe 2 measures temperature and the streamwise and vertical velocity components. The two cross wires of each probe are used to determine two velocity components and these wires are spaced 0.1 in. apart. The temperature wire is offset 0.1 in. Thus, the probe volume for Probe 1 is roughly 0.13D by 0.13D by 0.26D in the x, y, z directions and Probe 2 is 0.13D by 0.26D by 0.13D in the x, y, z directions.

Depending on the orientation of the probe wires, in some survey positions one of the velocity wires may be seeing a slightly different velocity than the other velocity wire. For example, at the top edge of the jet the lower wire will see more of the higher velocity jet core than the top wire. Similarly, at a survey position on the side of the jet core, the inside wire will see higher velocity than the outside wire. Additionally, the presence of one wire and its supports can slightly affect the vertical flow or cross flow that hits another wire; for example, the temperature wire and its supports can slightly influence the flow that the adjacent velocity wires will detect. These probe volume and orientation limitations lead to some asymmetry in the velocity data that is evident especially in the low blowing ratio data. These probe interferences may also be the cause of some of the fluctuation discrepancies between the probes. It should be noted that the measurement signals from these probes were very sensitive and special considerations were made to eliminate noise interference, maintain frequency response and spatial integrity to ensure low measurement uncertainty. It is felt that the raw data from these measurements is accurate and the artifacts are result of probe limitations and not measurement errors. The measurement uncertainties for the two probes were determined to be about 1 percent for temperatures and ranged from 1 to 6 percent for velocities.

In the presentation of results, where appropriate, the probe data was shifted to reflect more accurate location of the probe wire measurements. For example, temperature data was corrected to actual location of the temperature sensing wire—a vertical shift of 0.1 in. for Probe 1 and a horizontal shift of 0.1 in. for Probe 2. Similarly, the individual velocity measurements were shifted 0.05 in. to match the location of the center of the sensing wires of each probe. For cross correlation variables, e.g., $v'T'$, a correction was not possible, and thus more discrepancy and asymmetry are seen in the figures. For higher blowing ratio these effects are less noticeable.

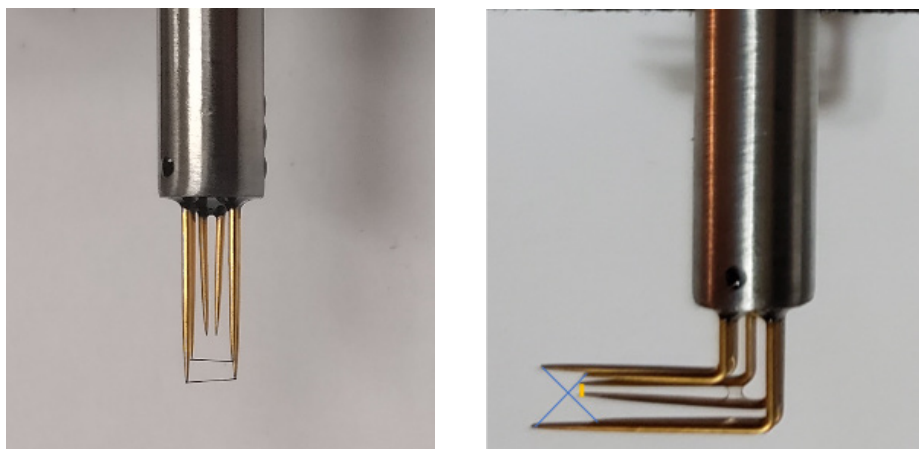


Figure C.1.—Close-up of the 3-wire “xT” probes showing cross-wire velocity wires and temperature wire; Probe 1 (left) and Probe 2 (right).

Figure C.2(a) and (b) show a comparison of temperature data taken from each of the two xT probes. As noted above, the temperature data was translated such that the location of the temperature sensing wires from the two independent surveys was coincident. Thus, the data for Probe 1 does not extend as low as Probe 2. The data is seen to be consistent between the two probes and is typical for an inclined jet in cross flow with the core flow transitioning from flattened circle to kidney shape. The slight differences in the spanwise data at $x/D = 2$ between $z/D = -0.5$ and 0.5 are due to the different probe volume and wire orientations mentioned above.

Figure C.3(a) and (b) show a comparison of the streamwise velocity data taken from each of the two xT probes. The data from the two probes agree fairly well showing the general kidney shaped development of the jet moving down stream. However, there are a few differences between the two probes especially for the lower blowing ratio, such as a slight asymmetry and some blurring of details near $y/D = \pm 0.6$. These small discrepancies are a result of the different wire configuration and probe volumes of each probe mentioned above. For example, the asymmetry of Probe 2 is the result of the flow hitting the right wire differently from the left wire. The vertical cross wires are 0.1 in. apart and one wire sees slightly higher velocity than the other wire as the probe traverses through the jet core and then a slightly lower velocity on the other edge of the jet core. This affects the resultant component calculations. For the higher blowing ratio, this difference is more negligible. The u -component from Probe 1 (streamwise and spanwise measurement) is thought to be more accurate on the sides of the jet ($z/D < -0.5$ and $z/D > 0.5$) where higher spanwise flows from entraining side vortices exist. Similarly, the center region of the jet ($-0.5 < z/D < 0.5$) which is dominated by the vertical velocity of the jet core is better represented by Probe 2 (streamwise and vertical measurement). See Appendix D for analysis supporting these conclusions.

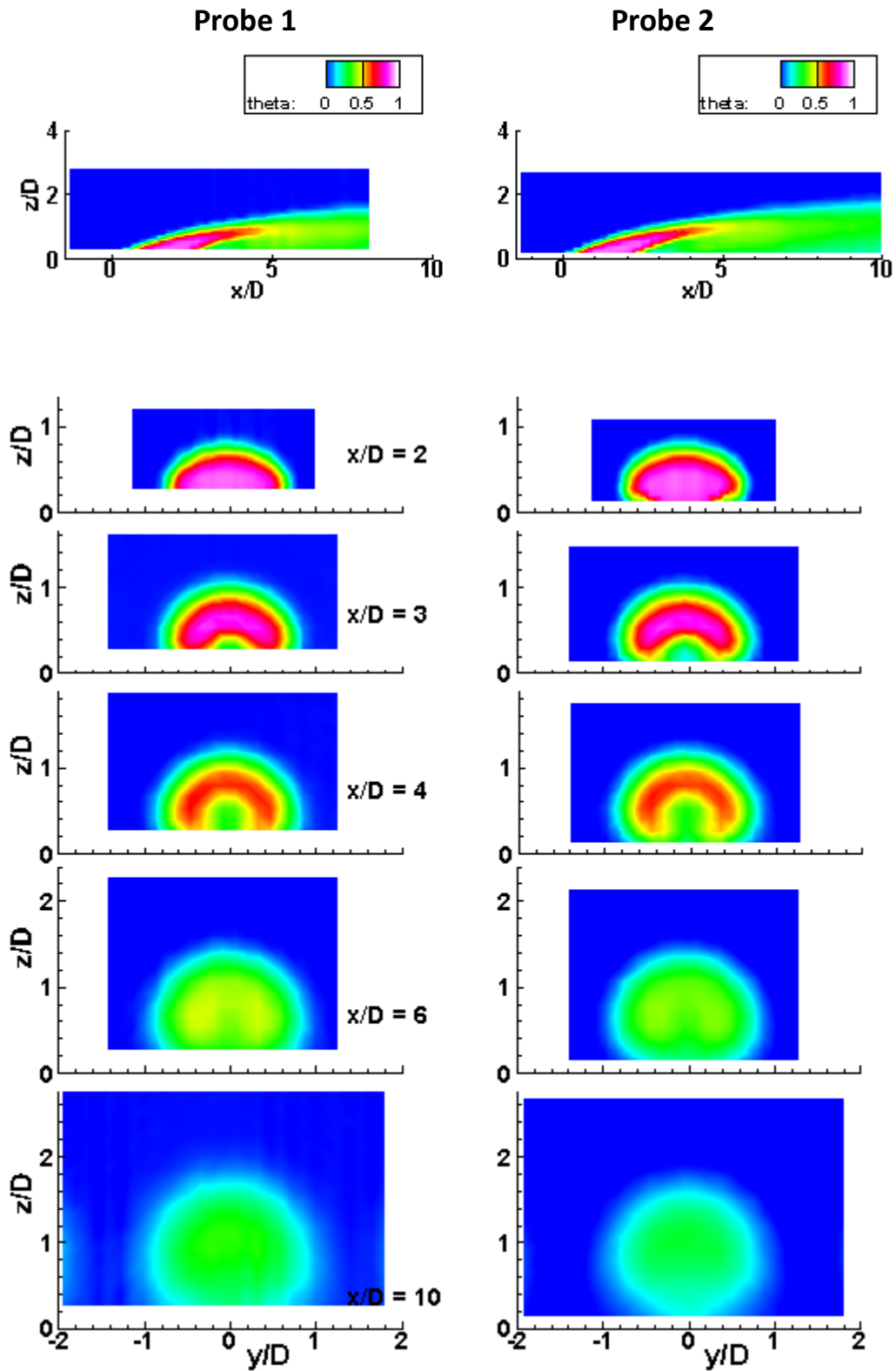


Figure C.2.—(a) Normalized temperature θ for Probe 1 and Probe 2 at streamwise and spanwise survey planes, $BR = 1.2$.

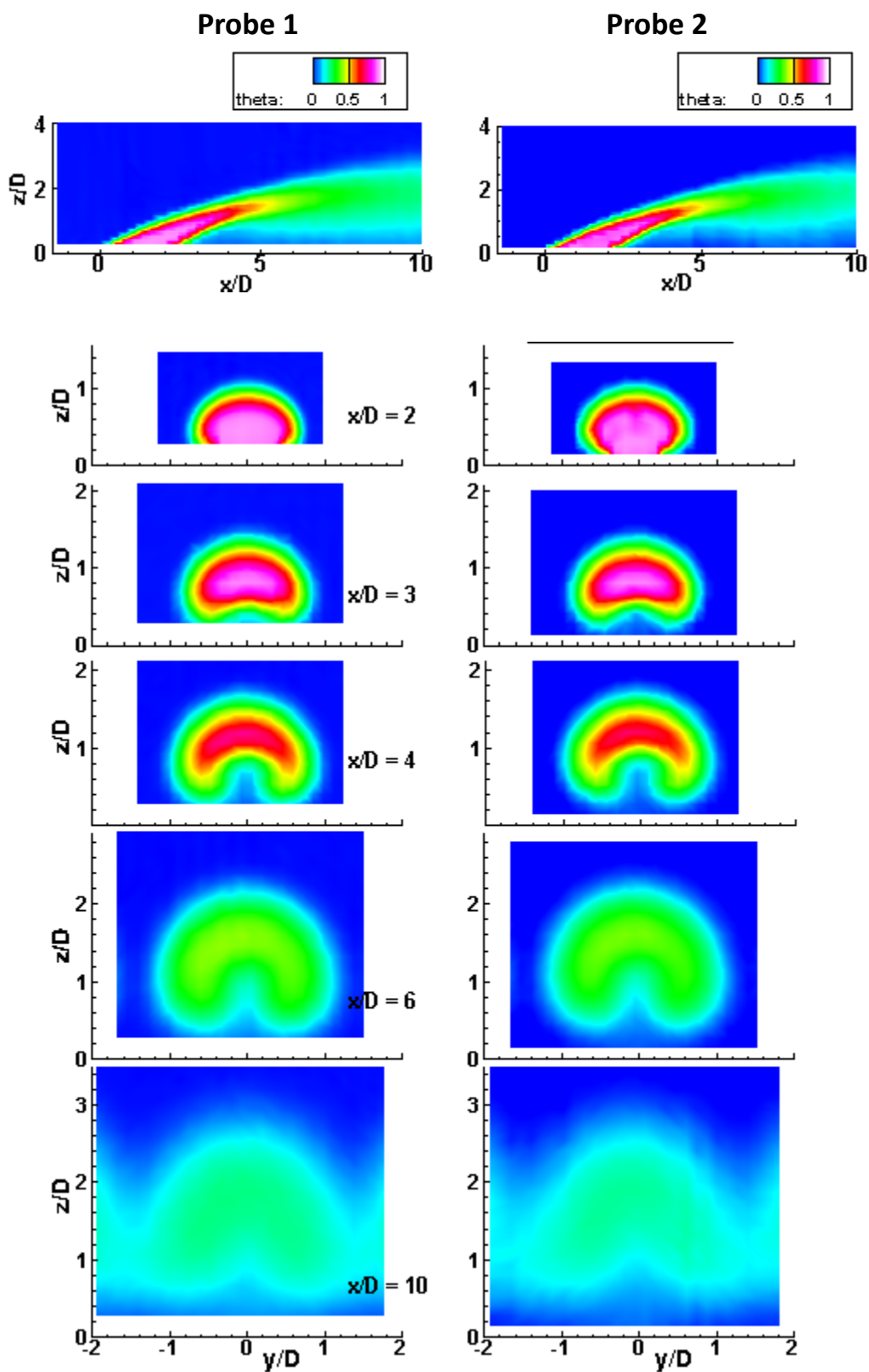


Figure C.2.—(b) Normalized temperature θ for Probe 1 and Probe 2 at streamwise and spanwise survey planes, $BR = 2.4$.

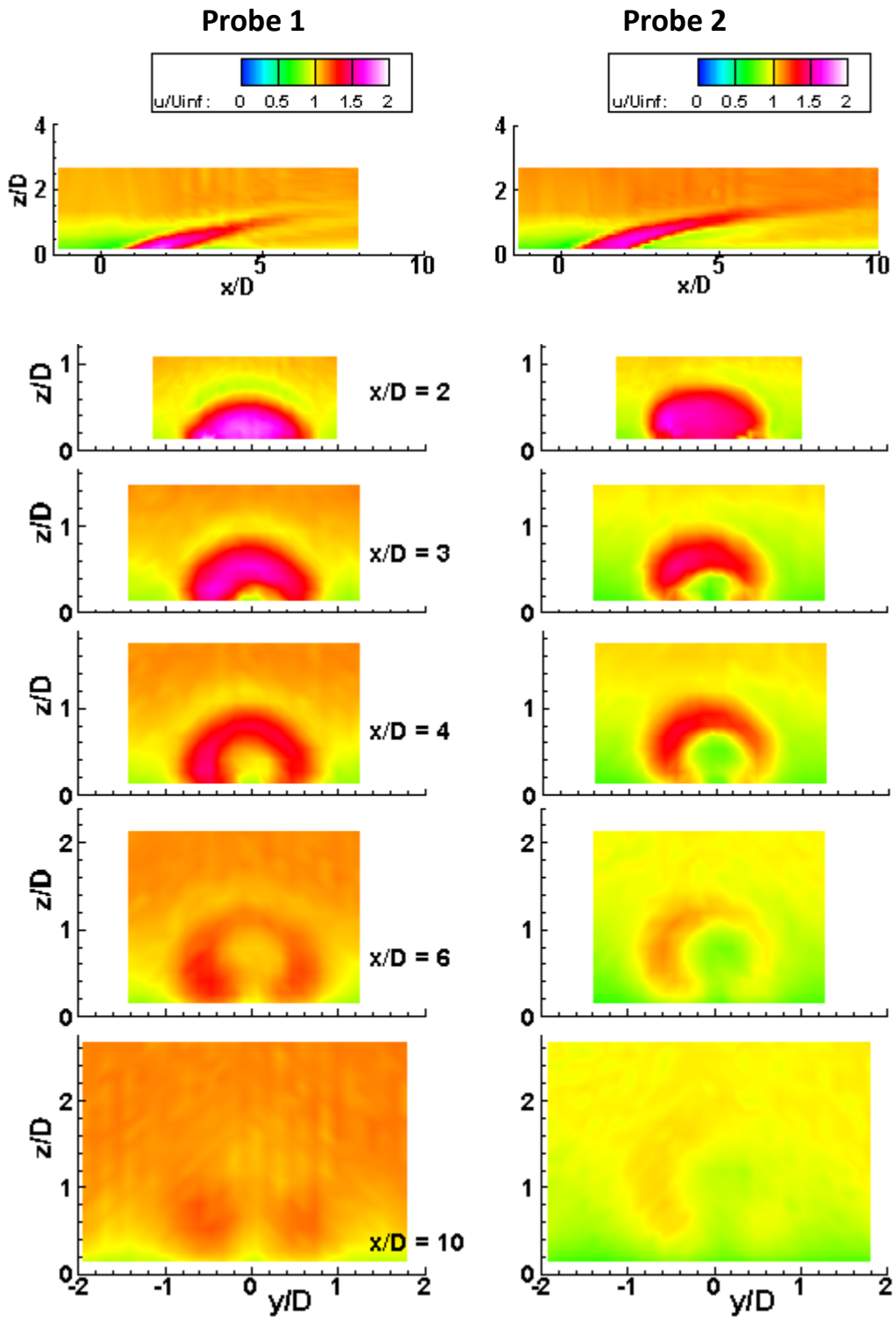


Figure C.3.—(a) Normalized u -component velocity for Probe 1 and Probe 2 at streamwise and spanwise survey planes, $BR = 1.2$.

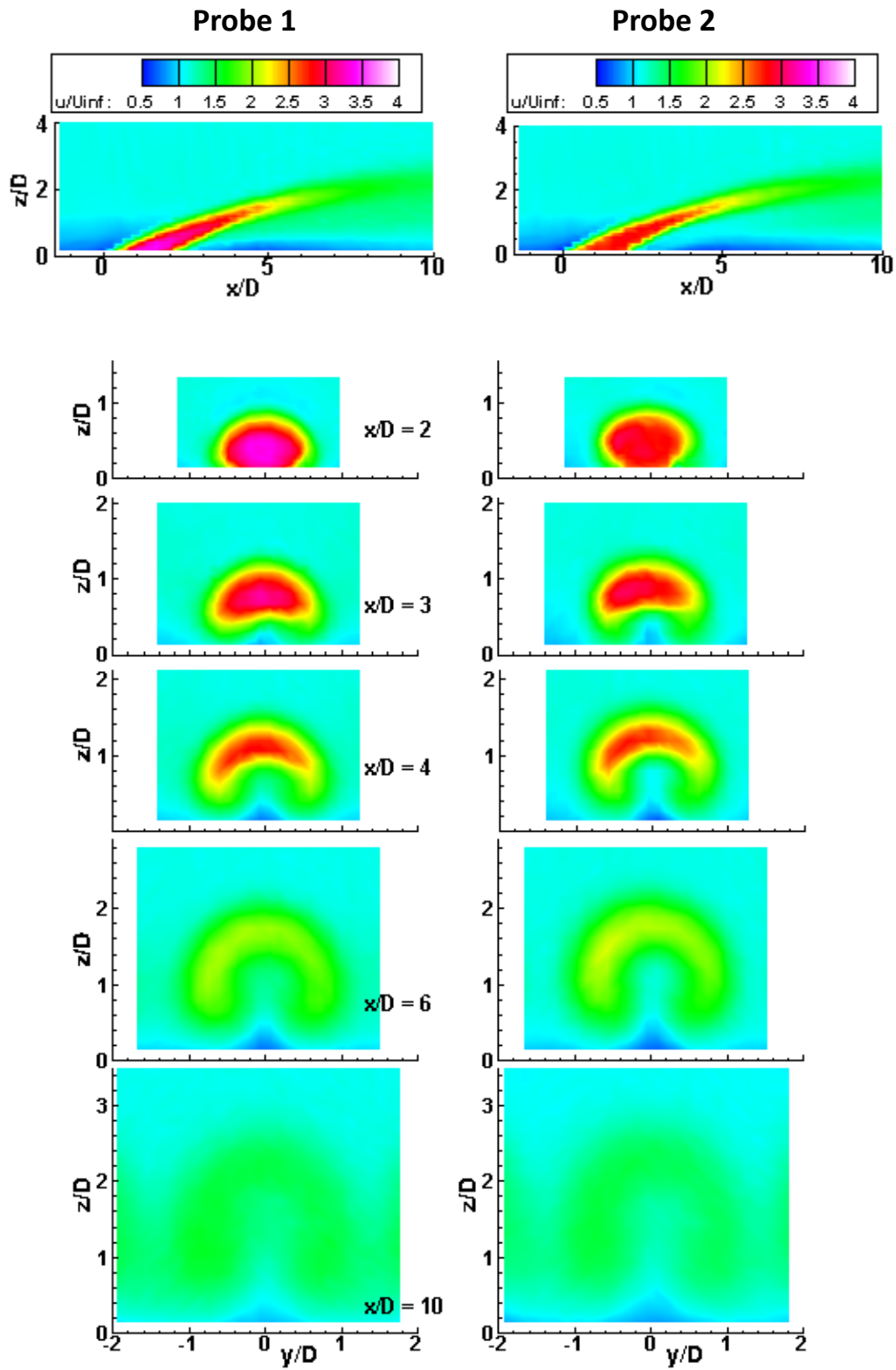


Figure C.3.—(b) Normalized u -component velocity for Probe 1 and Probe 2 at streamwise and spanwise survey planes, $BR = 2.4$.

Appendix D.—Comparison With LES Computations

The hot wire data was compared with a Large Eddy Simulation (LES) computation that was reported in Reference 11, with some of those results summarized below. Figure D.1 is taken from Reference 11 and shows the corresponding mean and fluctuating temperature profiles of both the hot wire experiment and the LES calculation for $BR = 1.2$. It should be noted that the coordinate system used in Reference 11 is different from the one used in this paper, thus the “Y/D” and “Z/D” axis labels are reversed. Generally, the data maps agree very well; the mean temperatures both show high core temperature with the jet mostly attached moving downstream. The LES calculations may show a slight separation just downstream of the hole, which is not evident in the hot wire data. Both LES and experiments show high temperature fluctuations in the shear layers, but the magnitude is higher in the upper shear layer of the LES calculation. Figure D.2 is also taken from Reference 11 and shows contours of the mean and fluctuating values of the streamwise velocity component. Again, the general shape of the contour maps agrees fairly well. In the centerline plane, there are small differences downstream of the jet near the floor, and there is some asymmetry in the mean velocity spanwise planes. The velocity fluctuation profiles show differences in the shear layers of the jet in the centerline plane, as well as in the spanwise planes near the hole.

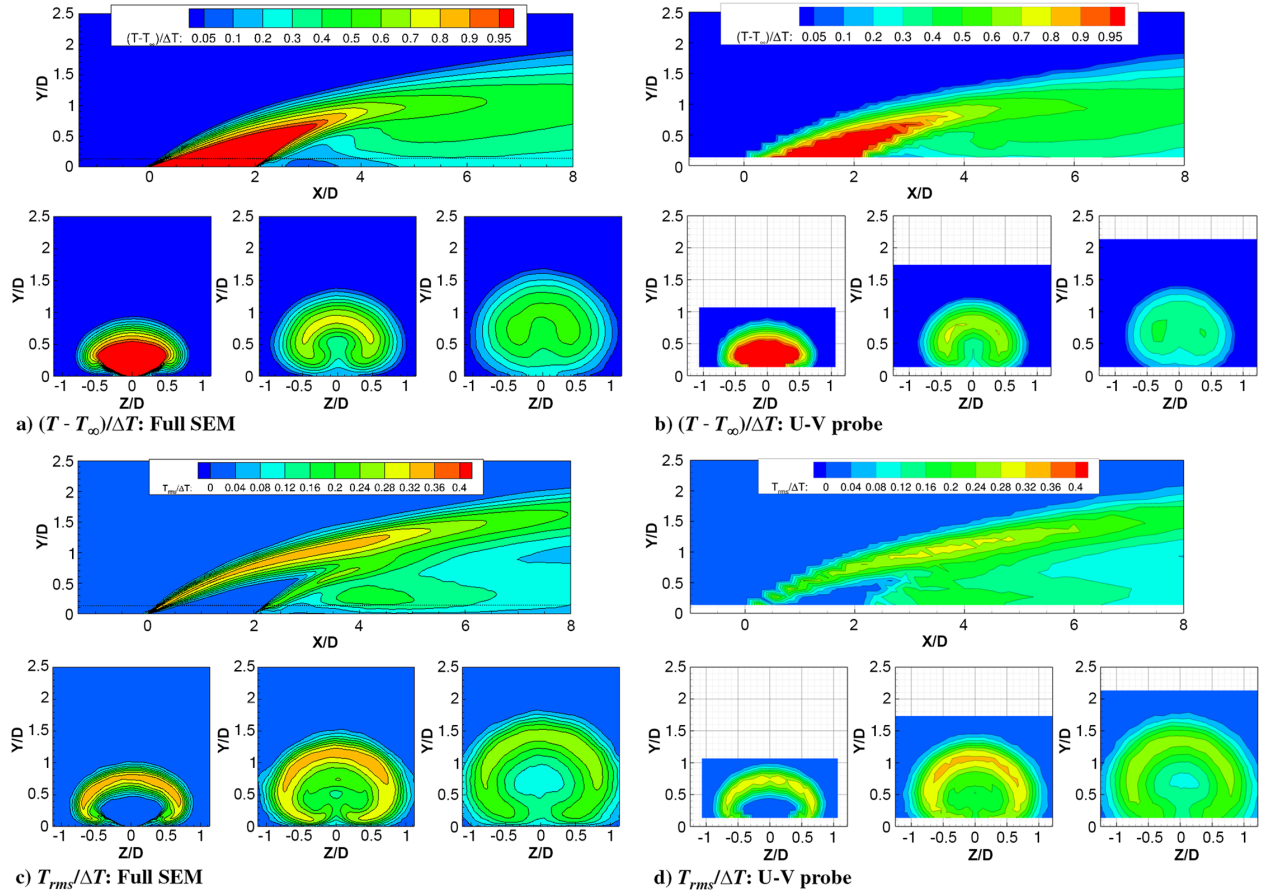


Figure D.1.—Mean (top) and fluctuating (bottom) temperature contours from LES (left) and xT-wire probe (right) along the centerline and at the spanwise planes $x/D = 2.00$, $x/D = 4.00$, $x/D = 6.00$, $BR = 1.2$ (from Borghi et al. (Ref. 11)).

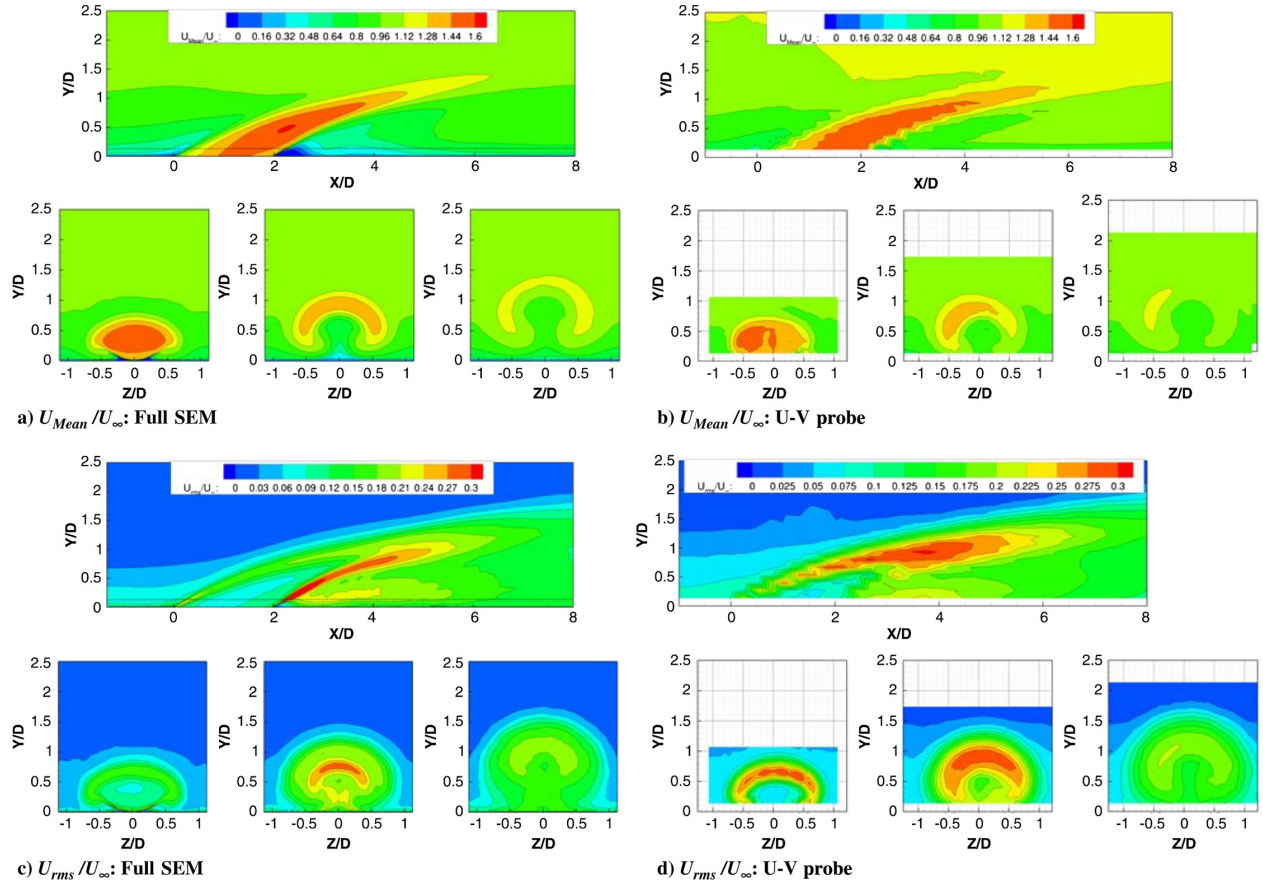


Figure D.2.—Mean (top) and fluctuating (bottom) streamwise-component velocity contours from LES (left) and xT-wire probe (right) along the centerline and at the spanwise planes $x/D = 2.00$, $x/D = 4.00$, $x/D = 6.00$, $BR = 1.2$ (from Borghi et al. (Ref. 11)).

Comparison of the heat flux variables is not as straight forward. Frequency and spatial limitations of any measured quantities can affect the ability to make direct comparisons with high grid resolution variables derived from CFD calculations. The hot wire probes in this study had specific probe volumes and frequency response limitations which had an effect on the measurements taken. These limitations in the data made direct comparison of the typical design variables difficult. Figure D.3 shows the streamwise heat flux $u'T'$ for the experiment and LES computation. Differences are evident, especially the upper and lower shear layers in the centerline and spanwise planes. The experimental heat flux plots display an asymmetry not seen in the LES simulations. The cause of this asymmetry is related to the spanwise offset of the temperature wires relative to the velocity wires in Probe 2 used here. By defining specific variables from the CFD data to match the limitations in the measured quantities, a better comparison can be made. To match the experimental measurements, the computational LES heat flux was modified in several ways. Figure D.4 shows the result of this modification to the LES data of $u'T'$ at $x/D = 3$. In the top left of the figure, the full resolution streamwise heat flux from the LES simulation is presented; in the bottom left the experimental result is shown. In the top right, the spatially down sampled LES heat flux is provided in which the spatial resolution of the LES heat flux matches the single point probe locations of the experiment. Recall that in the hot wire probes, the velocity wires and the temperature wires are offset by approximately $0.1D$. The bottom right plot in Figure D.4 shows the modified computational data that includes both the offset and down sampling to the experimental resolution. The inclusion of the temperature wire offset dramatically changes the distribution of the heat flux, with asymmetry in the

upper shear layer being well reproduced, and a reduced lower shear layer that now better matches the experiment. Thus, inclusion of the measurement limitations (offset and resolution) into the CFD results allows a better comparison of the data sets. This verifies agreement between the experimental results and the CFD calculations, thus yielding confidence in the full CFD derived “design” variables. This seems to be a viable way to match CFD results to measured variables within the limitations of the measurement capabilities and is preferred to other techniques that are designed to “add resolution” to experimental data.

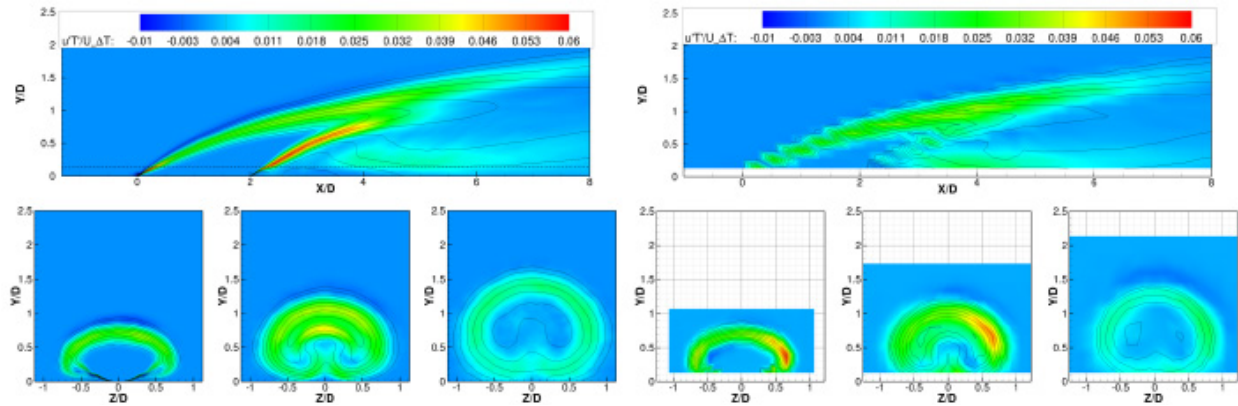


Figure D.3.—Streamwise turbulent heat flux from LES (left) and xT-wire probe (right) along the centerline and at the spanwise planes $x/D = 2.00$, $x/D = 4.00$, $x/D = 6.00$, $BR = 1.2$ (from Borghi et al. (Ref. 11)).

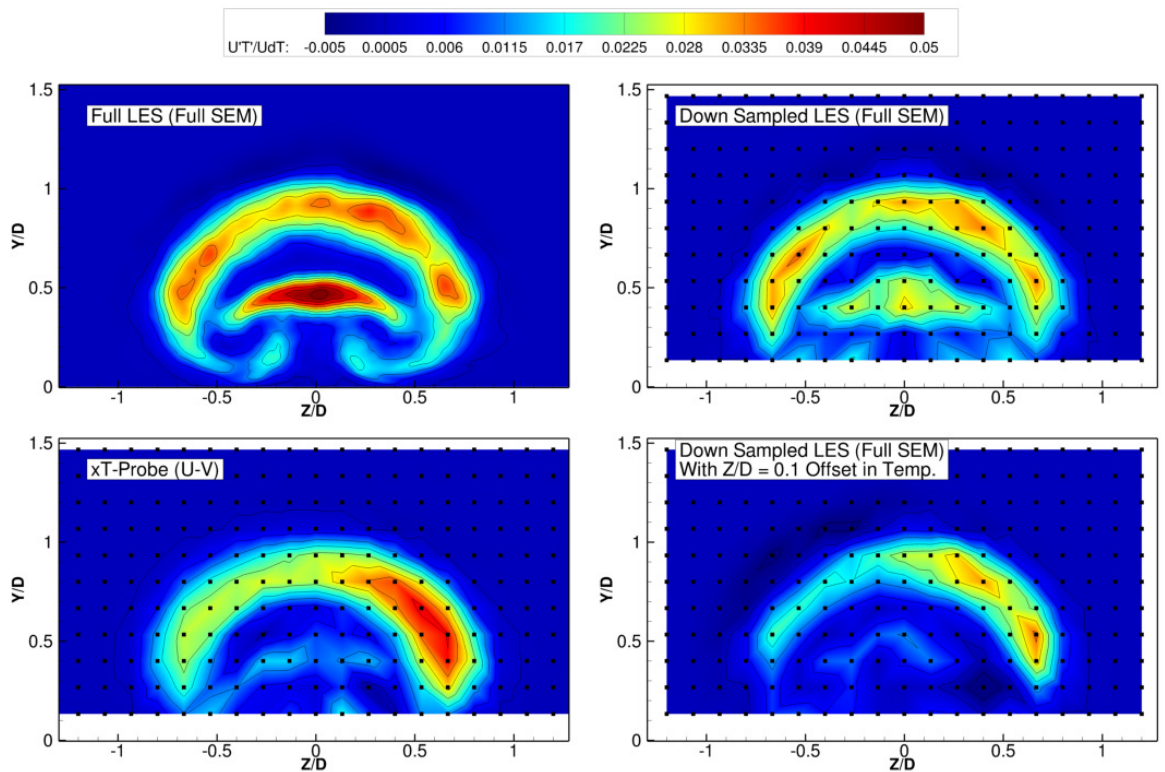


Figure D.4.—Results of two-point heat flux study. Streamwise heat-fluxes at $x/D = 3.0$. Full resolution LES (top left), xT Probe 2 (bottom left), Down sampled LES (top right), Down sampled LES with spanwise temperature offset (bottom right) (from Borghi et al. (Ref. 11)).

Appendix E.—Comparison With PIV Data

A comparison was made between the hot wire data taken in the present study with particle image velocity data with the same film cooling test model in the same facility at similar test conditions. Details of the measurement can be found in Reference 1.

Figure E.1 and Figure E.2 show the mean velocity components, u/U_∞ , v/U_∞ , w/U_∞ , from hot wire data and PIV data at blowing ratios of 1.2 and 2.4, respectively. The centerline contours for the velocity components generally show fairly good agreement especially for the higher blowing ratio case. Due to symmetry along the streamwise centerline, the v -component is quite small and thus discrepancies in the figures are rather negligible. Compared to the hot wire data, the PIV data does not pick up the higher velocities under the jet. The u -velocity contours in the spanwise planes again show fairly good agreement, but some discrepancies are evident at the lower blowing ratio case; the hot wire data shows some asymmetry in the jet profiles due to aforementioned probe wire orientation. Note that the uncertainties are larger for the lower velocity data.

While the mean values of the hot wire and PIV data compare well, a comparison of the fluctuating values shows some discrepancies. Figure E.3 and Figure E.4 show the fluctuating component velocities, u'/U_∞ , v'/U_∞ , w'/U_∞ from hot wire and PIV measurements for both blowing ratios. The general patterns of fluctuations are similar for both data sets, but the hot wire shows fluctuation magnitudes up to 25 percent higher at the $x/D = 6$ spanwise location for the u -component and $BR = 1.2$. Additionally, in the PIV u -component data, the upper and lower shear layers opposite the jet core appear to extend separately further downstream than the hot wire data illustrates. The hot wire data does not have enough resolution to pick up this subtlety.

It should be noted that there are distinct differences in the methods and limitations between hot wire and PIV measurements. While PIV measurements may have higher spatial resolution, the statistical quantities are determined by ensemble averaging over specified subregions, whereas hot wires are true single point simultaneous and continuous measurements. The PIV statistical quantities are dependent on the size of the subregion used. This could account for the better spatial resolution, but lower turbulence values observed in the PIV data.

Comparison of the Reynolds stress $u'v'$ in Figure E.5 and Figure E.6 shows generally good agreement with trends, but magnitudes vary somewhat. The centerline planes don't always agree, since a slight shift in the spanwise direction can change the contours for that plane. The Reynolds stress $u'w'$ results do not compare as well, especially at the lower blowing ratio. This is likely due to the difference in measurement calculation techniques as well as the relatively larger spatial resolution of the hot wire data.

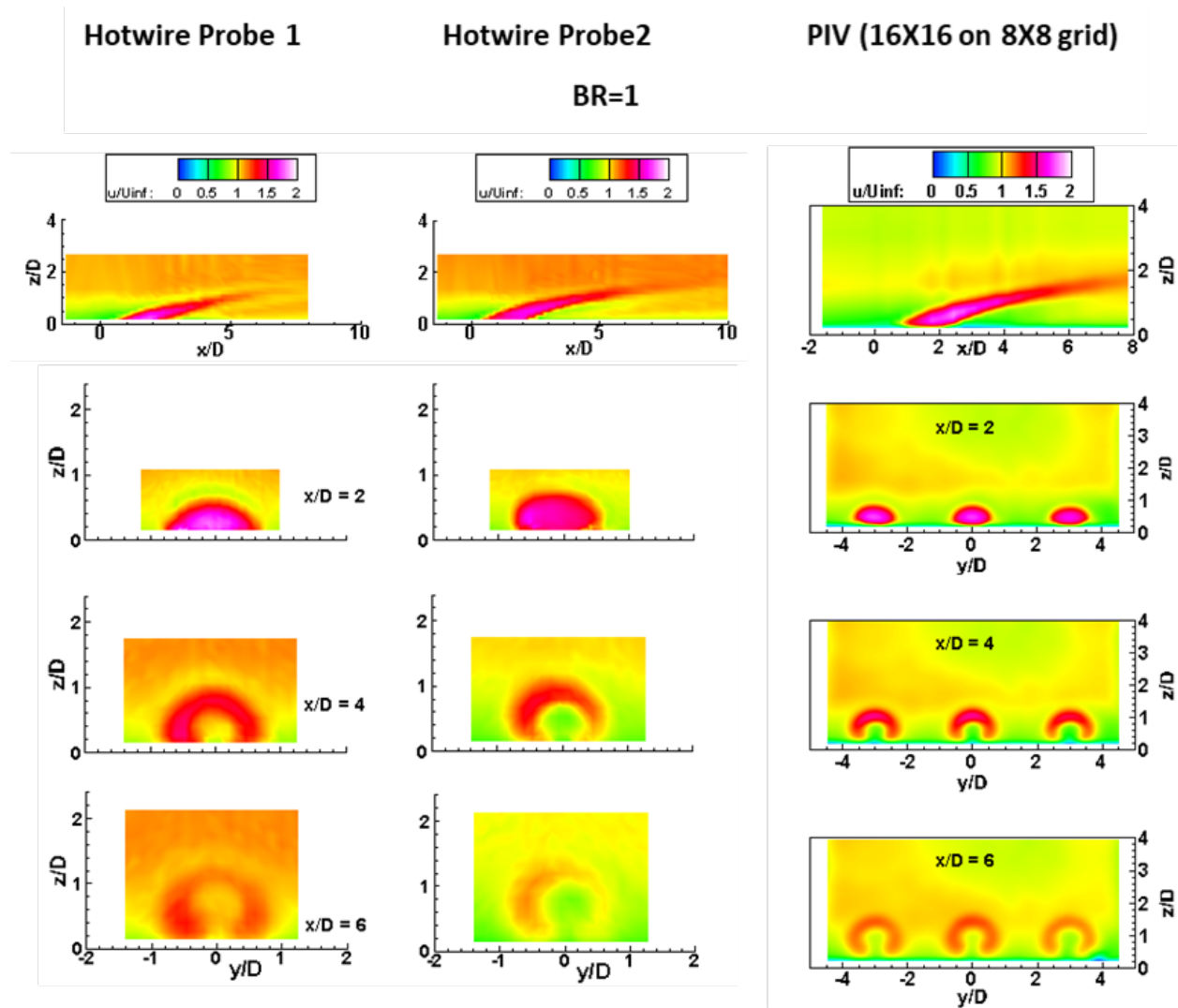


Figure E.1.—(a) u -component velocity, $BR = 1.2$, HW Probes 1 and 2 and PIV.

Hotwire Probe 1

PIV (16X16 on 8X8 grid)

BR=1

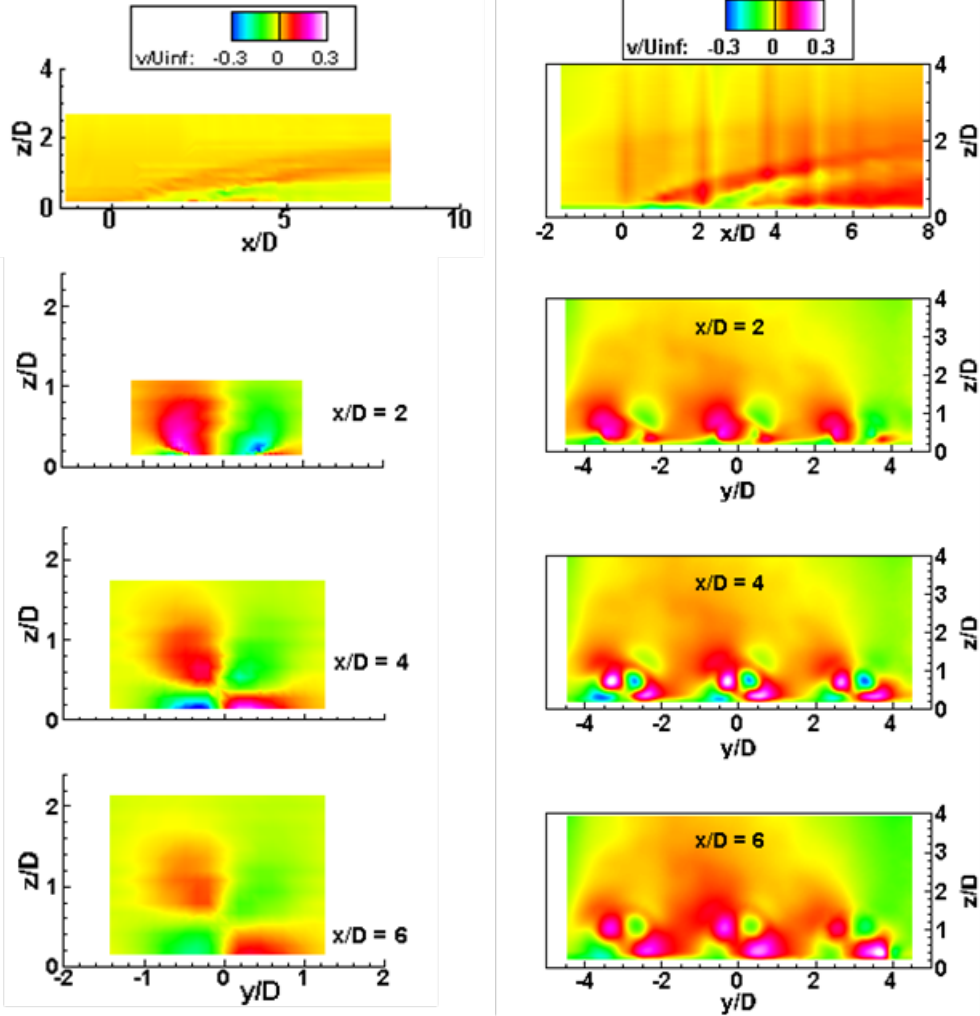


Figure E.1.—(b) v -component velocity, $BR = 1.2$, HW Probes 1 and 2 and PIV.

Hotwire Probe 2

PIV (16X16 on 8X8 grid)

BR=1

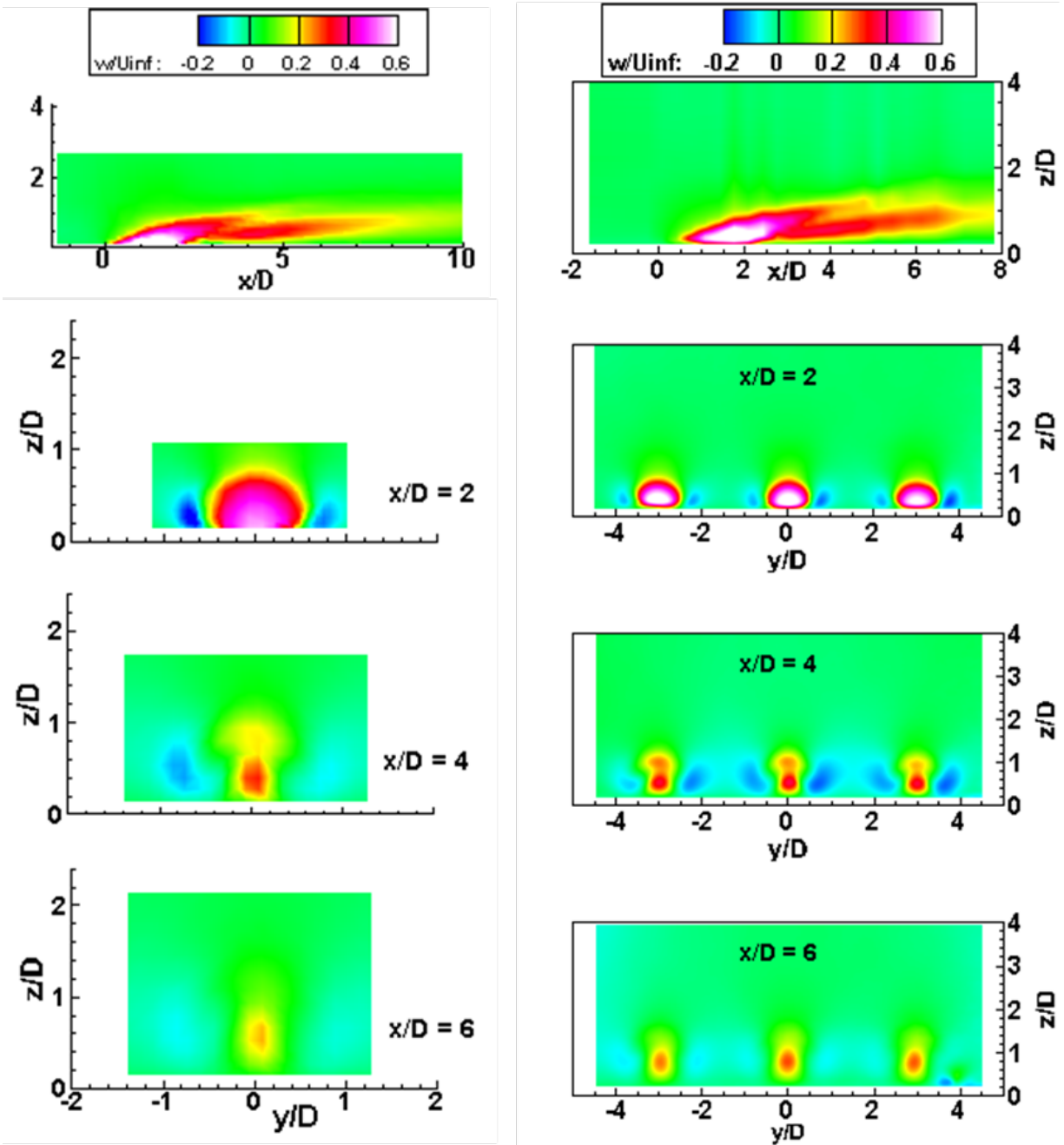


Figure E.1.—(c) w -component velocity, $BR = 1.2$, HW Probes 1 and 2 and PIV.

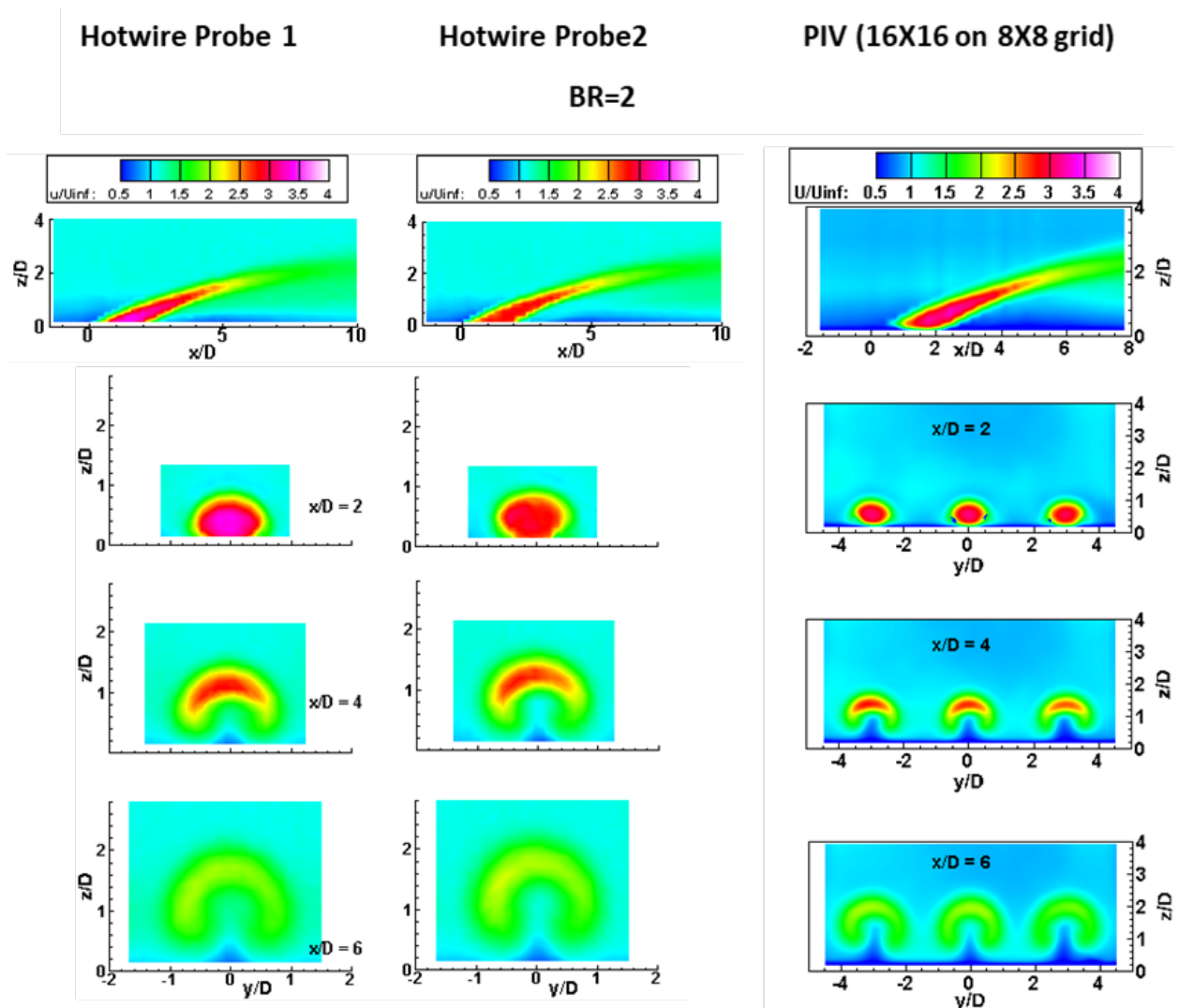


Figure E.2.—(a) u -component velocity, $BR = 2.4$, HW Probes 1 and 2 and PIV.

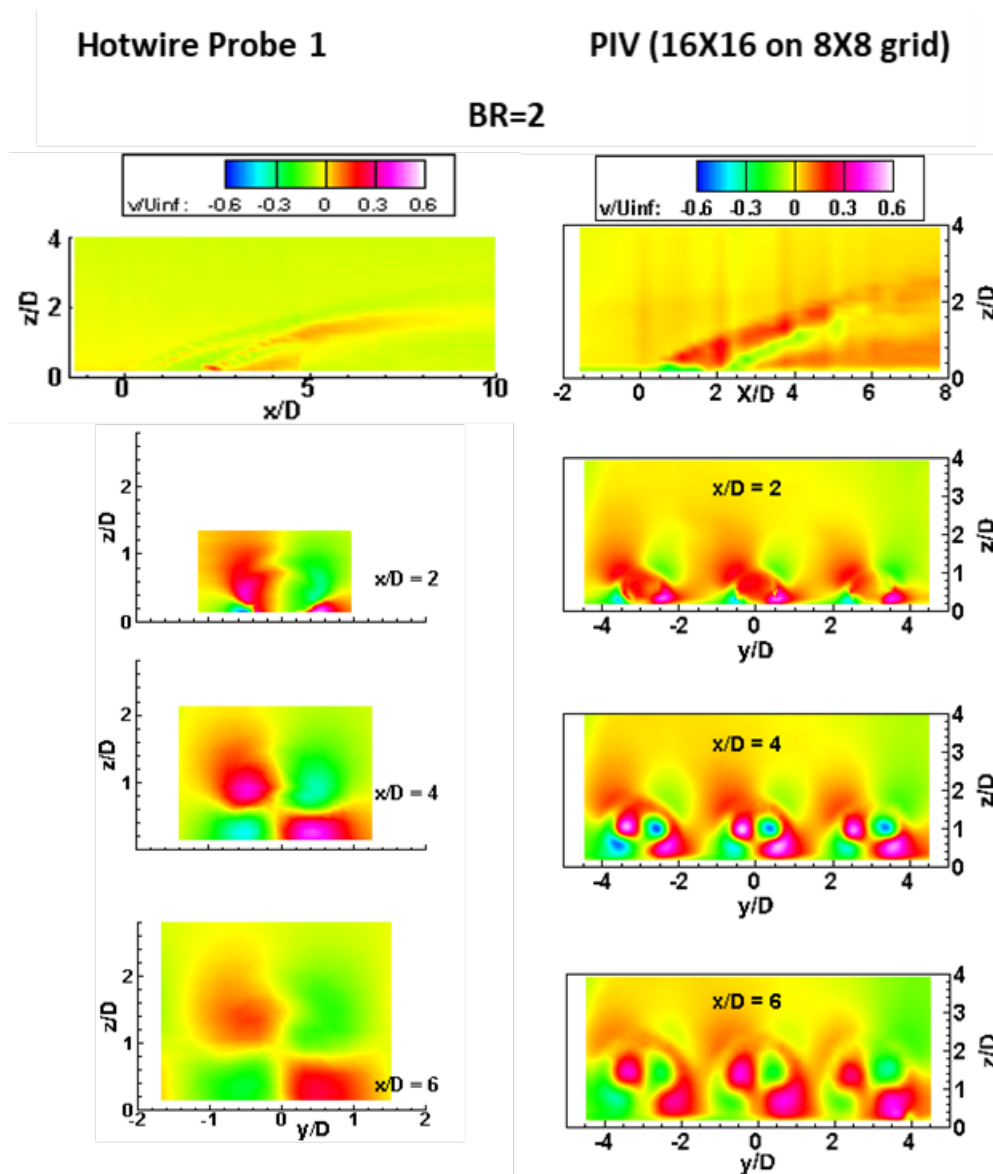


Figure E.2.—(b) v -component velocity, $BR = 2.4$, HW Probes 1 and 2 and PIV.

Hotwire Probe 2

PIV (16X16 on 8X8 grid)

BR=2

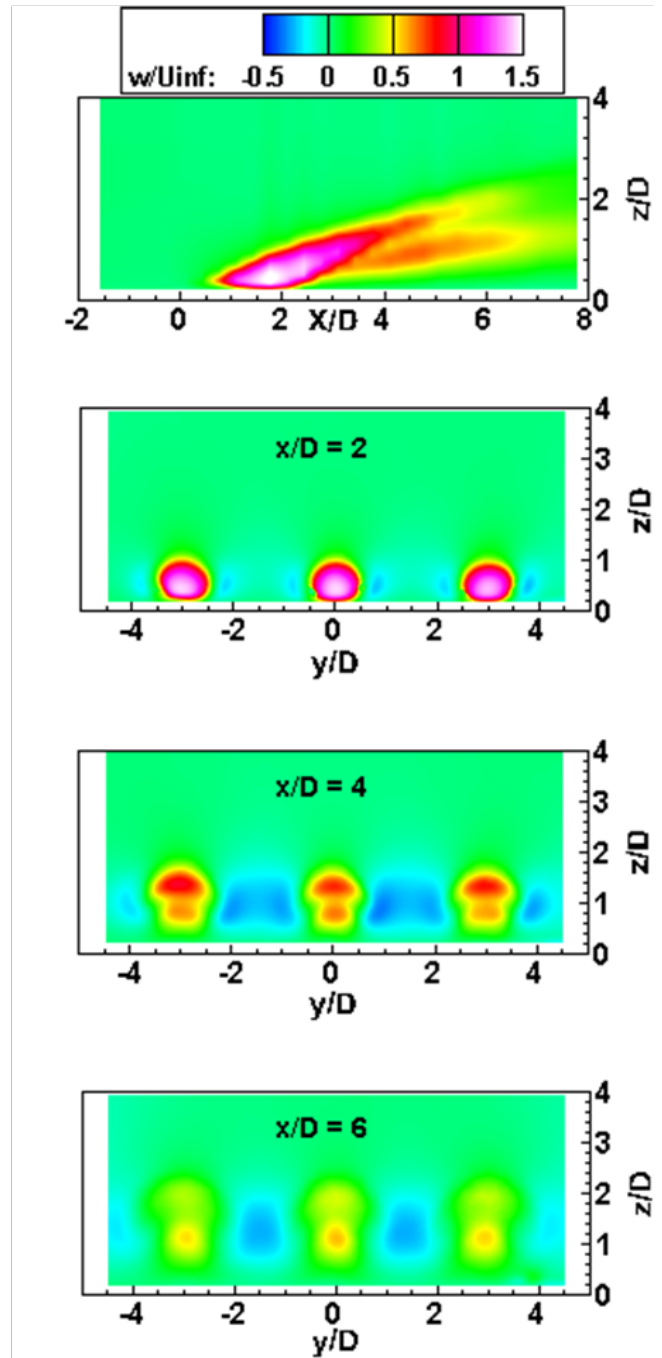
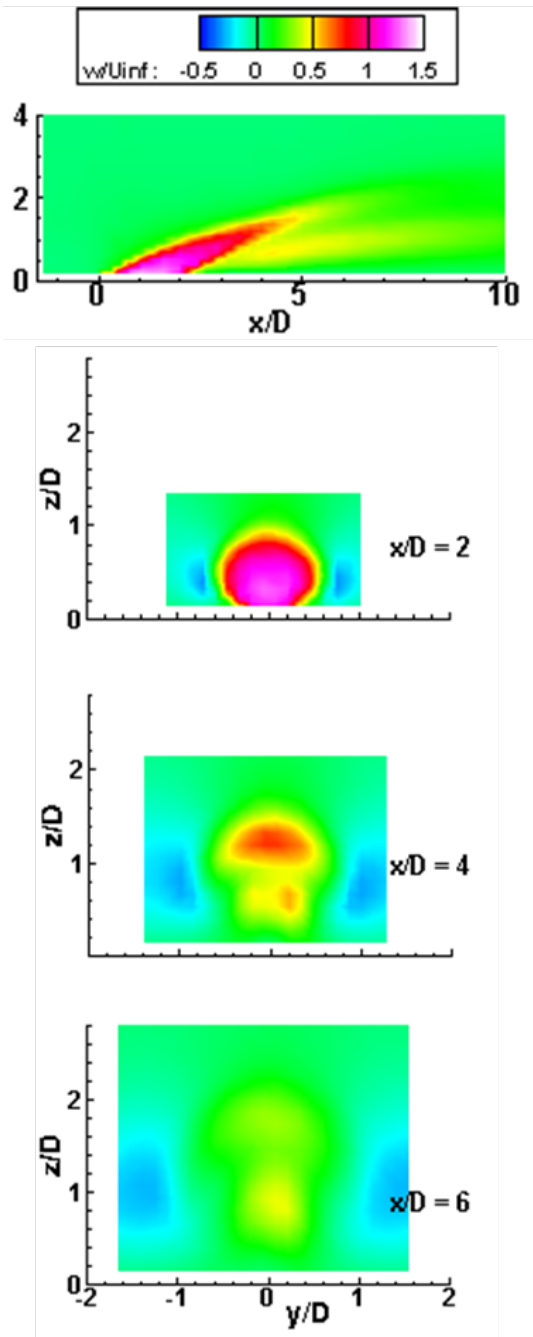


Figure E.2.—(c) w-component velocity, $BR = 2.4$, HW Probes 1 and 2 and PIV.

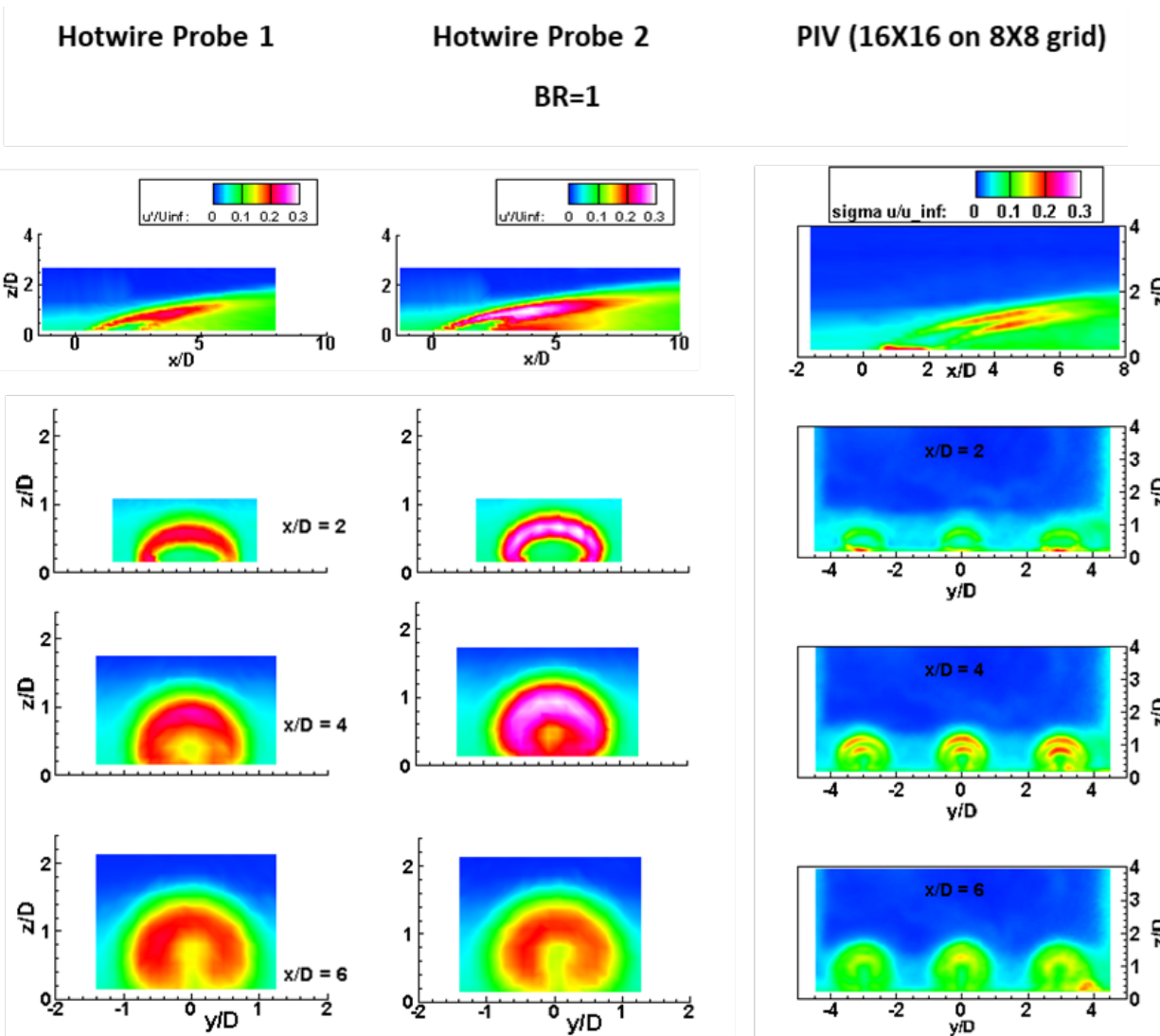


Figure E.3.—(a) Velocity component fluctuation u' , $BR = 1.2$, HW Probes 1 and 2 and PIV.

Hotwire Probe 1

PIV (16X16 on 8X8 grid)

BR=1

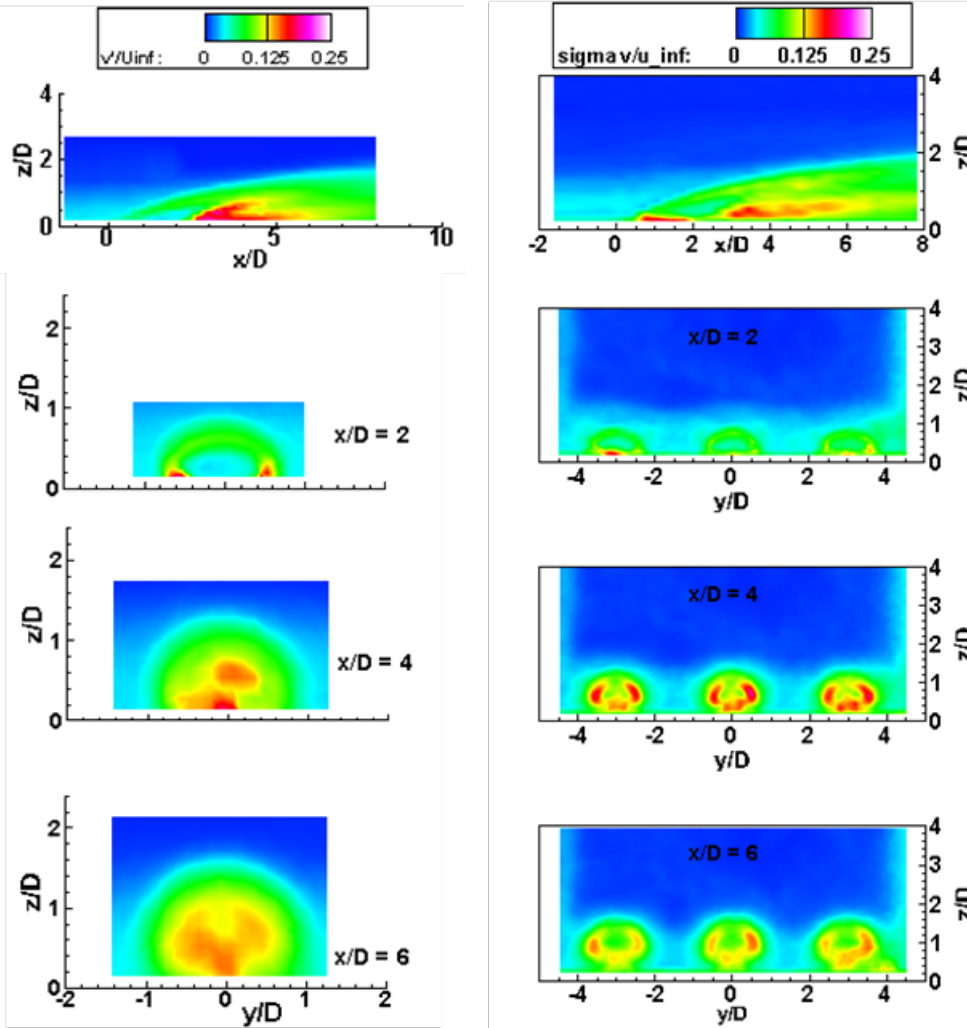


Figure E.3.—(b) Velocity component fluctuation v' , $BR = 1.2$, HW Probes 1 and 2 and PIV.

Hotwire Probe 2

PIV (16X16 on 8X8 grid)

BR=1

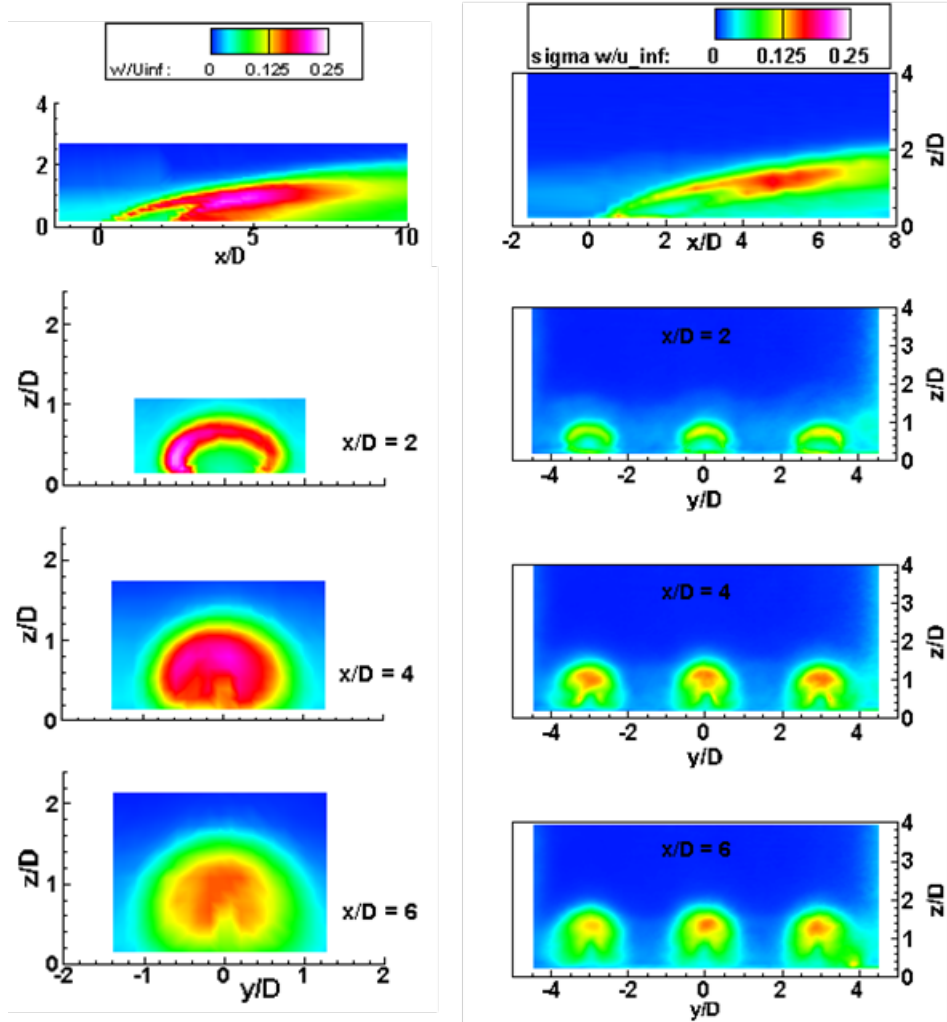


Figure E.1.—(c) Velocity component fluctuation w' , $BR = 1.2$, HW Probes 1 and 2 and PIV.

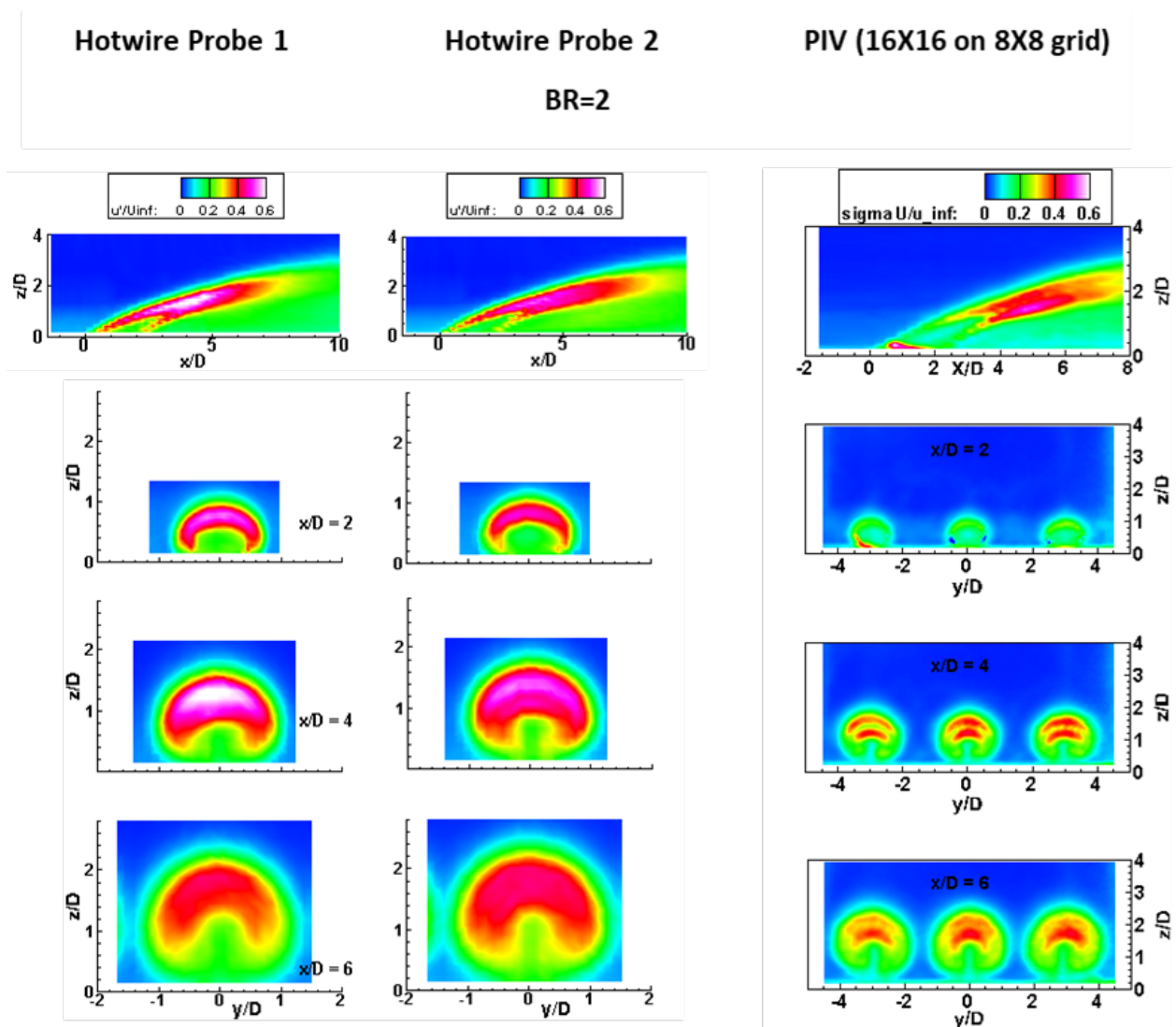


Figure E.4.—(a) Velocity component fluctuation u' , $BR = 2.4$, HW Probes 1 and 2 and PIV.

Hotwire Probe 1

PIV (16X16 on 8X8 grid)

BR=2

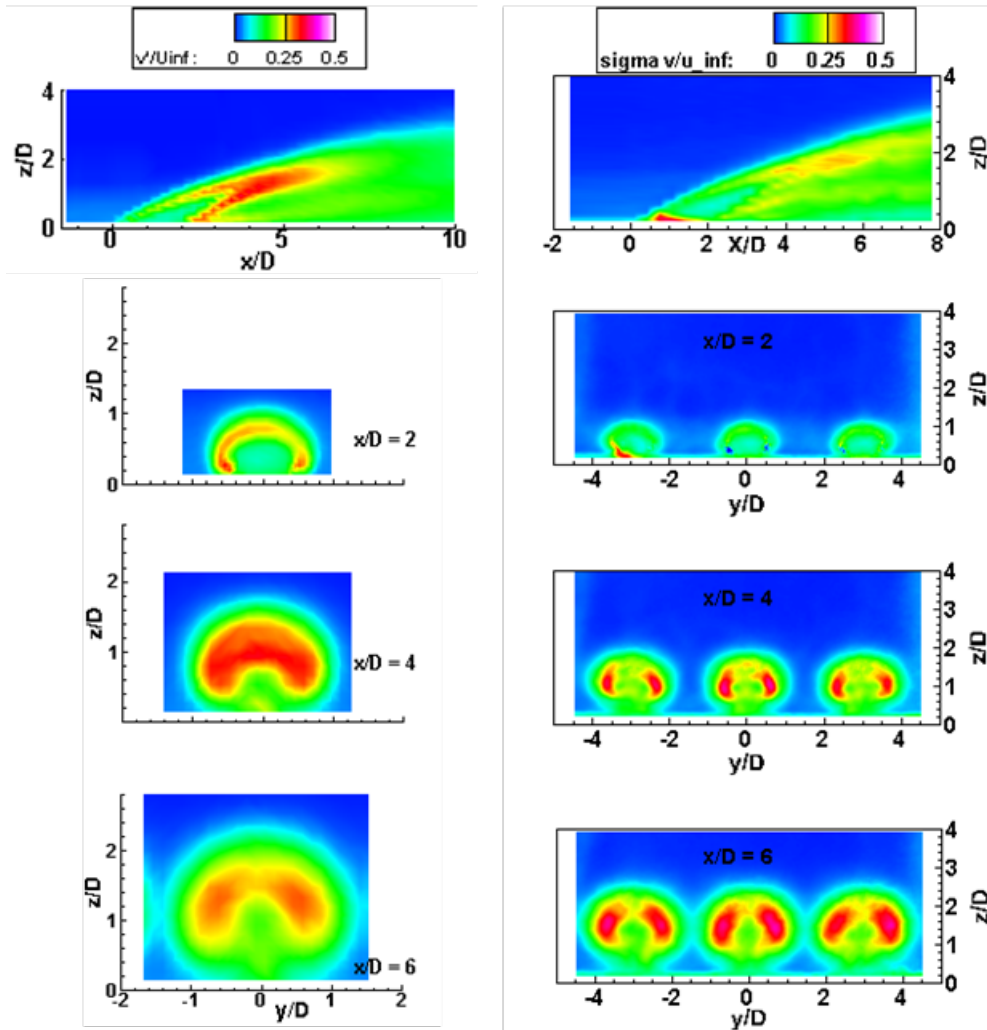
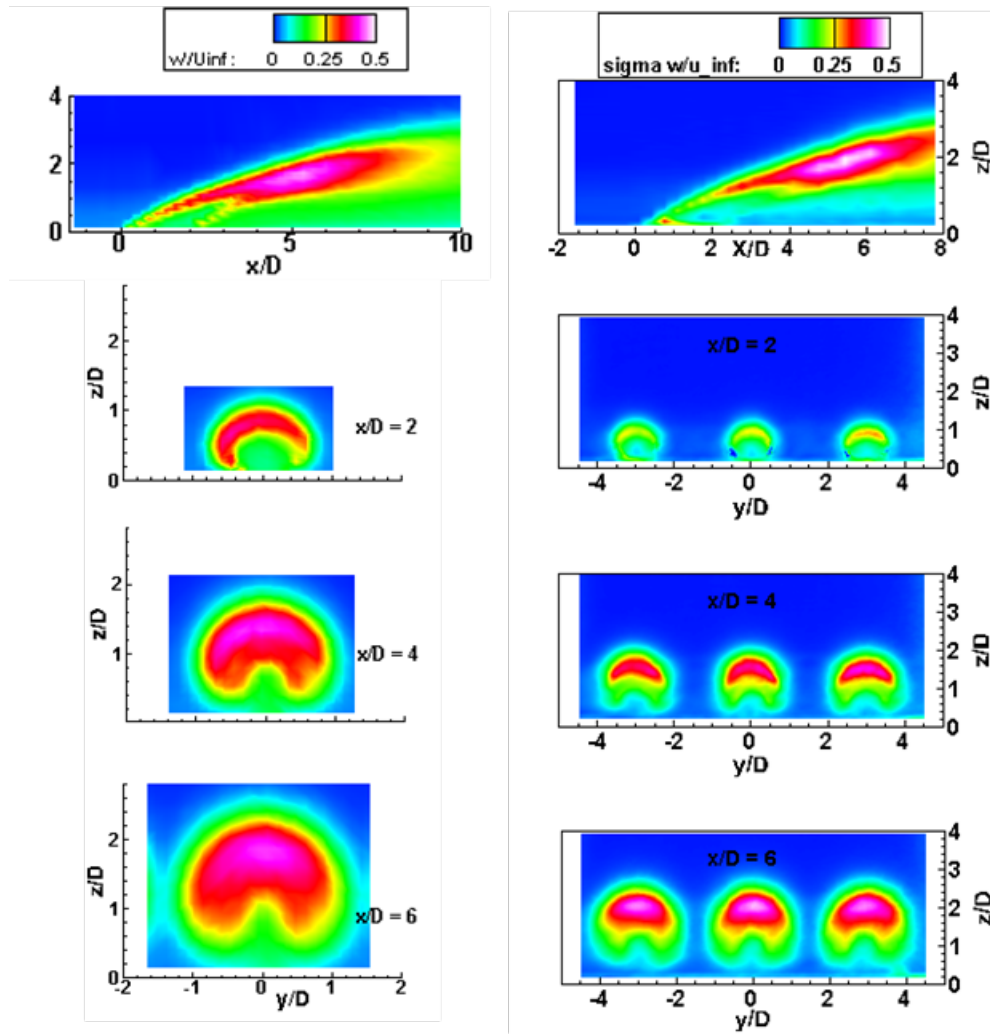


Figure E.4.—(b) Velocity component fluctuation v' , $BR = 2.4$, HW Probes 1 and 2 and PIV.

Hotwire Probe 2

PIV (16X16 on 8X8 grid)

BR=2



Hotwire Probe 1

PIV (16X16 on 8X8 grid)

BR=1

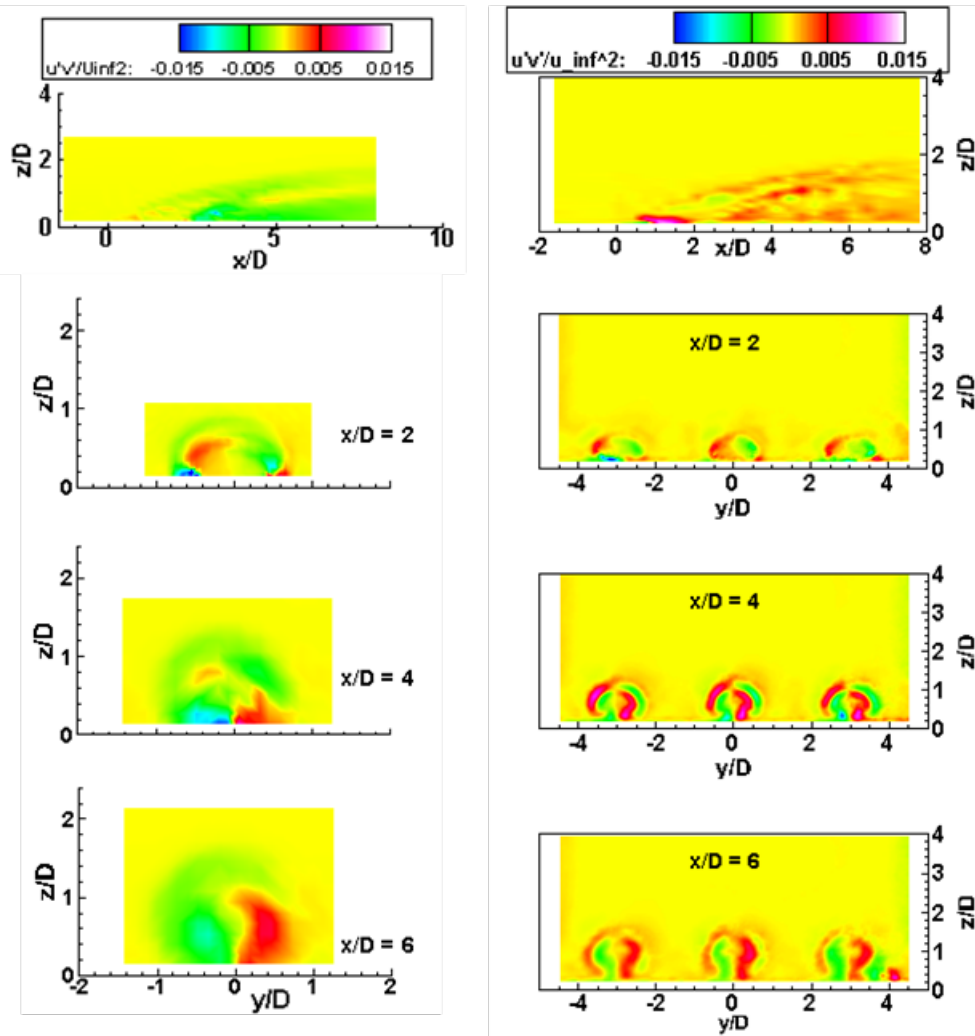


Figure E.5.—(a) $u'v'$, $BR = 1.2$, HW Probes 1 and 2 and PIV.

Hotwire Probe 2

PIV (16X16 on 8X8 grid)

BR=1

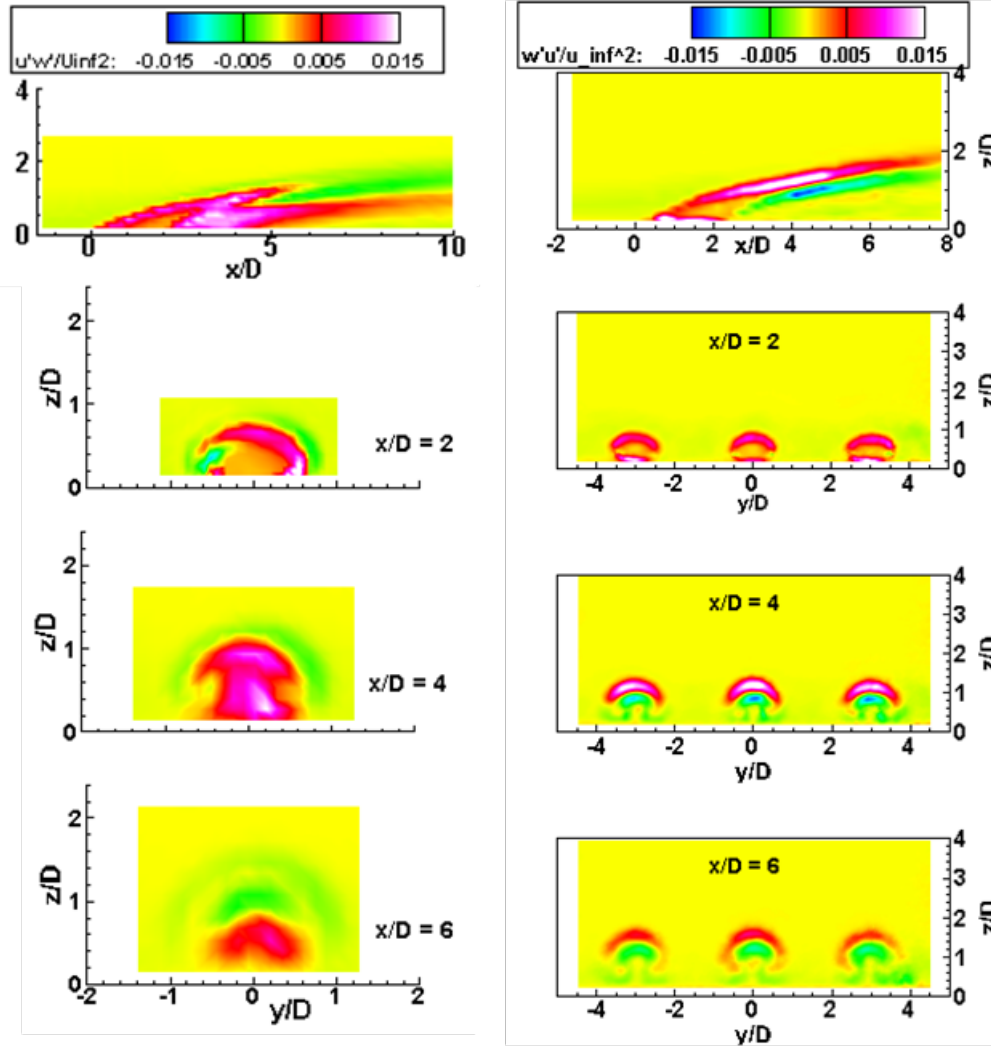


Figure E.5.—(b) $u'w'$, $BR = 1.2$, HW Probes 1 and 2 and PIV.

Hotwire Probe 1

PIV (16X16 on 8X8 grid)

BR=2

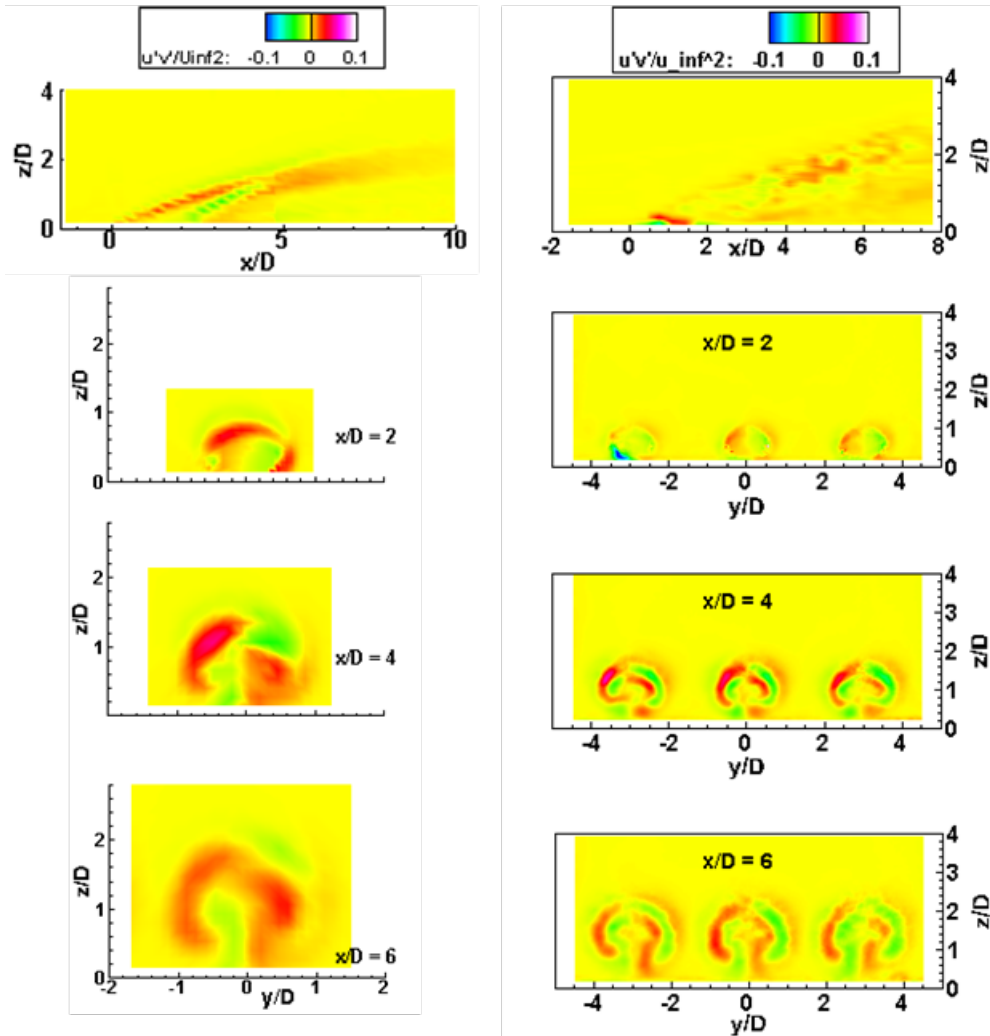


Figure E.6.—(a) $u'v'$, BR = 2.4, HW Probes 1 and 2 and PIV.

Hotwire Probe 2

PIV (16X16 on 8X8 grid)

BR=2

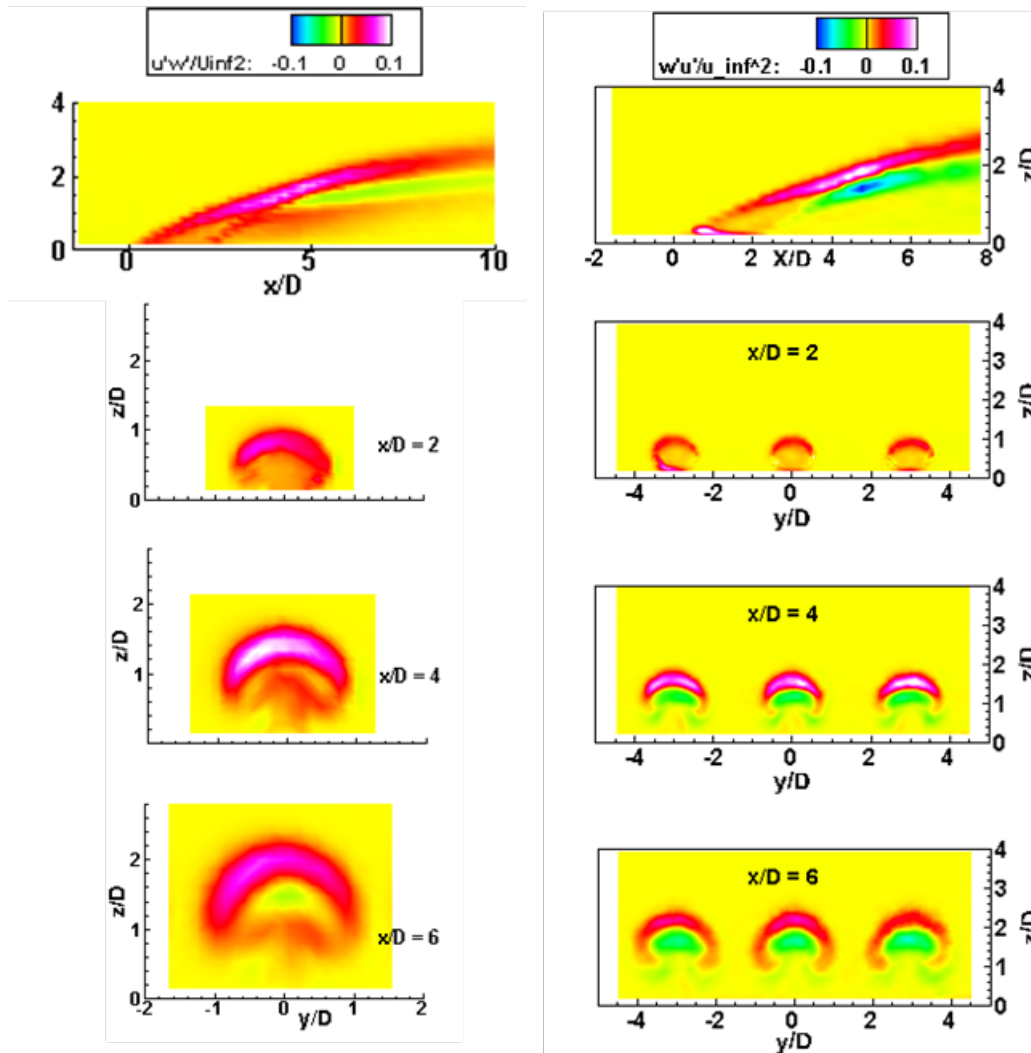


Figure E.6.—(b) $u'w'$, $BR = 2.4$, HW Probes 1 and 2 and PIV.

Appendix F.—Comparison of 1-Hole and 3-Hole Data

The data presented in this paper shows only the center hole of a flat plate with 3 holes. The purpose was to provide symmetrical periodic flows with no side wall effects. As expected, the 3-hole data showed appropriate symmetry among the holes. Some preliminary hot wire and PIV data was acquired on a 1-hole plate and compared to the 3-hole plate (Figure F.1). In general, little differences were noted for the flow conditions that were tested. Only far downstream would the results be different, with multiple jets interacting with each other.

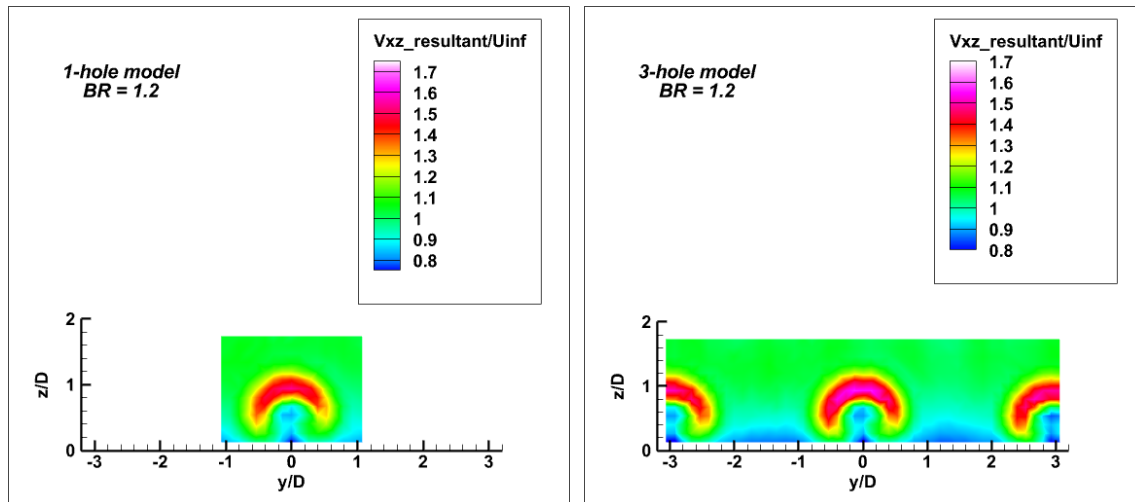


Figure F.1.—Comparison of 1-hole and 3-hole velocity data, $x/D = 4$, $BR = 1.2$.

Appendix G.—3D Data Representation

Another way of displaying the data is a three-dimensional view, showing the centerline and spanwise planes together in an isometric view. Figure G.1 and Figure G.2 show dimensionless velocity and temperature data taken behind the jet emanating from the 30° angled round hole into the free stream flow for $BR = 1.2$ and $BR = 2.4$. The jet for the $BR = 2.4$ case can easily be seen in this view to lift off the test section floor, with the jet spreading out laterally moving downstream and the typical “kidney shaped” vortex pattern.

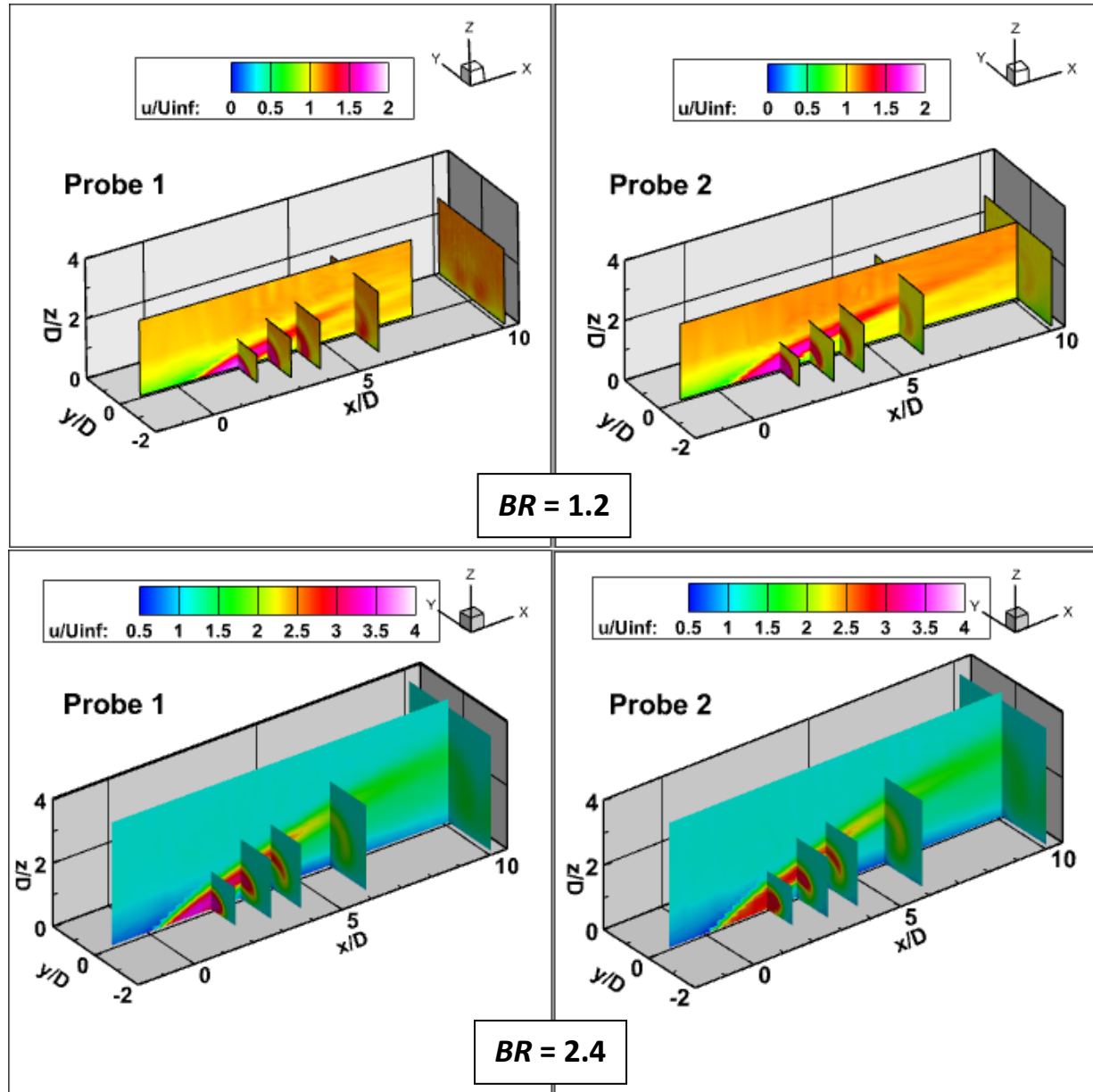


Figure G.1.— u velocity component, $BR = 1.2$ and $BR = 2.4$, xT Probes 1 and 2.

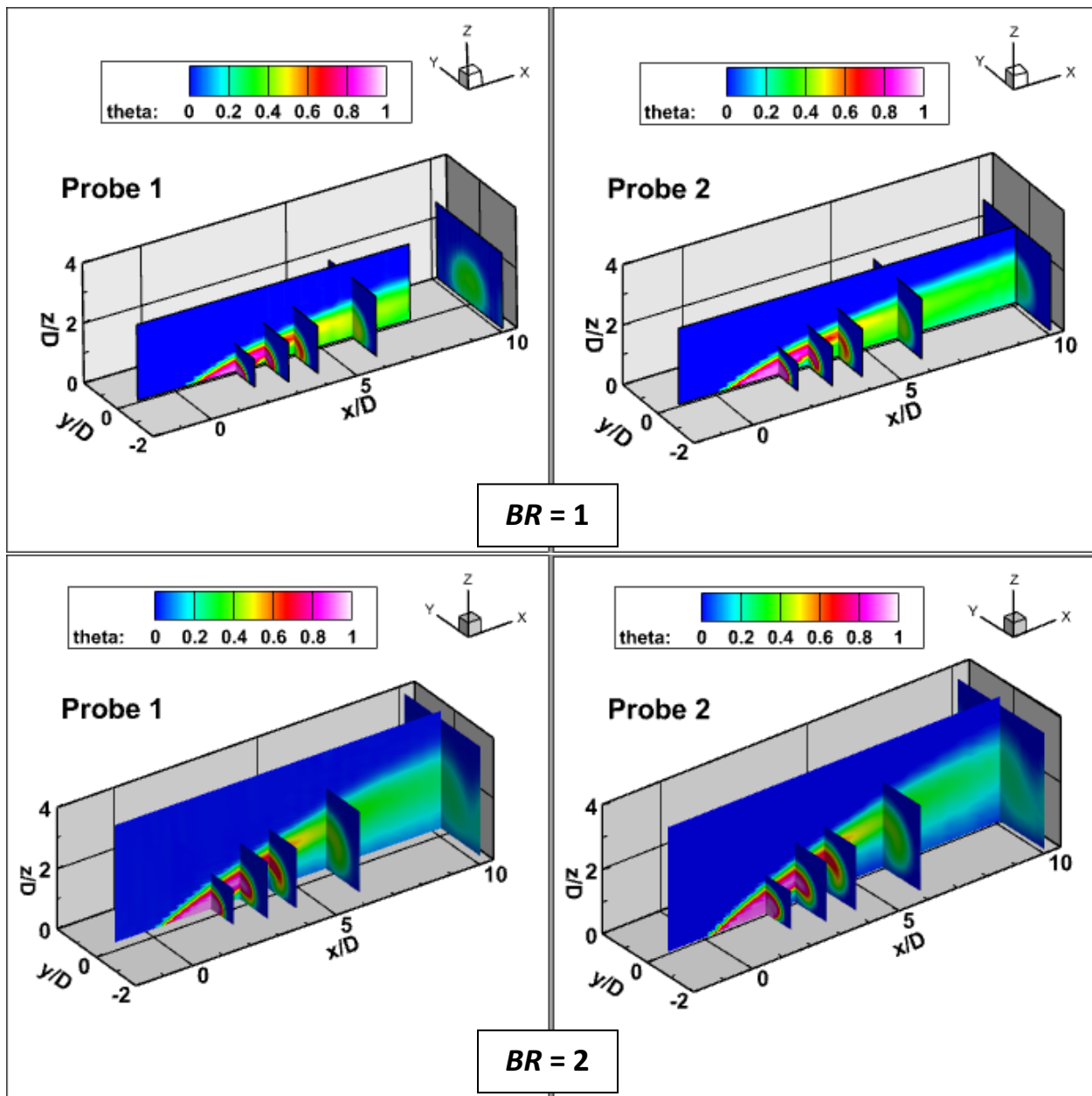


Figure G.2.—Nondimensional temperature, $BR = 1.2$ and $BR = 2.4$, xT Probes 1 and 2.

Appendix H.—Temperature Compensation Technique

It is possible for the low-pass frequency filtering inherent to constant current anemometry measurements to limit the temperature fluctuation signal. To account for this, a compensation technique based on Reference 14 and also employed in Reference 11 can be used to adjust the signal to noise ratio of the temperature measurements acquired. This method provides an estimated reconstruction of low-pass filtered temperature signals from a fine-wire thermometer. Figure H.1 shows the nondimensional uncompensated temperature fluctuation that is presented in this report and the temperature fluctuation calculated using the compensation technique at $BR = 2.4$. Figure H.2 shows the percent difference between the two calculations. The trends between the two are the same. The difference in the freestream is quite small, but the percent difference shows high values due to the small dT value used to normalize the data, so the freestream percent difference is not displayed in order to focus on the region of interest of the coolant jet. The compensation technique increases temperature fluctuation values 8 to 16 percent in the core and about 20 percent in the shear layer edges and beneath the jet. While the compensation technique provides higher estimates of the fluctuating values, given the limited spatial resolution of the experimental data, it was decided that the uncompensated data should be presented for this report. Data trends are not different and flow analysis is similar.

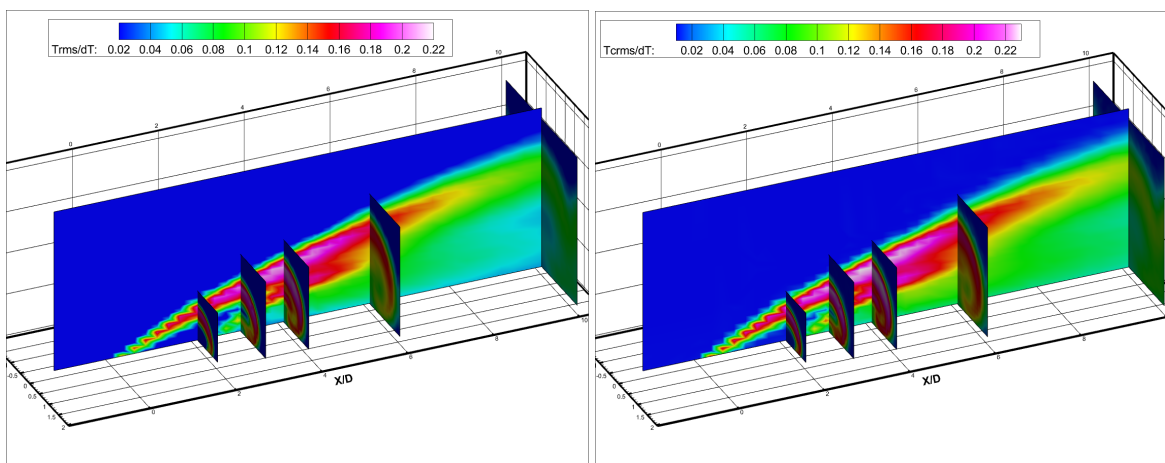


Figure H.1.—Nondimensional temperature fluctuation, uncompensated (left) and compensated (right), $BR = 2.4$.

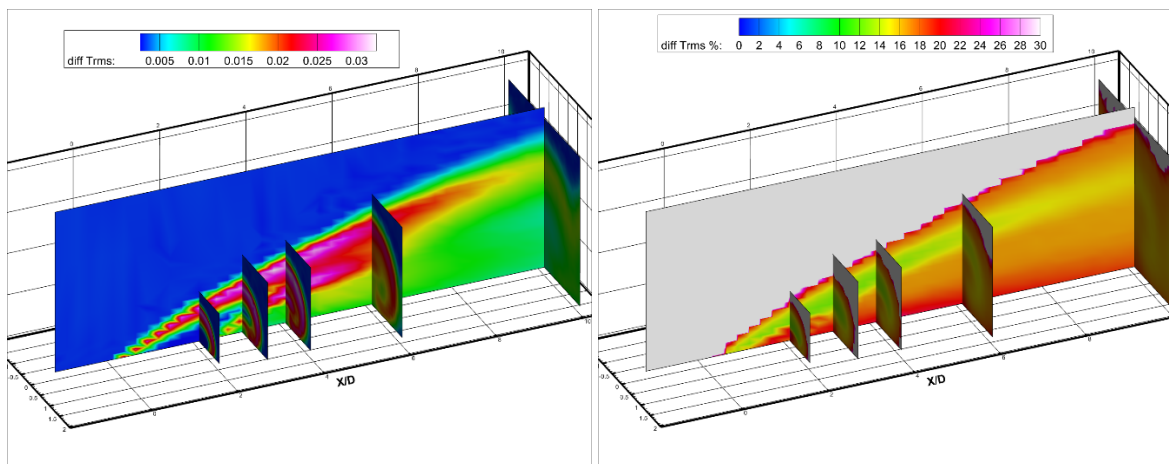


Figure H.2.—Nondimensional temperature fluctuation difference (left) and percent difference (right), $BR = 2.4$.

References

1. Wernet, M., Wroblewski, A., Locke, R., “A Dual-Plane PIV Study of Turbulent Heat Transfer Flows,” NASA/TM—2016-219074.
2. Wernet, M., “PIV and Rotational Raman-Based Temperature Measurements for CFD Validation of a Perforated Plate Cooling Flow, Part 1,” NASA/TM—2019-220227/PART1.
3. El-Gabry, L., Thurman, D., Poinatte, P., Heidmann, J., “Detailed Velocity And Turbulence Measurements In An Inclined Large Scale Film Cooling Array,” *Journal of Turbomachinery*, Nov 2013, 135(6): 061013, <https://doi.org/10.1115/1.4023347>, 2013.
4. Thole, K. A., Sinha, A. K., Bogard, D. G., and Crawford, M. E., “Mean Temperature Measurements of Jets with a Crossflow for Gas Turbine Film Cooling Applications,” *Rotating Machinery: Transport Phenomena, Proceedings of the 3rd International Symposium on Transport Phenomena and Dynamics of Rotating Machinery*, Taylor and Francis, Washington, D.C., 1990, pp. 69–85.
5. Womack, K., Volino, R., Schultz, M., “Measurements in Film Cooling Flows With Periodic Wakes,” *Journal of Turbomachinery*, Vol. 130, DOI: 10.1115/1.2812334, 2008.
6. Schreivogel, P., Abram, C., Fond, B., Straußwald, M., Beyrau, F., Pfitzner, M., “Simultaneous kHz-rate temperature and velocity field measurements in the flow emanating from angled and trenched film cooling holes,” *International Journal of Heat and Mass Transfer*, 103 (2016) 390–400.
7. Kohli, A., Bogard, D., “Turbulent Transport in Film Cooling Flows,” *Journal of Heat Transfer*, Vol. 127, pp. 513-520, 2005.
8. Lau, S., Meiritz, K., Ram, V., “Measurement of momentum and heat transport in the turbulent channel flow with embedded longitudinal vortices,” *International Journal of Heat and Fluid Flow*, Vol. 20, pp. 128-141, 1999.
9. Smits, A., Perry, A., “A Note on Hot-wire Anemometer Measurements of Turbulence in the Presence of Temperature Fluctuations,” *Journal of Physics E: Scientific Instruments*, Vol. 14, Number 3, pp. 311-312, 1981.
10. Smits, A., Perry, A., Hoffman, P., “The response to temperature fluctuations of a constant-current hot-wire anemometer,” *Journal of Physics E: Scientific Instruments*, Vol. 11, Number 9, pp. 909-914, 1978.
11. Borghi, M., Thurman, D., Poinatte, P., Engblom, W., “Numerical and Experimental Examination of Turbulent Mixing of a Heated Jet in Crossflow,” *Journal of Thermophysics and Heat Transfer*, Vol. 34, Number 2, <https://doi.org/10.2514/1.T5608>, 2020.
12. Thurman, D., Poinatte, P., Ameri, A., Culley, D., Raghu, S., Shyam, V., “Investigation of Spiral and Sweeping Holes,” *Journal of Turbomachinery*, Vol. 138, Issue 9, DOI: 10.1115/1.4032839, TURBO-15-1305, 2016.
13. El-Gabry, L., Thurman, D., Poinatte, P., “Procedure for Determining Turbulence Length Scales Using Hotwire Anemometry,” NASA/TM—2014-218403.
14. Tagawa, M., Kato, K., and Ohta, Y., “Response compensation of fine-wire temperature sensors,” *Review of Scientific Instruments*, Vol. 76, No. 9, 2005, p. 094904.

